HAL
open science

Exploration of Compressive Sampling for Wire Diagnosis Systems Based on Reflectometry

Tzila Ajamian

▶ **To cite this version:**

Tzila Ajamian. Exploration of Compressive Sampling for Wire Diagnosis Systems Based on Reflectometry. Signal and Image processing. École centrale de Nantes, 2019. English. NNT : 2019ECDN0040 . tel-02475792

HAL Id: tel-02475792

https://theses.hal.science/tel-02475792v1

Submitted on 12 Feb 2020

HAL is a multi-disciplinary open access archive for the deposit and dissemination of scientific research documents, whether they are published or not. The documents may come from teaching and research institutions in France or abroad, or from public or private research centers.

L'archive ouverte pluridisciplinaire **HAL**, est destinée au dépôt et à la diffusion de documents scientifiques de niveau recherche, publiés ou non, émanant des établissements d'enseignement et de recherche français ou étrangers, des laboratoires publics ou privés.

THÈSE DE DOCTORAT DE

L'ÉCOLE CENTRALE DE NANTES
COMUE **U**NIVERSITE **B**RETAGNE **L**OIRE

Ecole Doctorale N°601
Mathèmatique et Sciences et Technologies
de l'Information et de la Communication
Spécialité : Signal, Image, Vision

Par

« Tzila AJAMIAN »

« Exploration de l'Acquisition Comprimée appliquée à la Réflectométrie »

Thèse présentée et soutenue à NANTES, le 24 Octobre 2019
Unité de recherche : Laboratoire des Sciences du Numérique de Nantes (LS2N), UMR 6004

Rapporteuses avant soutenance :

Marie CHABERT, Professeur des universités, Université de Toulouse

Virginie DEGARDIN, Professeur des universités, Université de Lille

Composition du jury :

Président :	Qinghua ZHANG, Directeur de recherche à l'Institut National de Recherche en Informatique et en Automatique, Rennes
Examinatrice :	Caroline CHAUX, Chargée de recherche au Centre National de la Recherche Scientifique, Aix-Marseille Université
Dir. de thèse :	Saïd MOUSSAOUI, Professeur des universités, École Centrale de Nantes
Co-dir. de thèse :	Antoine DUPRET, Ingénieur chercheur, Commissariat à l'Énergie Atomique et aux Énergies Alternatives, Saclay

Invité
Olivier-Henri ROUX, Professeur des universités, École Centrale de Nantes

ACKNOWLEDGEMENT

This thesis work has been conducted in the Laboratory of Reliability and Sensors Integration (LFIC), part of the CEA Laboratory of Systems and Technologies Integration (CEA-LIST).

Firstly, I would like to thank Marie CHABERT and Virginie DEGARDIN, the reviewers of my Ph.D. thesis by whom I was honored. I would also thank Caroline CHAUX, Qinghua ZHANG, and Olivier-Henri ROUX, who agreed with all humbleness to be members of my jury.

I would love to express my gratitude to Thierry COLETTE and Jean-René LEQUEPEYS, heads to the Department of Architecture, Design, and Embedded Software (DACLE) for offering me the opportunity to manipulate my thesis in good conditions in their unit.

My sincere thanks also go to Antoine DUPRET and Tanguy SASSOLAS, heads of the LFIC, who provided me the opportunity to join their team as a Ph.D. student, and who gave me access to the laboratory and research facilities.

I would love to express my sincere gratitude to my thesis director Saïd MOUSSAOUI for his crucial support and trust, his insightful knowledge, and without whom I would not have been able to achieve this work. I owe him not just for his scientific ideas, but for guiding me in the wide world of academics. I am also grateful for his warm welcome each time he welcomed me in the Laboratory of Digital Sciences of Nantes (LS2N).

Besides my director, I would like to thank my adviser Antoine DUPRET for his great help, his availability, and his guidance. Without forgetting to thank him for all the scientific discussions we had, which made me overcome all the difficulties, especially during the writing of this thesis.

I would also like to thank my fellow LFIC lab-mates, for their support and help and for all the stimulating discussions we had. In particular, I am very grateful to Esteban, Jaume, Cyril, Mariem, Moussa, and Wafa for the valuable pieces of advice they gave, especially during this last year.

I would also like to thank former lab-mates, who left LFIC for other adventures and who were crucial to my work experience in the laboratory. I am grateful to Daniel and Christophe for all the joyful moments we shared and the pleasant atmosphere they

managed to bring in to LFIC.

My heartfelt appreciation, with a special thank you, goes to Caaliph from LCE for his cheerfulness, his positive attitude, and helps.

A special thank you to my friends, Thibault, Emmanuel, and Alejandro. The radiant, the sprightly, and the breezy.

In this period of my life, I consider myself lucky enough to meet someone as kind and generous as Emna. My office mate, my partner in crime, who was always present to take away all the negative vibes. Who turned every black day of mine into a white one and whose presence in the LFIC enlightened my mind.

I mainly owe this achievement to my parents Taline and Minas, to my sister Hranig and her husband Vako, who never doubted in my abilities or stopped encouraging me and who always supported in every possible way in all the crucial times of my life. Here I would like to remember my late grandmother Sossi and my late grandfather Mesrob, whom I consider now my guardian angel, who follows me with every step I take, whose prayers have been heard and to whom I dedicate all my hard work.

Last but not least, I would like to mention Khatchig, my best friend, for believing in me even when I did not. The one who often accompanied my overnight stays. With whom I fought against my fears and insecurities. I thank him for his daily support, his exceptional patience, and amazing entertainment. He always knew how to cheer me up and I learned to rediscover life through his innocent gaze.

It's always sunny somewhere...

TABLE OF CONTENTS

Glossary **7**

Nomenclature **11**

List of Figures **11**

List of Tables **16**

General Introduction **18**

1 Principals of Wire Diagnosis by Reflectometry **25**

1.1 Introduction 25

1.2 Wiring faults: hard faults vs. soft faults 26

1.2.1 Hard faults 27

1.2.2 Soft faults 27

1.3 Fault location technique by reflectometry 30

1.3.1 Reflectometry's concept 31

1.3.2 Reflectometry based methods 34

1.3.2.1 Reflectometry techniques based on the frequency domain analysis 35

1.3.2.2 Reflectometry techniques based on the time domain analysis 37

1.4 Embedded diagnosis and hardware requirements 42

1.4.1 Hardware limitation 45

1.5 Conclusion 46

2 Compressive Sampling **49**

2.1 Introduction 49

2.2 Methodology of CS 50

2.2.1 Sparsity 51

2.2.2 Acquisition phase 52
2.2.2.1 Properties 53
2.2.3 Recovery phase 54
2.2.4 Performance metrics 56
2.3 Analog measurement matrix 57
2.3.1 Non-Uniform Sampling (NUS) 58
2.3.2 Random Demodulator (RD) 59
2.3.3 Modulated Wideband Converter (MWC) 61
2.3.4 Summary on analog encoder AIC 62
2.4 Conclusion 64

3 Sparse Dictionary for Reflectometry Signals 67
3.1 Introduction 67
3.2 Complex chirp signal 68
3.2.1 Principles of Fractional Fourier Transform (FrFT) 70
3.2.1.1 The optimal fractional angle of FrFT for complex linear chirp signal 71
3.2.2 Application of α_{opt} to injected signal 73
3.2.3 Application of α_{opt} to reflected signal 75
3.3 Real Multi-Carrier (MC) signal 80
3.3.1 Principles of Discrete Cosine Chirp Transform (DCCT) 81
3.3.1.1 Theory 81
3.3.1.2 Implementation 82
3.3.2 DCCT with CS 83
3.3.3 Simulation results and figure of merit 87
3.4 Conclusion 91

4 Compressive Sampling for Reflectometry 93
4.1 Introduction 93
4.2 Proposed system 94
4.3 Standard reflectometry-based system for wire diagnosis 98
4.3.1 Point-to-point wire diagnosis 98
4.3.2 Diagnosis of the state of a Y complex network 100
4.4 Implementation of CS methods for reflectometry-based system for wire diagnosis 102

4.4.1 Impact of detection and localization for point-to-point wire 103
4.4.2 Impact of detection and localization for complex wire 107
4.5 Experimental results 114
4.5.1 Impact of the filter 118
4.6 Conclusion 119

General Conclusion and Perspectives **121**

Bibliography **125**

GLOSSARY

ADC	Analog-to-Digital Converter.
AIC	Analog-to-Information Converter.
ASIC	Application Specific Integrated Circuit.
CF	Compression Factor.
CR	Compression Ratio.
CS	Compressed Sampling.
DAC	Digital-to-analog Converter.
DC	Direct Current.
DCCT	Discrete Cosine Chirp Transform .
DCT	Discrete Cosine Transform.
FDR	Frequency Domain Reflectometry.
FMCW	Frequency-Modulated Continuous-Wave.
FPGA	Field-Programmable Gate Array.
FrFT	Fractional Fourier Transform.
FT	Fourier Transform.
IDCCT	Inverse DCCT.
IF	Instantaneous Frequency.
IFFT	Inverse Fast Fourier Transform.
MC	Multi-Carrier.
MCR	Multi-Carrier Reflectometry.
MCTDR	Multi-Carrier TDR.

MSR	Mixed-Signal Reflectometry.
MWC	Modulated-Wideband Converter.
NDR	Noise Domain Reflectometry.
NUS	Non-Uniform Sampling.
NUT	Network Under Test.
OFDM	Orthogonal Frequency Division Multiplexing.
OMP	Orthogonal Matching Pursuit.
OMTDR	Orthogonal Multi-tone TDR.
PDFDR	Phase Detection FDR.
PN	Pseudo Noise.
PRBS	Pseudo-Random Binary Sequence.
PRD	Percentage Root-mean-Square difference.
PSK	Phase-Shift Keying.
RD	Random Demodulator.
RIP	Restricted Isometry Property.
RMSE	Root Mean Squared Error between.
SINAD	Signal to Noise and Distortion.
SNR	Signal to Noise Ratio.
SSTDR	Spread Spectrum TDR.
STDR	Sequence TDR.
SWR	Standing-Wave Reflectometry.
TDR	Time Domain Reflectometry.
VCO	Voltage-Controlled Oscillator.

WD Wigner-Ville Distribution.

NOMENCLATURE

Reflectometry

$\mathbf{a_i[n]}$ Real or complex discrete-time domain injected signal

$\mathbf{a_r[n]}$ Real or complex discrete-time domain reflected signal

$a_i(t)$ Real or complex continuous injected signal

$a_r(t)$ Real or complex continuous reflected signal

c Speed of light in a vacuum inertial system

Compressive Sampling

$\mathbf{\Phi}$ Sensing or measurement matrix of length $\mathrm{M} \times \mathrm{N}$

$\mathbf{\Psi}$ Sparse dictionary matrix of length $\mathrm{N} \times \mathrm{N}$

$\mathbf{\Theta}$ Reconstruction matrix of length $\mathrm{M} \times \mathrm{N}$

$||\cdot||_0$ Pseudo norm l_0 calculated as : $||\cdot||_0 = \#\{\mathrm{i} : \cdot_\mathrm{i} \neq 0\}$

$||\cdot||_p$ Norm l_p calculated as : $\left(\sum_{i=1}^{n} |\cdot_i|^p\right)^{(1/p)}$ with $0 < p < \infty$

f_s Sampling frequency with respect to Shannon-Nyquist theory

f_{max} Maximum frequency of the testing signal

$f_{s\text{-}s}$ Sub-sampling frequency without respecting Shannon-Nyquist theory

General

$\cdot * \cdot$ Convolution product of two signals

$\cdot \star \cdot$ Cross-correlation between two signal (discrete or continuous domain)

$\langle \cdot, \cdot \rangle$ Inner product

$\mathbf{a}^*$	Complex conjugate of a vector
$\mathbf{A}^\dagger$	Moore-Penrose pseudo inverse of $\mathbf{A}$
$\mathbf{a}^\mathrm{T}$	Transpose of a vector
$\mathcal{F}$	Fourier Transformation
$\mathcal{F}^a$	Fractional Fourier Transformation of order a

LIST OF FIGURES

1.1 Hard faults in aeronautical cables [14]. 27
1.2 A progressive chafing example of an aircraft cable during a flight cycle [16]. 28
1.3 Instantaneous damage versus the time phases (mortality phase, useful lifetime and worn-out phase) of different type of defects. 29
1.4 A scheme showing the principal of reflectometry. 31
1.5 A reflectogram showing the responses of reflected signal for different impedances at $50\ \mathrm{m}$ where $Z_c = 50\ \Omega$. 32
1.6 Equivalent circuit of a small part of a transmission line, showing the per-unit-length parameters R, L, C, and G. 33
1.7 An example of a linear chirp signal occupying a bandwidth of 50MHz for FDR implementation. 36
1.8 An example of MCTDR signal. On the left, the spectrum of multi-carrier signal and on the right, the time domain representation of the signal [44]. 40
1.9 Typical embedded wire diagnosis setup. Using a FPGA to generate the injected signal $\mathbf{x_i[n]}$, to save the reflected signal $\mathbf{x_r[n]}$ and finally to apply a cross-correlation. The conversion from digital to analog and vice-versa is applied by DAC and ADC respectively. The sampling frequency, f_s, is defined by Shannon-Nyquist theory. 42
1.10 A conceptual approach between the conversion rate (speed) and the resolution for Nyquist ADCs architectures. 46

2.1 Conceptual illustration of the CS theorem. It contains three different phases: condition on $\mathbf{x}$ phase, signal acquisition phase, and the digital recovery phase. Note that (T) is the transpose operation. 51
2.2 A generic overview of sampling by means of CS. 58
2.3 NUS protocol. The large circles represent time-domain samples. The NUS samples at irregularly spaced intervals, though always in multiples of Δt. 58

2.4 The block diagram of the Random Demodulator (RD) on the top, including the three main steps: modulation with $p_c(t)$ with a frequency $f_{\mathsf{p}} \geqslant 2f_{\mathsf{max}}$, filtering and low-rate uniform low-rate sampling with an ADC converter at a frequency $f_{\mathsf{s\text{-}s}} < f_{\mathsf{s}}$. On the bottom the frequency representation of each steps. Not that $\mathrm{m} \in \{1 \ldots \mathrm{M}\}$. 60
2.5 The diagram of MWC. 61

3.1 Time and Frequency domain representation of a cosine signal operation at a frequency $f = 8$ MHz ($x(t) = \cos(2\pi f t)$). We can notice that the FT of the $x(t)$ has a sparse representation with only 2 components at $|f| = 8$ MHz different from zero. 68
3.2 Representation of the linear chirp signal with a frequency range 0-50 MHz. 69
3.3 The (u, v) plane of FrFT rotated by an angle α relative to the original time-frequency plane (t, f). 70
3.4 This figure provides a different representation of a linear chirp signal. As the projection angle rotates to the optimal, the FrFT of the chirp signal converges to an impulse function. 72
3.5 Time domain representation of the injected signal with a bandwidth 0-50 MHz and the sparse representation of $x_i(t)$ using FrFT with the theoretically calculated angle of rotation $\alpha_{opt_i} = 1.815$ rad/s. Note that $\alpha_{opt_i} = a_{opt_i}\frac{\pi}{2}$. 74
3.6 In blue the choice of the $\alpha_{opt_i}$for the injected signal. The dashed line in gray represent the value of the calculated a_{opt_i}. Note that $\alpha_{opt_i} = a_{opt_i}\frac{\pi}{2}$. . 75
3.7 Time domain representation of the reflected signal in point-to-point wire and the sparse representation of $x_r(t)$ using FrFT while the theoretically calculated angle of rotation $\alpha_{opt_r} = 1.82$ rad/s. 76
3.8 The layout of the NUT considered, with a characteristic impedance $Z_c = 50\,\Omega$. The three lines [$\mathbf{B1}$, $\mathbf{B2}$, $\mathbf{B3}$] are of respective length [24,18,32] meters, where the extremities of $\mathbf{B2}$ and $\mathbf{B3}$ are charged by $Z_l \gg Z_c$. . . 77
3.9 Time domain representation of the reflected signal in a Y-Network and the sparse representation of $x_r(t)$ using FrFT while the theoretically calculated angle of rotation $\alpha_{opt_r} = 1.818$ rad/s. 78
3.10 Attenuations versus the frequency, where α_1 and α_2 are the attenuations of a different type for real case wires. 79

3.11 The sparse degree estimation of the reflected signal versus different frequency bands in a point-to-point wire. 80
3.12 The sparse degree estimation of the reflected signal versus different frequency bands in complex Y-Network represented in Figure 3.8. 80
3.13 Example of the signal $\mathbf{x}[\mathbf{n}]$ in time and DCCT domain and its reconstruction. 84
3.14 MCTDR signal representation in time and DCCT domain as well as the reconstruction error. 85
3.15 3-D plot of DCCT coefficients of MCTDR signal occupying a bandwidth of $[0-50]$ MHz. 87
3.16 3-D plot of DCCT coefficients of the reflected MCTDR signal occupying a bandwidth of $[0-50]$ MHz in point-to-point wire. 89
3.17 3-D plot of DCCT coefficients of the reflected MCTDR signal occupying a bandwidth of $[0-50]$ MHz in complex Y-Network. 90
3.18 Reconstruction error as a function of signal bandwidth for different types of wires in a point-to-point network. 90

4.1 The proposed compressive sampling architecture of reflectometry with RD. Where in the digital model of RD, $\mathbf{P}$ represents the ± 1 values of PRBS and $\mathbf{H}$ represents the impulse response of the low-pass filter as well as the sub-sampling. Not that $\mathrm{m} \in \{1 \ldots \mathrm{M}\}$ and $\mathrm{n} \in \{1 \ldots \mathrm{N}\}$. . . . 94
4.2 The Mixer ADL5391 [91]. 95
4.3 The low-pass filter ADRF6510 [92]. 96
4.4 The FPGA board: Red Pitaya. 96
4.5 Schema-bloc of the implemented reflectometry architecture. 97
4.6 The normalized reflectogram corresponding to high sampling frequency $f_s = f_{Nyq} = 2B$ for a point-to-point system, while the injected signal chirp occupies a bandwidth $B = 50$ MHz. 99
4.7 Influence of the maximum signal frequency on the accuracy of the fault localization. 99
4.8 Bounce layout of the NUT considered, with a characteristic impedance $Z_c = 50\,\Omega$. The three lines $[\mathbf{B1}, \mathbf{B2}, \mathbf{B3}]$ are of respective length $[24,18,32]$ meters, where the extremity of $\mathbf{B2}$ and $\mathbf{B3}$ is charged by $Z_l \gg Z_c$. . . . 100

4.9 The normalized reflectogram corresponding to high sampling frequency $f_s = f_{Nyq} = 2B$ for a Y-network system, while the injected signal chirp occupies a bandwidth $B = 50$ MHz. 101
4.10 The reflectogram for the chirp signal occupying a bandwidth of $B = [25, 50]$ MHz, where the influence of the maximum frequency of the injected signal on the detection and localization two nearby faults is represented. 102
4.11 A study on a chirp signal with a bandwidth $B = 50$ MHz for a sampling frequency $f_{\text{s-s}} = f_s/8 = 12.5$ MHz. 106
4.12 A study on an MCTDR signal with a bandwidth $B = 50$ MHz for a sampling frequency $f_{\text{s-s}} = f_s/8 = 12.5$ MHz. 106
4.13 The robustness of the fault localization with sampling frequency on the performance of the reflectogram's by evaluating the SINAD. 107
4.14 Reflected and reconstructed of sub-sampled signal with OMP at $f_{\text{Nyq}}/8$. 108
4.15 Reflectograms, in red (with CS) corresponding to low sampling frequency $f_{s\text{-}s} = f_{\text{Nyq}}/8$ and high in blue (without CS) corresponding to high sampling frequency $f_{s\text{-}s} = f_{\text{Nyq}} = 2B$. 109
4.16 Reconstructed reflectogram for four different bandwidths of injected signal where the sampling frequency is constant $f_{s\text{-}s} = 50$ MHz for the Y-network of branches length $[24, 18, 32]$ m. 111
4.17 Reconstructed reflectogram for four different bandwidths of injected signal where the sampling frequency is constant $f_{s\text{-}s} = 50$ MHz for the Y-network of branches length $[24, 18, 21]$ m. 113
4.18 The injected MCTDR and PRBS signals by the AWG. 114
4.19 Reflected signal multiplied with the PRBS, with blue by ADL5391 and with red numerically in MATLAB. 115
4.20 Filtered signal after multiplication at a $f_c = 12$ MHz, where the blue is filtered by ADRF6510 and the red is numerically filtered using the Butter function of MATLAB. 116
4.21 Reconstructed signal vs. standard reflected signal. 117
4.22 Reflectograms comparison approach between the measured, theoretical, and standard. 117
4.23 Reflectograms comparison approach between the half measured half theoretical, theoretical, and standard. 118

4.24 The impulse response of perfect integrator in temporal and frequency domain with cut off frequency $f_c = 12.5$ MHz. 119
4.25 Reflectograms comparison approach between the half measured-half theoretical, theoretical, and standard. 119

LIST OF TABLES

1.1 Probability of the appearance of defects in a cable according to age in aeronautics. 29
1.2 Summary of TDR based method specificities. 41

2.1 Summary of pros, cons and challenges of Nyquist and sub-Nyquist sampling. 50
2.2 Different quality classes of reconstruction according to the PRD [72]. . . 57
2.3 Summary of the various AIC encoders proposed based-CS architectures [84, 85]. 63

4.1 The SNR_{dB} for different compression factors and the relative errors $\delta\alpha_r$ of localization of defects at each point. 110

GENERAL INTRODUCTION

Context

The level of requirement on the online monitoring and reliability of the wired networks is remarkable with the increase of embedded applications. The LFIC (*Laboratoire Fiabilité d'Intégration de Capteurs*) of CEA LIST (*Laboratoire d'Intégration de Système et des Technologies*) mainly works on the strategies to improve and help the development of an onboard diagnostic system for electrical cable networks. They propose signal types for which the detection is possible while the target system is running [1, 2]. Moreover, not only they try to overcome the difficulty to overview cable aging, but they also study and develop methods to improve and ease the detection and location of soft wire faults [3]. However, the online diagnosis imposes serious challenges, such as the spatial resolution that depends on the maximum frequency of the injected signal. Therefore, in this thesis and with a collaboration with LS2N (*Laboratoire des Sciences du Numérique de Nantes*), we aim to find a solution for hardware limitation. Accordingly, based on a new methodology called Compressed Sampling (CS), a particular study on the reflected signal is applied.

Problem Statement

Wireless communication or transmission systems were introduced at the end of the 19th century. This technology has developed over the subsequent years and had masked the importance of wires. Consequently, so many questions arise about the utility and the importance of wires. They are a necessary element because they are responsible for transmitting the electrical power and signals in any transmission, communication, and power distribution systems. They may seem simple, but they come in many forms and are made from many materials. Power wires are usually present in building applications (e.g., public outdoor lighting, airports, hospitals, road and rail tunnels, ...) and industrial applications (e.g., nuclear power stations, ships). Thus, they are usually

used for long distances without time condition and often bared to rough environmental conditions like high thermal or mechanical operations, corrosion as well as some magnetic radiations. Those factors can change the nature of an initially healthy wire, and therefore, some defects may appear. In general, these latter are identified as defects on the cables, which represent an impedance mismatch into the wire. Based on the literature, they are classified according to their severity degree: hard faults, i.e. short or open circuits and soft faults, i.e. structural damage of wire without loss of electrical continuity. As a matter of fact, among all faults, the most difficult and dangerous diagnosis problems are those that occur only during a particular condition and are unable to be reproduced on the ground. Moreover, unlike other electrical equipment which are installed in clean, sealed and air-conditioned rooms, they are also buried underground or placed inside a tight tunnel where not only the visual inspection is impossible but also they are complicated to repair or replace. Hence to be in the secure zone and to gain some time, money, and precision, an online monitoring system for aging and degradation status is required for such networks. Among all the existing methods, from early 1960 till today, reflectometry became a traditional and familiar approach for detecting the impedance mismatches in any Network Under Test (NUT). The reflectometry systems triggered by the principle of radar as well as echography, where a particular test signal (low-voltage and high frequency) is injected into the wire. While the test signal travels the NUT and once it encounters a discontinuity this signal is reflected back to the injection point [4]. Therefore, a reflectometer, which represents a reflectogram, analyzes this reflected signal, where the mandatory information of the defect (location, type, and size) on the NUT is obtained. Reflectometry based techniques differ by the type of the injected signal and the analysis required to identify the defect. Meanwhile, a reflectometry based system is the most suitable method to apply the online diagnosis by its ability to integrate into the embedded system as well as its potential to test the network without causing any interference with other native signals. Also, the architecture of the embedded diagnostic system must take into account the whole measurement chain to the fault location. Moreover, In such case digital signals and processing module can be easily integrated into a Field-Programmable Gate Array (FPGA) or Application Specific Integrated Circuit (ASIC). Nevertheless, this integration of the diagnosis revealed severe constraints related to the size and the cost of the diagnostic system as well as to the complexity of the processing (bandwidth, sampling frequency, ...). Yet, the performance of the reflectometry setup is evaluated by

its resolution and its accuracy. However, to detect defects with better spatial resolution, certain types of faults or complex cable networks, the injected signal must cover a very wideband of frequencies. Thus, during its injection or acquisition and, in order to respect the Shannon theorem, the signals must be sampled by a Digital-to-Analog Converter (DAC) and Analog-to-Digital Converter (ADC) at a frequency of several hundred of MHz. Therefore embedded diagnosis systems present significant challenges in building sampling hardware that operates at a sufficiently high rate to analyze the result from the high frequency reflected signal. With current hardware technologies, high-rate sampling systems are difficult to implement and are costly [5]. Additionally, an adequate ADC samples an enormous amount of information, which in real-time increases the complexity and the cost of the diagnosis system. The objective of this thesis is to propose as well as evaluate a new architecture for the embedded diagnostic system for any wired networks that optimize the performance, cost and improves the spatial resolution of wire diagnostics. This research explores the use of new sub-Nyquist architectural approach for reflectometry systems to apply signals with higher bandwidth, thus, an enhancement of the precision and the accuracy of localization of any defect appearing on the NUT.

Based on similar problematics, in 2006, a new technique referred to as Compressive Sampling (CS) was introduced in the signal processing by Donoho [6] and Candès et al. [7]. They proposed a new, nonlinear sampling theorem, stating that a sufficiently sparse signal can be sampled or digitized directly at a frequency much lower than the one required by Nyquist-Shannon theorem. Therefore, and in order to compress and reconstruct the compressible signals, one of the challenges required by the CS is to work with those which have sparse representations in some specific bases or domains. However, for continuous-time signal acquisition, Analog-to-Information Converters (AIC) was proposed by Tropp et al. [8] that recalls the CS context and defines the measurement matrix. In general, all of the AIC architectures have an analog encoder, which is followed by a uniform low rate ADC converter. On the other hand, unlike the measurement phase, the reconstruction phase of the CS requires demanding computational algorithms. Consequently, the complexity of the measurement phase is deported to the reconstruction phase. The main challenge that will be addressed in this work is the setting of adequate dictionaries allowing a sparse representation of multi-carrier signals involved in wire diagnosis by reflectometry and the proposal of a complete architecture for the implementation of the resulting signal acquisition scheme

based on compressed sensing. The first contribution is, therefore, the proposal of two dictionaries suitable for complex and real signals defined for reflectometry systems to diagnosis network maintenance. The second contribution is to adapt the analog implementation of compressed sensing for reflectometry systems, where we simulate and evaluate their performance, then study their implementation. The simulations will be based on a model to be developed for the architectural approach and on a model of the cable on existing codes. Finally, the third contribution is to propose first experimental results on wire diagnosis based on the whole architecture using the laboratory equipment at first and then by an FPGA prototyping. However, more developments will be required to complete and validate this architectural approach.

Thesis Organization

The diversity of the themes treated in this thesis makes the chapters complementary but not always dependent on each other. Therefore, this thesis is developed into four chapters, as follows:

Chapter 1: introduces an overview of the first context of our study, wire diagnosis by reflectometry. First, by a brief introduction, we present the main reasons behind the appearance of wiring faults. After that, we detail the typologies and the instantaneous damage rate of defects such as hard faults, soft faults, and aging. We focus mainly on the concept of integrating diagnostics systems based on reflectometry into embedded architecture, which provides the opportunity to apply and improve online monitoring. To better understand the principle of reflectometry, we recall the principles of wave propagation along transmission lines. The general principle of reflectometry based techniques is presented with their two varieties: the time domain and frequency domain reflectometry methods. In which, we illustrate their significant advantages and disadvantages. Finally, in this chapter, the necessity to use high-frequency signals as well as their limitation based on conventional architectural approach is discussed.

Chapter 2: presents the second context of this study, the CS. After a brief overview of works applying the idea of CS, the chapter begins on the basic principles of CS, in which we discuss one of the main principles: the sparsity. Next, we discuss the required properties that the measurement matrix should satisfy, as well as some commonly used reconstruction algorithms. This chapter generalizes CS to a reduced sampling rate of an analog signal. It introduces the various analog encoders, AIC, proposed in

the literature. Our main focus is on the Random Demodulator (RD) architecture, which was the first proposed hardware implementation for CS.

Chapter 3: addresses the first contribution of the thesis, where the search for a domain or a base allowing a very low degree of sparsity. Generally, the time-frequency transform domains are the most used, but we go beyond the standard to find the sparse dictionary and introduce different dictionaries for different types of signals. The idea of finding the sparseness dictionary is motivated to decrease the sampling frequency because the more the signal is sparse fewer samples are needed to rebuild it correctly. Taking into consideration the advantages of Multi-Carrier (MC) signals for reflectometry, we investigate two kinds of signal. We present the study for complex chirp signal and the real MC signal where we decide to use the Fractional Fourier Transform (FrFT) and Discrete Cosine Chirp Transform (DCCT) respectively. In this context, we detail the theoretical approach of FrFT and DCCT, then the results obtained by this transformation. We employ the two most widely used performance metrics, namely the Compression Ratio (CR) and Percentage Root-mean-Square difference (PRD).

Chapter 4: details the second contribution of the thesis. It examines the validity of the methodology and the choice of the analog encoder proposed by CS, which offers the low-rate sampling. The standard three phases of AIC will be recalled while showing its feasibility in locating and detecting the defect with a low rate of ADC. First, the study is applied to a point-to-point complex network in which we vary only the sampling rate in order to study the limitations of the under-sampling. Second, for the sake of improving the resolution of the system or else to detect the nearby defects, we maintain the sampling frequency constant while we increase the frequency of the injected signal. In fact, the last part of this chapter will be dedicated to the last contribution, where the experimental approach and the limitations of it for a point-to-point wire are studied.

Finally, a conclusion and a final discussion, as well as directions for future research, will be discussed.

Publications

The work of this thesis has been published in three conferences and one journal paper, listed below:

[1] T. Ajamian, S. Moussaoui, and A. Dupret, “Échantillonnage comprimé pour le

diagnostic filaire par réflecométrie", *in: Actes du XXVIéme colloque GRETSI sur le Traitement du Signal et des Images*, Juan-Les-Pins, France, Sept. 2017.

[2] T. Ajamian et al., "Compressed signal acquisition in wire diagnostic", *in: 2017 IEEE SENSORS*, pp. 1–3, Oct. 2017, DOI: 10.1109/ICSENS.2017.8234017.

[3] T. Ajamian, S. Moussaoui, and A. Dupret, "A Novel Compressive Sampling Approach for Detecting Hard Defects in Complex Wire Networks", *in: 2018 IEEE AUTOTESTCON*, pp. 148–151, Sept. 2018, DOI: 10.1109/AUTEST.2018.8532534.

[4] T. Ajamian, S. Moussaoui, and A. Dupret, "Breaking nyquist limitations in reflectometry-based wire diagnosis systems by compressive sampling", *in: IEEE Instrumentation & Measurement Magazine*, vol. 22, no. 4, pp. 3-9, Aug. 2019, DOI: 10.1109/MIM.2019.8782192.

[1] and [2] are mainly based on the first approach of applying the CS to reflectometry-based systems, mainly, using a complex chirp signal for a point-to-point network. Eventually, this idea was developed and applied for complex Y-Network that took part in an international conference [3]. This latter was awarded as a Best Student Paper and gained the opportunity to be published in a journal paper, where the performance of such an application combination is discussed. Moreover, a journal paper is in preparation where various strategies (type of signal, choice of filter, sparseness degree, etc.) will be examined.

CHAPTER 1

PRINCIPALS OF WIRE DIAGNOSIS BY REFLECTOMETRY

1.1 Introduction

Electrical cables are covering many fields of applications where they are often exposed to rough environments, run over long distances, and are intended to work for several decades. Certain of those factors modified the characteristics of cables; hence, the nominal functioning and the good performance of a system are not guaranteed. Therefore, cable faults can be a severe problem, also depending on the application, they are usually hard to repair or replace. In this context, the online non-destructive monitoring systems for cable diagnosis must be used.

In this chapter, after mentioning some cumulative length of cables required in specific applications and their catastrophic consequences, we are going to present the types of faults. They are categorized depending on their severity and the impact that causes to the system. This chapter is followed by a fault location technique, in which we focus mainly on reflectometry based methods. In order to better understand the reflectometry principle, we introduce the framework of the transmission line in the context of the wiring modeling techniques. Then we focus mainly on the types of the signal used and analysis applied either in the time domain or frequency domain. Notably, in this thesis, we are interested in embedded wire diagnosis techniques applied in reflectometry; thus, we explain the hardware implementation step by step as well as its requirements and limitations.

1.2 Wiring faults: hard faults vs. soft faults

Transportation systems, vehicles, or infrastructure, are made up of a large number of interconnected components, which requires substantial wired connections carrying energy or data flows to communicate with each other. Electrical cables are also present in nuclear power plants, industrial machinery, and buildings. In fact, the choice of cables may vary; it depends on the nature of the transmitted signal, the length of the network, and the environment in which the network operates. Generally, the nature of the transmitted signals can be either analog or digital [9], having low or high power, propagating at low, medium, or high frequencies. For instance, a computer network can use three types of cables: the coaxial cable, the twisted pair, or the optical fiber [10]. Nowadays, we notice an enormous increase in the cumulative length of cables, especially in transportation fields. Evidently, in automobiles, the cumulative length of embedded cables has exceeded the 4 Km. In the public transportation "high-speed train" (French: *Train à Grande Vitesse, TGV*), this average length reaches 200 km. This phenomenon is also present in the field of avionics, where cable lengths exceed several hundreds of km in modern aircraft (nearly 40 km for the Rafale and 530 km for the Airbus A380). This increase has led to complexity in wired networks making the maintenance operation very complex [11].

Another critical point is the environment in which the cable is placed. It can widely vary between air, as for power transmission networks, the sea, as internet cables, or underground as for power cables. However, underground cables are mostly affected by thermal, electrical, mechanical, and environmental stresses [12]. Over time, these various constraints cause more or less severe modifications in the insulation of the underground cable. Moreover, in France in 2010, 66% of new lines were built underground [13].

Malfunctions in any connections induce abnormal behaviors of the global system. This results in an incorrect transmission of information that is used by the control system and the supervision system. Without taking into consideration the aging factor, there are two leading families for wiring faults: hard faults and soft faults.

1.2.1 Hard faults

Hard faults are responsible for severe malfunctions of the system and can have dramatic consequences. They are characterized by the fact that they prevent any signal from going further away due to significant variation of the characteristic impedance of the cable. They manifest themselves by a total interruption of the flow of energy or information in the damaged cable. A significant variation of the cable parameters is represented as open or short circuits. Figure 1.1 shows examples of hard faults in aeronautical cables [14]. The open circuit is an electric circuit that has been broken due to mechanical damage or violent movements of the cable. As for the short circuit, due to damaged insulation, it is simply a low resistance connection between the two conductors supplying electrical power to any circuit. In 1999, the US NAVY published that during electrical cable maintenance, 37% relates to hard faults (18% short circuits and 11% open circuits) [15].

(a) Cut wire (Open circuit).

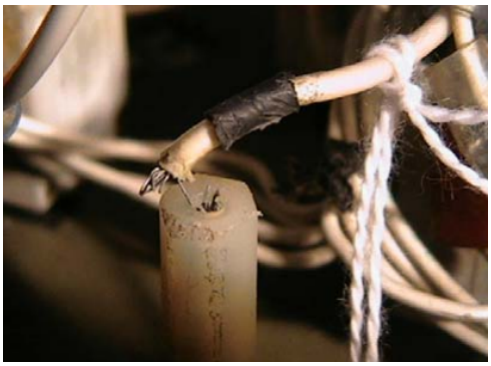

(b) Breaking a conductor.

Figure 1.1: Hard faults in aeronautical cables [14].

1.2.2 Soft faults

Soft faults, namely friction, insulation damage, cracks, etc. will not stop the transmission of energy. However, the quality of its transmission will depend on the state of the degradation of the cable. Basically, any fault which is not considered as a hard shall be defined as a soft one. Those faults are usually more difficult to detect [16, 17]. Therefore, soft faults are characterized by a slight variation in the characteristic impedance of the cable. These degradations do not always lead to severe breakdowns since they

do not prevent the flow of energy or information, but in long-term, they may be a preliminary step towards the occurrence of hard faults following mechanical aggression, environmental constraints (penetration of the humidity, heat stress, etc.) or the aging of the cable.

In fact, during the life cycle of an aircraft, new failure scenarios are discovered that must be addressed in order to meet safety design requirements. A report shows that about 30 to 50% detectable wiring damages of wires rely on chaffing [18]. Figure 1.2 illustrates a progressive chaffing of an aircraft cable. In the begging, after 4 K cycle, a soft fault appears into the cable. Once for all after 6 K, this permanent defect developed and became a hard fault leading to a catastrophic accident if not early rectified.

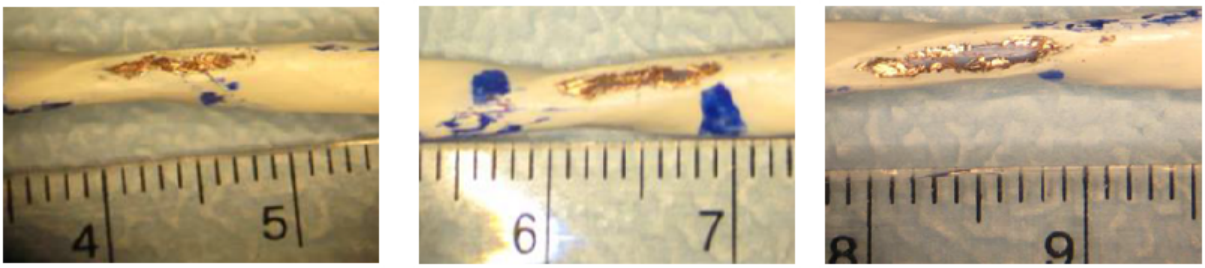

(a) 4 K cycles: the shield is relatively intact.

(b) 6 K cycles: holes start to appear in the shield.

(c) 10 K cycles: the inner dielectric is scraped but intact.

Figure 1.2: A progressive chafing example of an aircraft cable during a flight cycle [16].

Besides, other than those two critical families of defects, one should admit the existence of the aging factor. The environmental degradation can accelerate and affect the aging of the wire insulator over time through the effects of humidity, temperature, and even exposure to the sun. Therefore, a modification in the physical and mechanical properties of the conductor occurs for the aging wire. In 2003, an American study showed that there is a very close relationship between the number of cable-related problems and the age of civilian or military aircraft [19], where the probability that a wiring defect appears in a plane increases with time (Table 1.1).

Actually, the life-cycle of a wire can be represented in a bathtub curve. The bathtub curve is a type of model demonstrating the likely failure rates of all devices. Over a certain product lifetime, the bathtub curve shows how many units might fail during any given phase of a three-part timeline. According to the type of defects and their severity, a wire is subject to the three standard phases of a life-cycle: mortality phase, useful lifetime, and wear-out phase [20]. As illustrated in Figure 1.3, the mortality phase is

Table 1.1: Probability of the appearance of defects in a cable according to age in aeronautics.

Age (years)	Probability (%)
5	35
10	52
20	66

assigned for hard and some types of soft defects where the damage rate is severe. This instantaneous damage rate decreases in some types of soft defects; thus, the damaged system can function normally; hence, it gives the system a useful lifetime. The final portion is dedicated to the aging factor. This is the wear-out phase; in other words, the end-of-life, where the performance of the wires is reduced, eventually an increasing failure rate.

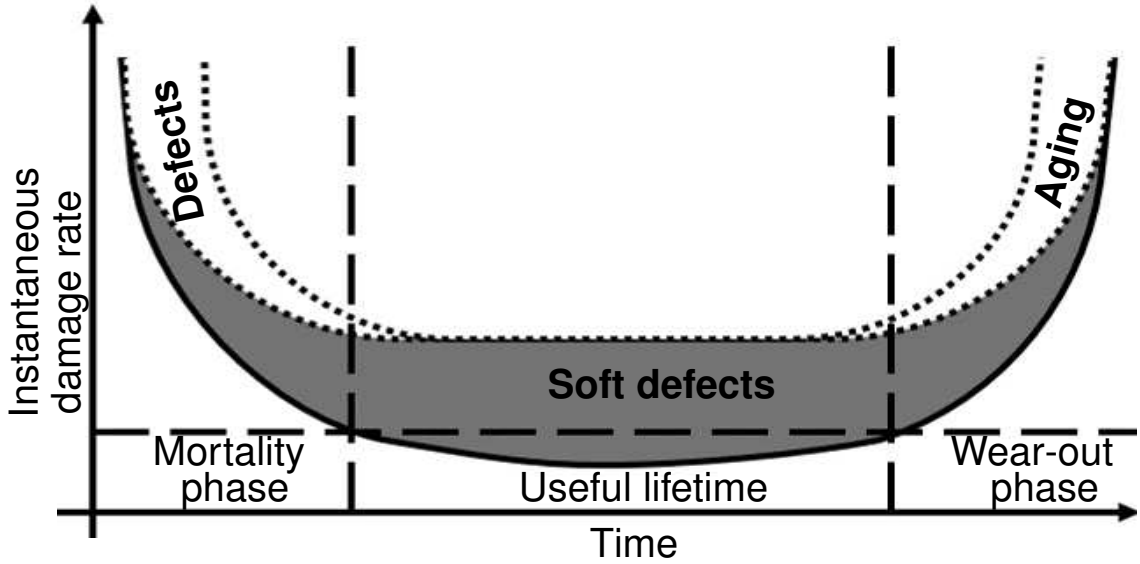

Figure 1.3: Instantaneous damage versus the time phases (mortality phase, useful lifetime and worn-out phase) of different type of defects.

In many application domains, particularly critical systems for the safety of people, equipment, or even the environment, wire faults can have highlighted the potentially catastrophic consequences. The two most known events TWA 800 (in 1996) and Swissair 111 (in 1998) took the lives of hundreds of peoples where the accidents are at-

tributed to the aging factor of wire and the arcing on the wire, respectively [20]. Also, on August 9, 2007, a flight 1121 of the company Air Moorea crashes with 20 people on board. The accident, due in particular to a cable break, occurred during takeoff. Moreover, there are almost 2 million working hours dedicated to finding and fixing wiring problems in the Navy [21]. A report for 737 Boeing airplane indicated that chafed wires through the Teflon and the damaged power cable of a fuel boost pump were notices after approximately 21 thousand flight hours instead of an interval of 30 thousand flight hours [22].

To be in the safe zone, to save time and money, and for dependability reasons, it is crucial to detect and localize these connection faults as early and as accurately as possible. Consequently, the US government has encouraged industries and universities to develop intelligent detection, diagnostics, and prevention systems to detect cable faults [23].

1.3 Fault location technique by reflectometry

The section above demonstrates the existence of different types of defects in cable networks and the real cause of their appearance. To get information about the health condition of the NUT and to anticipate the detection of faults (hard or soft faults), a monitoring system is required. Several wire diagnosis methods have been developed. Even though the most insured method is based on the visual inspection [24], sometimes it is difficult as it may be impossible, mainly when the wires are buried underground, placed inside a tight tunnel or hidden. Besides, inspection techniques are often tedious and challenging. For those reasons, cable diagnosis monitoring systems are necessary, where they provide high reliability and low maintenance cost at the same time. Based on the state-of-the-art of wire fault detection techniques, they can be categorized into several classes; online and offline, destructive and non-destructive, and so on. The offline diagnosis does not allow a wire to be scanned when it is connected or when other signals are present. Depending on the application, this method can be very restrictive (e.g., vehicles). While the online diagnosis allows inspection of the wire condition when other native signals are transmitted.

In this case, the difficulty is to not disturb the electronic systems connected to the wire. From early 1960 till today, reflectometry became a traditional and familiar approach for detecting the impedance mismatches in the NUT. Besides, The reflectometry based

techniques have presented useful results compared to other traditional methods. In the following sections, first, we recall the principles of wave propagation along transmission lines. Then, we detail the two families of reflectometry based techniques: the Time Domain Reflectometry (TDR) and Frequency Domain Reflectometry (FDR). They are mainly different from the type of injected testing signals and the analysis techniques. Finally, we discuss the present hardware approach of reflectometry architectures, which possess the component that limits the performance and accuracy of the inspection.

1.3.1 Reflectometry's concept

The reflectometry, a non-destructive and a single measuring point technique, consists of injecting a particular test signal (low-voltage and high frequency) down the wire and analyzing the reflected signal caused by the discontinuities along the wire and the end of the wire. Consequently, the analysis of this reflected signal gives rise to a reflectogram from which the mandatory information of the defect (localization, type, and size) on the medium under consideration is extracted [11], Figure 1.4. If we consider a point-to-point wire with a characteristic impedance $Z_c = 50\ \Omega$ and present a defect at $50\ \mathrm{m}$, see Figure 1.5 shows its impulse response, i.e. the reflectogram, for different impedances (Z_f).

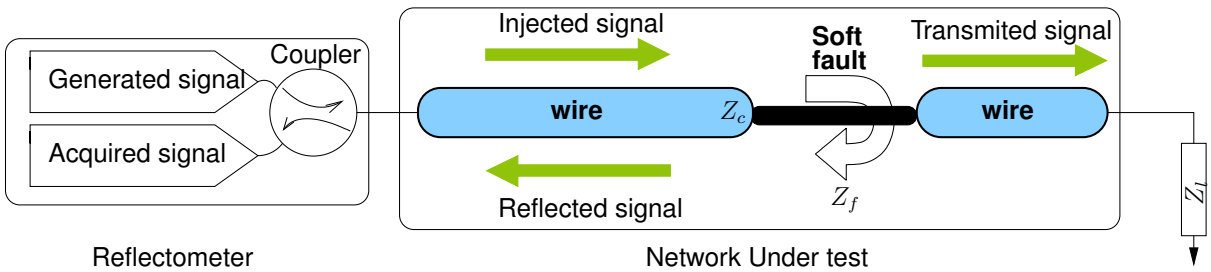

Figure 1.4: A scheme showing the principal of reflectometry.

So, in general, this concept of reflectometry, in which $x_i(t)$ represents the injected signal at the input of the line with a response of the channel $h(t)$ and $x_r(t)$ the reflected signal is expressed as follows:

$$x_r(t) = x_i(t) * h(t). \tag{1.1}$$

The operator $(*)$ represents the convolution product. In fact, compared to $x_i(t)$, $x_r(t)$ is attenuated due to the electrical properties of the channel and delayed by a propagation

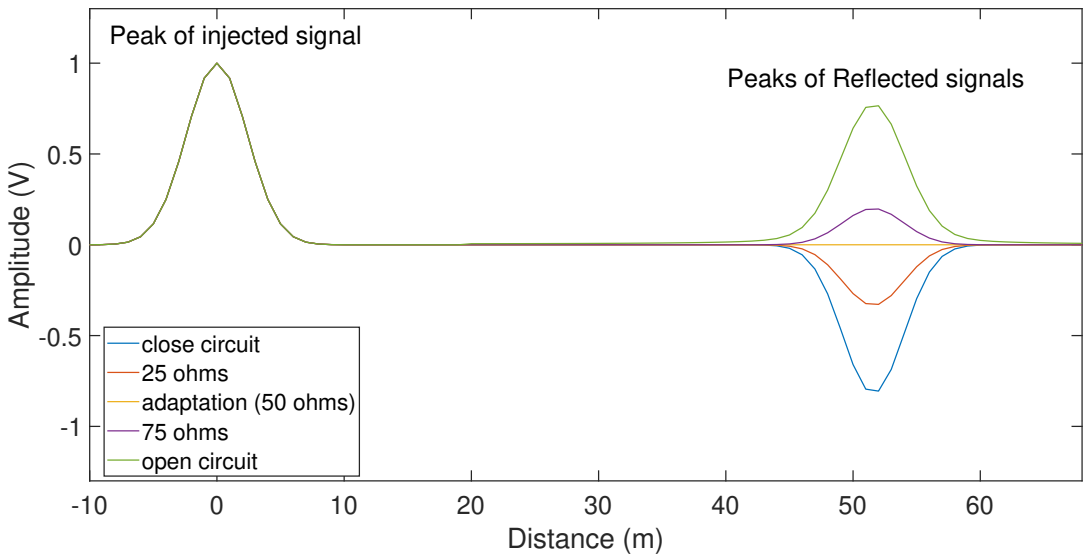

Figure 1.5: A reflectogram showing the responses of reflected signal for different impedances at $50\ \mathrm{m}$ where $Z_c = 50\ \Omega$.

time τ, which corresponds to the round trip time between the injection plane and the discontinuity. There are a variety of transmission lines that can be interrogated. Propagation of voltage pulses along with these cables, as well as the creation and characteristics of reflected pulses, can be described using circuit theory or Maxwell's equations of electromagnetic wave theory. A more detailed study about Maxwell's equation and more specifically an inverse-problem approach to estimate the cable parameter from a reflectometry is detailed in [25]. However, we are working on high frequencies where the wavelength λ is less than the length of the line, so the amplitude of the wave is no longer constant throughout the line. This analysis is based on using the concept of propagation in physical media. Modeling the wiring system consists in calculating the voltage potential to identify the equivalent electrical parameters ($RLCG$): R the resistance per unit length, L the inductance per unit length, C the capacitance per unit length, and G the conductance per unit length. Furthermore, the propagation study in high frequency, which needs to apply on an infinitesimal length section dx of the line, gives the lumped elements of this section, as illustrated in Figure 1.6.

This modeling approach and these parameters lead to identify the Telegrapher's equation [26]. We consider as excitation a sinusoidal pulse wave $\omega = 2\pi f$ where f is

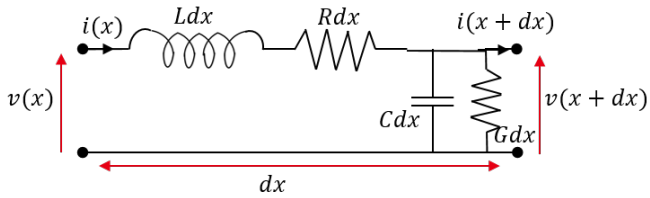

Figure 1.6: Equivalent circuit of a small part of a transmission line, showing the per-unit-length parameters R, L, C, and G.

the frequency. In this case, the current and voltage waves are given, respectively, by:

$$v(x, \omega, t) = V(x, \omega) \exp(j\omega t), \tag{1.2}$$

$$i(x, \omega, t) = I(x, \omega) \exp(j\omega t), \tag{1.3}$$

where $V(x, \omega)$ and $I(x, \omega)$ represent the complex amplitudes associated with the voltage $v(x, \omega, t)$ and the current $i(x, \omega, t)$, respectively. The solution of those equations leads to determine the two wave equations (1.4) and (1.5), to compute the complex propagation constant (γ), the characteristic impedance (Z_c) of the wire, and the reflection coefficient (Γ) [27]. An in-depth study of those equations is presented in [28].

$$\frac{\partial^2 V(x,t)}{\partial t^2} - \gamma^2 V(x,t) = 0, \tag{1.4}$$

$$\frac{\partial^2 I(x,t)}{\partial t^2} - \gamma^2 I(x,t) = 0, \tag{1.5}$$

where, γ is the complex propagation constant given by:

$$\gamma = \sqrt{(R + j\omega L)(G + j\omega C)} = \alpha + j\beta, \tag{1.6}$$

with α and β being the attenuation constant in Nepers/m and the phase constant in radians/m, respectively. Moreover, $\omega = 2\pi f$, f being the cyclic frequency of excitation. We can notice that α, the attenuation constant, is directly related to the excitation frequency; hence, the attenuation will be remarkable on high frequencies. Solving these partial differential equations (1.4) and (1.5) results to determine the voltage and current all along the line. Thereupon, on a particular position, the ratio between the voltage and current of a wave traveling along the line is its corresponding characteristic impedance,

Z_c, given as:

$$Z_c = \sqrt{\frac{R + j\omega L}{G + j\omega C}}. \tag{1.7}$$

In general, depending on the cable type, it has a standard or predefined value at least at low frequencies (for α negligible). Meanwhile, as mentioned in the preceding sections, the detection of a reflected wave occurs only when it exists an impedance discontinuity within the line. For instance, the characteristic impedance of the transmission line is Z_c, and at the position d on the cable the impedance of the fault is Z_f ($Z_c \neq Z_f$), the reflection coefficient $\Gamma(x)$ is defined as:

$$\Gamma_f(x = d, \omega) = \frac{V_{reflected}}{V_{incident}} = \frac{Z_f - Z_c}{Z_f + Z_c}. \tag{1.8}$$

Indeed, the value of this reflection coefficient varies with the fault's severity. Certainly, hard faults, whether open ($Z_f = \infty$) or short ($Z_f = 0$) circuits, result in total reflection coefficient, $|\Gamma| = 1$. As well as, when $\Gamma = 0$, this is translated to a matched load circuit $Z_c = Z_l = Z_f$. Since, soft defects result for a $|\Gamma| < 1$, the softer the defect is, the smaller the value of Γ becomes. In this circumstance, the coefficient of transmission is expressed as $T_f(x = d, \omega) = 1 + \Gamma_f(x = d, \omega)$. Moreover, the elapsed time, τ, between the injected and reflected wave, permits also to locate the position d of the defect.

$$d = \frac{\tau v_p}{2}, \tag{1.9}$$

where v_p is the wave propagation velocity. In the case of a lossless transmission line ($R = G = 0$), it is given as follows:

$$\beta = \omega\sqrt{LC} \Rightarrow v = \frac{\omega}{\beta} = \frac{1}{\sqrt{LC}}. \tag{1.10}$$

In practice, usually, the values of L and C are hard to determine. For this reason, in reflectometry, it is often a sufficient approximation to consider $v = \frac{2}{3}c$, in which c is the light velocity.

1.3.2 Reflectometry based methods

The state-of-the-art of reflectometry based methods for wire or cable fault detection can be categorized into two wide families. The difference between those methods lies

in the type of injected waveforms and the methods used for the analysis of the reflected signal. The analysis of the reflected signal is performed either in the time or in the frequency domain.

1.3.2.1 Reflectometry techniques based on the frequency domain analysis

Frequency Domain Reflectometry (FDR) methods, usually applied in radar applications, use a set of stepped frequency sine waves signal, known also as chirp signal, and locate the defect by the interpretation of the reflected signal or the stationary signal formed by the interference of the injected and reflected signal [29][11]. This linear chirp signal, illustrated in Figure 1.7, is given by the following expression:

$$\begin{aligned} x_i(t) =& A\sin(\theta(t)+\phi), \quad \text{where} \quad \theta(t) = \int_0^t 2\pi f(u)du, \\ f(t) =& f_{\text{min}} + \frac{f_{\text{max}} - f_{\text{min}}}{t_{\text{max}}} t, \quad \text{such that} \quad 0 \leq t \leq t_{\text{max}}, \end{aligned} \tag{1.11}$$

where, $\theta(t)$ is the instantaneous phase and $f(t)$ is the instantaneous frequency that varies between f_{min} and f_{max}.

FDR techniques directly measure the network response in the frequency domain by evaluating the frequency, phase, or amplitude to determine the position of an impedance discontinuity. Note that, these types of measurement need to apply an Inverse Fast Fourier Transform (IFFT) in order to have the impulse response in the time domain, in particular for the analysis of the reflection coefficients of each discontinuity.

●Frequency-Modulated Continuous-Wave (FMCW)

The electronics of the FMCW uses a Voltage-Controlled Oscillator (VCO) or other sine wave generator, to inject periodically into the wire a high-frequency sine wave in which the frequency increases linearly with time ($\partial f = f_{\text{max}} - f_{\text{min}}$) [30–32]. Once this signal meets a discontinuity, it reflects into the injection point. A directional coupler separates the injected and the reflected wave. In this method, the principle consists in measuring the frequency offset ΔF between the incident signal and the reflected signal delayed temporally by Δt. The relation between ΔF and Δt is given as:

$$\Delta F = \frac{\Delta t}{T} \partial f, \tag{1.12}$$

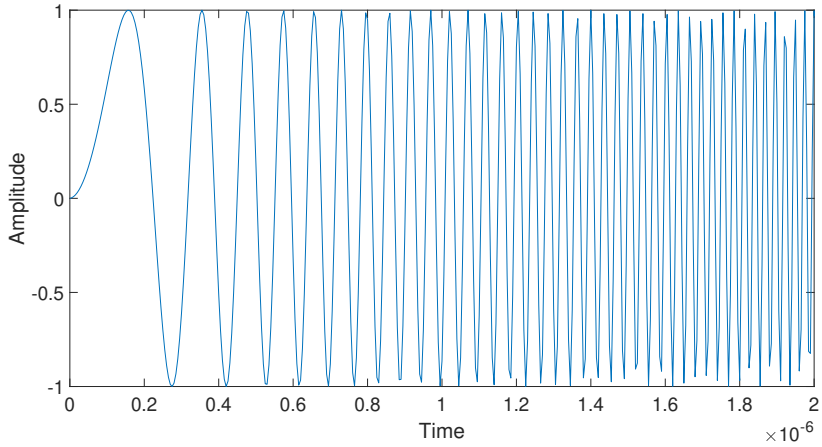

Figure 1.7: An example of a linear chirp signal occupying a bandwidth of 50MHz for FDR implementation.

where T represents the period to generate the sine wave occupying a frequency ∂f. Hence, the distance in which the reflection has occurred is calculated:

$$d = \frac{v\Delta t}{2} = \frac{vT\Delta F}{2\partial f}. \tag{1.13}$$

Unfortunately, this method is successful only for a significant reflection coefficient (hard defect) [29]. Also, it needs high-frequency sensors that can detect and calculate the frequency difference between the injected and the reflected signal (typically in the range of hundreds of megahertz to few gigahertz).

●Standing-Wave Reflectometry (SWR)

SWR injects a high-frequency sine wave signal down the wire. This strategy does not separate the injected wave from the reflected one. Thus, the combination of the injected and reflected waves produces a standing wave on the cable [33, 34]. The process to determine the location and type of the load on which the reflection took place, consists of analyzing the amplitude behavior of the formed standing wave at the minimum points. The first technique is sensitive to the noise. Another procedure can be used to locate a fault; it is based to send a set of a stepped-frequency sine signal and observe the point of minimum and maximum.

●Phase Detection FDR (PDFDR)

PDFDR is similar to FMCW because it separates the injected wave from the reflected one, but instead of measuring the frequency shift as done in FMCW, it measures the

phase shift. So, a set of sine waves is injected, which is reflected on the end of the cable or another discontinuity [34, 35]. After multiplying the reflected signal with a copy of the injected signal, a two-frequency component signal is obtained: the high-frequency and DC component. Applying a Fast Fourier Transform (FT) to the DC component, which varies sinusoidally as the frequency is swept linearly, the length of the cable or the distance of a defect is obtained. The alternative method of PDFDR is Mixed-Signal Reflectometry (MSR). The concept of MSR is similar to PDFDR but does not require a directional coupler to separate the incident wave from the reflected signal. [36] details the theoretical approach and also presents the block diagram of those methods.

However, FDR methods are expensive because they need high-frequency electrical components. Moreover, FDR methods can be used on live wires, as long as the test frequency is not within the frequency range of the existing signals on the wire. They are also unsuited to complex topology networks due to multiple combinations of shifted signals, which are complicated to analyze. They are instead intended for significant discontinuities, which reflect almost all the energy of the signal. Besides, it applies a time-domain transformation in order to characterize the type of the defect.

1.3.2.2 Reflectometry techniques based on the time domain analysis

Time Domain Reflectometry (TDR) injects a voltage having a very short rise time, typically a voltage step or a pulse along a wire. Among all the other methods (FDR or the derivative of TDR), it is the simplest and fastest because the direct analyzes of the echoes present in the reflected signal allow identifying the defect [4]. For instance, measuring the round trip time delay between the incident and the reflected echoes τ and recognizing the velocity of the propagation v_p of the wire, allows determining the position of the fault d (equation (1.9)). Unlike the FDR methods, TDR shows a good performance in any network (whether point-to-point or complex network). Nevertheless, soft faults, giving rise to the reflected signal with a small amplitude of reflection, are difficult to detect [37, 38]. Often, standard TDR satisfied an offline diagnosis that acquires an interpretation of a person. Moreover, it demands a total interruption of the network to perform its diagnosis. However, recently, the development of more advanced digital processing procedures took place. Furthermore, the propagation of high-frequency signals is more attributed to two phenomena: attenuation and dispersion. First, since in real life, lossless wires do not exist; therefore, due to the resistance of the wire, the amplitude of the pulse incident signal is attenuated. It is manifested by the decrease

of its amplitude during its propagation and thus limits the performance of the diagnosis regarding cable length. Besides, the fact that a soft defect (arch) has a small reflection coefficient and the incident signal is attenuated; thus, the reflected signal gets disappeared. Second, the dispersion can be explained by the modification of the phase constant depending on the frequency; therefore, the propagation velocity changed. Indeed the precision of the localization of the pics is lost because the dispersion distorts and flattens the pulse signal. To overcome the last attributed limitations of pulse wave TDR methods, state-of-arts suggested alternative signal types.

●Sequence TDR (STDR) or Spread Spectrum TDR (SSTDR)

STDR and SSTDR were introduced in 2005 and were the first methods to be feasible for use on the live wire without interfering with the service signals, considering the strategy of frequency translation that moves the spectral support of the test signal around a carrier frequency [36, 39–41]. Unlike the standard reflectometry-based methods that require to use high-frequency signals, they use high-speed digital signals. The principle of STDR is to inject into the cable a Pseudo Noise (PN) while (SSTDR) also injects a PN sequence but modulated by a sine wave. Then, the correlation between the measured reflected wave (a combination of incident and reflected waves) and a copy of the test PN injected code is calculated. The correlation that is calculated is the impulse response of the cable; thus, this correlation data provides the distance and the type of the defect into the wire. Indeed, using the PN sequence as a test signal provides some advantages. First, the fact that the signal to be injected is very low amplitude, its statistical properties imply that it does not correlate with the native signals on the network. Second, while the pulse TDR requires to send a very high power signal over a short time interval, injecting a low amplitude, PN prevents to circumvent the practical difficulty of high power injection. So, if we take the case of a Dirac function, the energy is:

$$E_{\text{TDR}} = A^2 T, \tag{1.14}$$

where A is the amplitude of the signal and T is the impulse period. However, the energy obtained by pulse compression becomes:

$$E_{\text{STDR}} = A^2 T_x \mathbb{E}, \tag{1.15}$$

where $\mathbb{E}$ represents the average power of the signal and T_x is the time duration of this signal. Thus, for the same amplitude, it is possible to increase the signal strength by

increasing its time duration. Third, it shows also good feasibility to detect hard faults and some soft faults that produce significant reflections. In fact, SSTDR is more accurate and precise than STDR because the correlation peaks are sharper. A similar architectural technique related to as Noise Domain Reflectometry (NDR) [42], uses as an incident signal the noise or high-speed signals already present in the wire. The concept to locate the distances of faults remains the same, the correlation (multiplier and an integrator) function between the incident wave and the reflected wave estimates the time delay; hence, the fault distance. In fact, it avoids the problems of interference and reduces the overall architecture of a reflectometer but, the location precision and accuracy depend directly on the bandwidth of the signal on the cable.

●Multi-Carrier signal based reflectometry

The objective of using MC signals is to execute an online diagnosis during the normal operation of the system. To perform the measurement, Multi-Carrier Reflectometry (MCR) [43] or Multi-Carrier TDR (MCTDR) [1, 44] uses an arbitrary band of simultaneous frequencies with phase aligned. This allows fitting the signal to application constraints. With MCR, the magnitude of each component in the frequency domain of the testing signal is controlled independently, which can be reduced or canceled due to some constraints. Therefore, the MCTDR method is based on controlling the energy of the spectral distribution of the injected signal. The injected signal x_n is defined for a given system as a sum of sinusoids by adjusting the amplitude and phase of each of them.

$$x_n = \frac{2}{\sqrt{N}} \sum_{k=1}^{N/2} c_k \cos\left(\frac{2\pi k}{N} n + \theta_k\right), \tag{1.16}$$

where c_k and θ_k are the amplitude and the phase of each sinusoidal component, respectively. The amplitude allows to control the spectrum of the test signal, and is set to 1 for the non-forbidden band and 0 for the band already used. The phase is calculated by a specific method to minimize the peak to peak amplitude in the time domain. Figure 1.8 illustrated an example of the MCTDR signal.

Since the signal bandwidth can be controlled, therefore firstly, it is defined in the Fourier domain, and then the time domain signal x_n is obtained by applying the IFFT. From the measured reflected signal, an approximation of the impulse response of the cable is constructed. Yet, the secondary lobes appearing in the autocorrelation function of the signal mask real echoes in the final result. Therefore post-processing is needed to remove this distortion. The post-processing may appear in different axes. Under

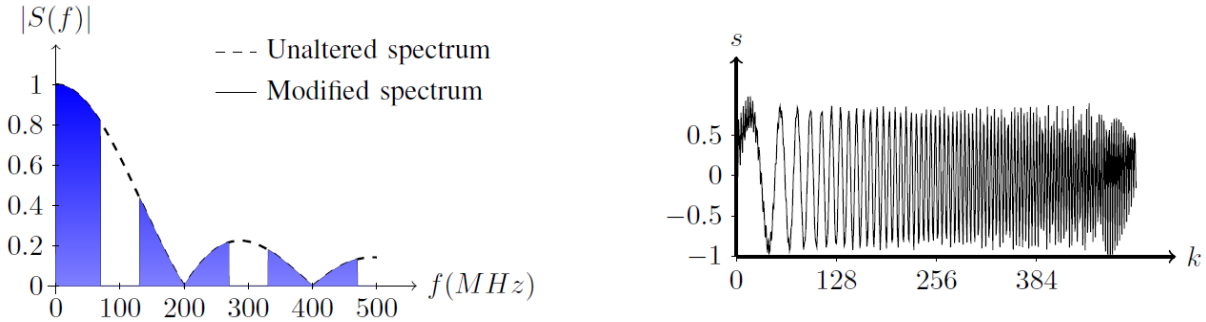

Figure 1.8: An example of MCTDR signal. On the left, the spectrum of multi-carrier signal and on the right, the time domain representation of the signal [44].

the hypothesis that all the coefficients of the injected signal are active ($c_k \neq 0$), a deconvolution algorithm is applied.

On the other hand, when the bandwidth is split into many sub-carriers, for which a set of $c_k = 0$, the CLEAN algorithm [1] makes it possible to obtain an approximation of the reflectogram under assumptions about the shape of the reflectogram. Otherwise, the concept of Orthogonal Frequency Division Multiplexing (OFDM) is used to provide more robust results or quality of the diagnosis. This new reflectometry method is called Orthogonal Multi-tone TDR (OMTDR) [2], which is equivalent to an OFDM communicating system. The bandwidth of the testing signal is modulated, applying a Phase-Shift Keying (PSK) of a different order. Basically, it divides the channel bandwidth into many sub-carriers independently modulated. However, sub-carriers in these methods are precisely orthogonal to one another. Thus, they can overlap without interfering. As a result, OMTDR systems can maximize spectral efficiency without causing adjacent interference against native signals on live wires. To improve the quality of the measurement, in another word, to remove the presence of the lobes around each peak, a post-processing module is needed.

It has been found that the MCTDR and the OMTDR reflectometry based methods perform online diagnosis. Unlike other existing methods, their final result computation is independent of the network topology. Besides, they extend the TDR to embedded systems, but the accuracy or quality of the diagnosis is limited, and obtaining interpretable results requires additional processing. Table 1.2 summarizes the advantages and disadvantages of the aforementioned TDR based methods.

Table 1.2: Summary of TDR based method specificities.

Method	Type of signal	Pros	Cons
Pulse TDR	Step or pulse wave.	- Easy to interpret.	- Needs fast rise and fall time. - applicable for offline diagnosis.
NDR	Uses the signals already present in the wire (noise or high-frequency).	- No interference problems.	- Limitation to a soft defect. - Ambiguity of identification of the peak.
STDR	PN sequences.	- Little interference with the existing signals. - Low amplitude of the PN. - Easy integration.	- No flexibility of the spectrum. - Loss of precision.
MCTDR	Set of sinusoids in the time domain.	- Full control of the spectrum. - No interference. - Robustness to noise. - Adaptation to the complex network.	- Need an averaging. - Need a post-processing.
OMTDR	OFDM based modulation signal.	- Increase of spectral efficiency. - Increased transmission rate. - Possibility for communication. - More accurate for soft defects.	- Need an averaging. - Need a post-processing.

1.4 Embedded diagnosis and hardware requirements

Live wire diagnosis is often required to ensure permanent monitoring of the health of embedded cables. Condition-based maintenance is a modern approach that provides high reliability and low maintenance cost at the same time. This implies integrating an embedded diagnosis system into the native environment of the cable network. Usually, the TDR based method detailed in Section 1.3.2 and Table 1.2 are qualified for online wire diagnosis; therefore, for embedded diagnosis systems. This real-time operating system takes into account the entire measurement chain from generation of the signal up to the location of the fault. It has three main functions; first, the generation of the test signal, second the acquisition of the reflected signal, and third the post-processing module for locating the defect, warning the user, or both. Modern embedded systems use a processor cores together with Field-Programmable Gate Array (FPGA) or Application Specific Integrated Circuit (ASIC). In this context, digital signals or the discrete-time vector of the signal are required. Furthermore, compared to any analog methods for TDR and FDR reflectometry, the operation in the digital domain is easier and manageable such as the generation of MCTDR or any other signals. Figure 1.9 represents a typical embedded wire diagnosis system setup.

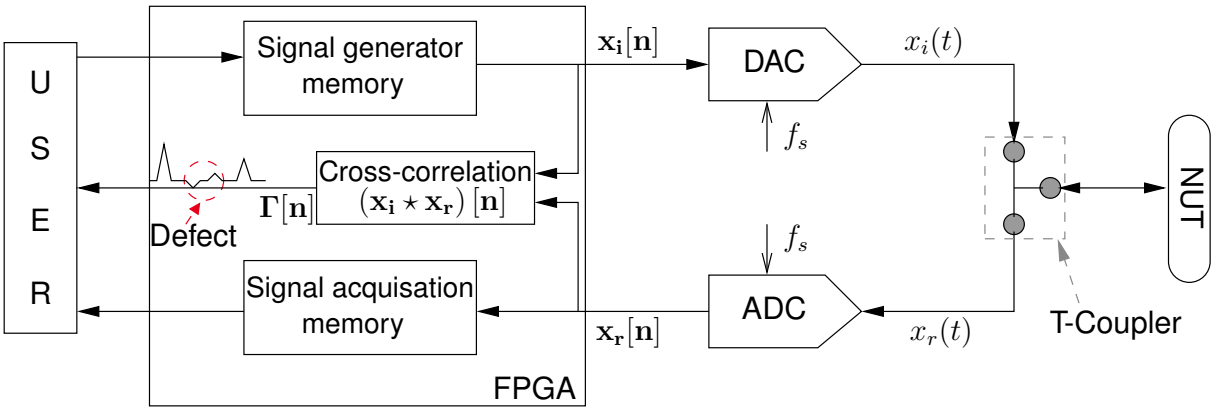

Figure 1.9: Typical embedded wire diagnosis setup. Using a FPGA to generate the injected signal $\mathbf{x_i[n]}$, to save the reflected signal $\mathbf{x_r[n]}$ and finally to apply a cross-correlation. The conversion from digital to analog and vice-versa is applied by DAC and ADC respectively. The sampling frequency, f_s, is defined by Shannon-Nyquist theory.

The concept of this architecture is that an N-length discrete testing signal $\mathbf{x_i[n]}$ is injected periodically:

$$\mathbf{x_i[n]} = (\mathbf{x_{i1}}, \mathbf{x_{i2}}, \cdots, \mathbf{x_{iN}})^{\mathrm{T}}, \tag{1.17}$$

where T denotes the Transpose of the vector $\mathbf{x_i[n]}$.

The DAC transforms the discrete-time signal into analog signal $x_i(t)$. The period of the signal is $T_\mathrm{N} = \mathrm{N}T_s$, where $T_s = \frac{1}{f_s}$ is the sampling period of the DAC. Then, to make the necessary connection, the unavoidable T-coupler is used. Its first end is linked to the DAC of the board, the second end is connected to the NUT, and the third one is connected to the ADC entry of the board. On reception, the time domain of reflected signal $x_r(t)$, which depends on the impulse response $h(t)$ of the network, is expressed as follows:

$$x_r(t) = \sum_{k=-\infty}^{+\infty} \sum_{\mathbf{n}=1}^{\mathrm{N}} \mathbf{x_i[n]} \int_0^{T_s} h(\tau + \mathrm{N}T_s + kT_\mathrm{N}) d\tau. \tag{1.18}$$

Next, the ADC samples the reflected signal $x_r(t)$ with a frequency f_s, similar to the DAC, which should respect the Shannon-Nyquist theory. The sampled vector $\mathbf{x_r[n]}$ is written as follows:

$$\mathbf{x_r[n]} = (\mathbf{x_{r1}}, \mathbf{x_{r2}}, \cdots, \mathbf{x_{r\mathrm{N}}})^\mathrm{T}, \tag{1.19}$$

Finally, in order to obtain the wire transfer function and to check the health condition of the NUT, the similarity is measured in the digital domain between $\mathbf{x_i[n]}$ and $\mathbf{x_r[n]}$. This process is accomplished by a cross-correlation, $\mathbf{\Gamma[n]}$ given in discrete domain by

$$\mathbf{\Gamma[n]} = (\mathbf{x_i} \star \mathbf{x_r})\,[\mathbf{n}] = \sum_{\mathbf{m}=-\infty}^{\infty} \mathbf{x_i^{\#}[m] x_r[m+n]}, \tag{1.20}$$

where $(\star)$ and $(\#)$ denotes the cross-correlation and complex conjugate, respectively. Lelong, in his thesis [1], explains the cross-correlation technique more specifically. The correlation or any other post-processing may be applied directly in the FPGA or by the user (software). Hence, the board can be interfaced with a user or to a personal computer in order to download and analyze the data acquired by the FPGA.

Indeed, the interesting fact about the performances of reflectometry is related to detection and location accuracy. More importantly, though, the spatial resolution and maximal distance to the fault location are responsible for the efficient performance of the reflectometry. These two factors, especially the spatial resolution, have been the subject of several research projects and will be discussed in the following.

- **The maximal distance to the fault:** l_{max}

Depending on the type of the signal Dirac pulse, sinusoidal, or multi-carrier frequency signals, a choice of f_{min} and f_{max} is required. Taking into consideration the MC signals and the assumption of generating the signal in the digital domain, the frequency step

size, Δf, is dependent on the number of points N and the frequency bandwidth [35]. The maximum range of the system, l_{max} at which it can detect a defect is calculated by

$$l_{\text{max}} = \frac{v_p}{2\Delta f}, \qquad \text{where} \qquad \Delta f = \frac{f_{\text{max}} - f_{\text{min}}}{\mathrm{N}}. \tag{1.21}$$

Thus, as given in equation (1.21), Δf limits the l_{max} of the NUT. The factor 2 is related to the fact that since the signal performs a round trip down the wire, so the maximum cable length that can be measured is half the allowable range. To use reflectometry in the analysis of electrical cables, it is necessary to inject signals whose wavelength is smaller or equivalent to the length of the cable, thus implying the use of high-frequency or broadband signals.

●**The spatial resolution:** δ_s

The resolution of measurement determines the accuracy in detection of the fault position in the NUT. Thus, the importance of determining the spatial resolution δ_s. This factor is related to the bandwidth B of the injected signal, according to [28]:

$$\delta_s = \frac{v_g}{B}. \tag{1.22}$$

The spatial resolution is responsible for the accuracy of defect localization. Based on equation (1.22), improving the accuracy of reflectometry systems requires the use of high-frequency signals. The shorter the rise/fall time of the standard TDR, the higher is the resolution. For MC signals (especially for MCTDR, OMTDR, or FDR methods), this resolution is limited by the frequency sweep bandwidth. However, for future reflectometry systems, maximizing the δ_s is a major challenge. Decreasing the pulse width of a Gaussian signal or in general using high-frequency signals implies the need for high-frequency DAC or ADC. One of the fundamental tenets of signal processing that lies at the heart of practically all DAC and ADC devices is the Shannon-Nyquist sampling theory. In the field of data conversion, the number of samples needed to recover a signal correctly is dictated by its bandwidth. It can be explained that, if the band-limited signal occupies a bandwidth of B Hz, this latter be reconstructed without error from uniform samples, if the sampling rate is at least $2B$ samples/sec.

1.4.1 Hardware limitation

Reviewing subsequent and more recent literature, some techniques have been proposed to improve the location accuracy, such as the fake oversampling techniques [45], phase analysis of reflected signal [46], or other frequency domain analysis methods [47]. The most well-known and used is the oversampling technique. It is about increasing the sampling frequency of the measured signal by a factor Ω. The new sampling frequency is $f_s' = \Omega f_s$ and the new sample vector representing the measured signal becomes of length $\Omega \mathrm{N}$. The article [47] explains two alternative methods that use the oversampling technique. The first alternative method of oversampling relies on the incremental phase-offset shifting technique, which samples the received signal at an arbitrarily spaced time. The second is the fake oversampling; this will be applied by using a constant frequency offset between the DAC and ADC, which means that $f_{\text{ADC}} = \frac{\Omega}{\Omega+1} f_{\text{DAC}}$. These techniques are capable of providing more accurate results of fault's location, yet some of them face important synchronization problems, others must determine an interval time to guarantee detection of the defect. Furthermore, the oversampling or high rate ADC samples an enormous amount of information, which may require a greater memory size and in real-time increases the complexity and the cost of the diagnosis system. All of these proposed techniques, based on a different approach, remain using the Nyquist rate. The application of this rate requires a sampling frequency that is almost beyond the limit of the physical capabilities of ADC. Thus, electronically, there is a need for fast microprocessors, fast sampling systems, or fast FPGA in order to analyze the result from the reflected signal.

Today, after six decades of formulation of the Shannon-Nyquist theorem, there are various architectures for ADC design: Delta Sigma, Successive Approximations, Pipeline, Flash. Not only the technology of ADC architecture can no longer reach the required rate, but also they start loosing in resolution and are computationally expensive [5, 48, 49]. Nowadays, the practical implementation of live wire diagnosis have been implemented on an FPGA board driving ADC between $65 - 200\ \mathrm{MHz}$ [43, 47]. In Fig. 1.10, we represent a conceptual approach between the conversion rate (speed) and the resolution for ADC. As we notice, the faster the conversion rate of the ADC, the smaller the converter resolution gets. Waiting around for ADC technology to catch up to new applications could take many years. So the question that arises is if a signal can be sampled at a frequency well below the minimum frequency prescribed by Shannon. Therefore, we are interested in a sub-Nyquist method that permits to use

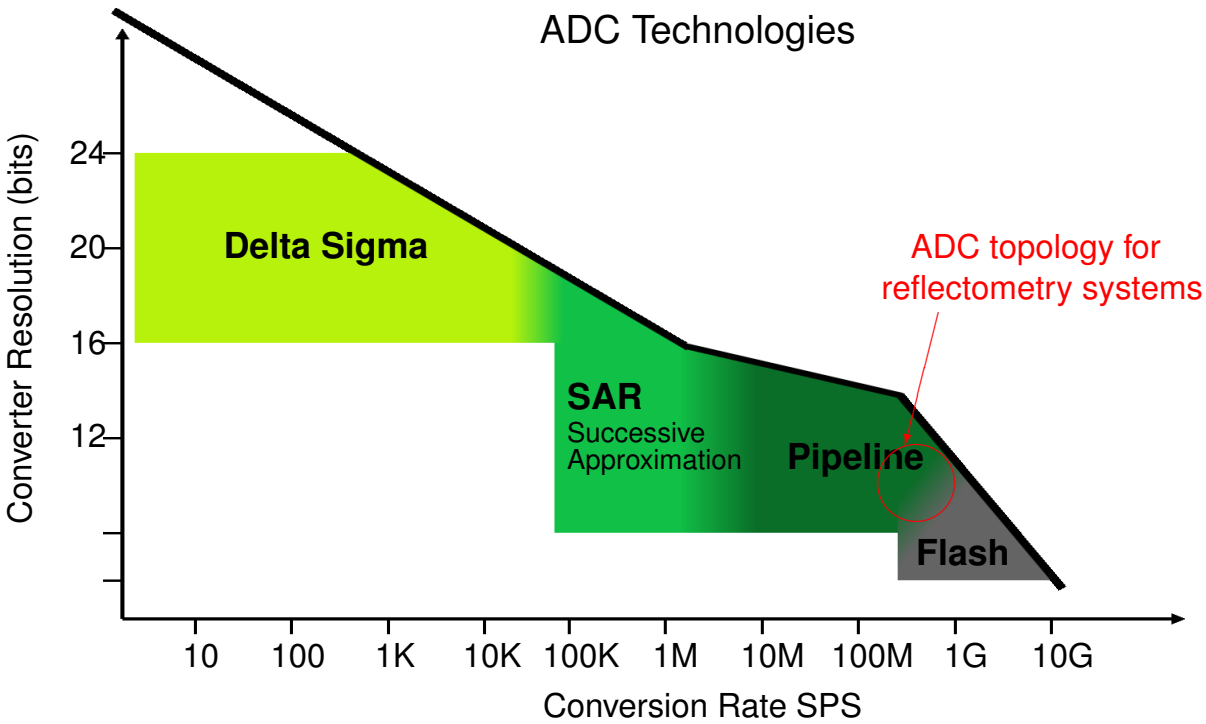

Figure 1.10: A conceptual approach between the conversion rate (speed) and the resolution for Nyquist ADCs architectures.

high-frequency signals and to bypass the minimum rate required for sampling.

1.5 Conclusion

In this chapter, we presented the area of application of the cables and their catastrophic consequences when they are subject to aggressive environmental conditions. Those factors are responsible for the change in the nature of the healthy wire; hence the apparition of some faults. In a bath-tube curve, we represent the instantaneous damage rate versus the time phase of different types of defects. Therefore, a monitoring system is required to gain some time and money. In this context, the reflectometry method appears to be the most suitable for detecting and locating one or more defects in wired networks. Next, a quick overview of wave propagation techniques on the transmission line helps to better understand some specification of reflectometry systems. We focus more on reflectometry based methods. We classify those methods into two prominent families TDR and FDR. We detail each technique separately, and they distinguished

by the types of injected waveforms and the methods used for the analysis of the reflected signal. Also, this chapter indicates the advantages and disadvantages of each proposed method to perform the online diagnosis. An essential aspect of the reflectometry systems is the ability to run online. To provide greater flexibility and fully digital processing, MC reflectometry is proving to be a promising approach. We are interested in embedded diagnosis; therefore, we introduce the architecture setup of the wire diagnosis technique. The fact that high-frequency signals results in an improvement of spatial resolution, hence the fault location accuracy, push us to study the hardware limitation of the embedded diagnosis.

Finally, by taking into account the mentioned specification of such a measurement system, it can be noticed that very high-frequency signal acquisition must deal with fast ADCs, high-speed FPGA circuits, and an enormous amount of data would in compact memory controllers. Therefore, we close this chapter by a state-of-arts, on the actual ADC limitation. In this context, we dedicate Chapter 2 to highlight the possibility to integrate sub-Nyquist sampling techniques.

CHAPTER 2

COMPRESSIVE SAMPLING

2.1 Introduction

As mentioned previously, to avoid spectral aliasing, the well known Shannon-Nyquist sampling theorem tells that the nominal sampling frequency required is at least twice the maximum frequency of the signal. Moreover, the low-pass filter is not sufficient to avoid the aliasing problems. However, in many applications, this frequency limitation has many consequences. For example, in a digital image and video cameras, it can be so high that eventually, too many redundant samples are collected to store or transmit them. In radar [50] and biomedical systems (Wireless Body Sensor Networks [51, 52] or Magnetic Resonance Imaging [53]) where high-speed ADC is needed and that sometimes is beyond the current state-of-the-art; also, in this case, it gets very expensive. Further research is needed to prove the viability of high data-rate with reasonable power consumption ADC (e.g., 20 GHz sampling rate with 16 bits resolution) and to find ways to increase reliability and feasibility of Nyquist sampling systems. Therefore, academia and industry have an interest in the advancement and implementation of sub-Nyquist systems. Accordingly, a partial measurement of the signal is applied using a sampling rate lower than the Nyquist rate. In some way, as shown in Table 2.1, we can classify two categories of sampling: the Nyquist sampling and sub-Nyquist sampling. The algorithm of sub-Nyquist systems is applied by a technique called Compressive Sampling (CS), also called Compressive Sensing. The idea of CS was first introduced in signal processing by Donoho [6] and Candès [7]. The particularity of CS is that it combines the sampling and compression into one step by measuring minimum samples which contain enough information about the signal [54]. In 2004 the idea of CS got a new level, subsequently as seen in diverse fields. In image processing application (especially in cameras, medical imaging, and seismic imaging), it shows a successful achievement by reducing the number of measurements, consequently, the power consumption, the cost, and the complexity of the system [55–58]. Also, compared to

classical radar systems, it improves the resolution that can be limited by time-frequency analysis of the signal [59].

Table 2.1: Summary of pros, cons and challenges of Nyquist and sub-Nyquist sampling.

Type	Nyquist sampling	Sub-Nyquist sampling
Algorithm sub-type	Standard A/D converters	Compressive Sampling
Pros	Simple structure	Low sampling rate, signal acquisition cost
Cons	High sampling rate, energy cost	Sensitive to design imperfection
Challenges	Reduce sampling rate, save energy	Improve robustness

The CS exploits additional information about the digitized signal in question in order to capture it at a frequency below that of the Nyquist rate directly in compressed form and without loss of any information. The rest of this chapter is organized into two parts. First, we provide a state-of-the-art of the key mathematical insights underlying the CS. The second part will focus on the practical side. The data acquisition chain with the CS, called Analog to Information Converter (AIC), will be studied and the various encoders proposed in the literature will be presented.

2.2 Methodology of CS

The theory of CS has existed for around 4 decades [54]. It emerged to a new level in 2004 by David Donoho and Emmanuel Candès [60]. On the contrary to the central tenets of signal processing, the idea of CS relies on sampling a signal at a frequency significantly less than the twice by its bandwidth in a uniform or non-uniform way and by exploiting some characteristic. This leads to shorter acquisition times and decreased amounts of data. Although the pertinence of this paradigm refers to some conditions which are directly related to the type of the signals of interest and the sampling process. Respectively, the validation of this framework is based mainly on tow fundamental premises: **sparsity** and **incoherency**. Once the required conditions are defined, the

final step consists of recovering the sub-sampled signal via sparse reconstruction algorithms. Indeed, we can summarize that the applicability of the CS paradigm suggests very particular acquisition and recovery protocol, as illustrated in Figure 2.1.

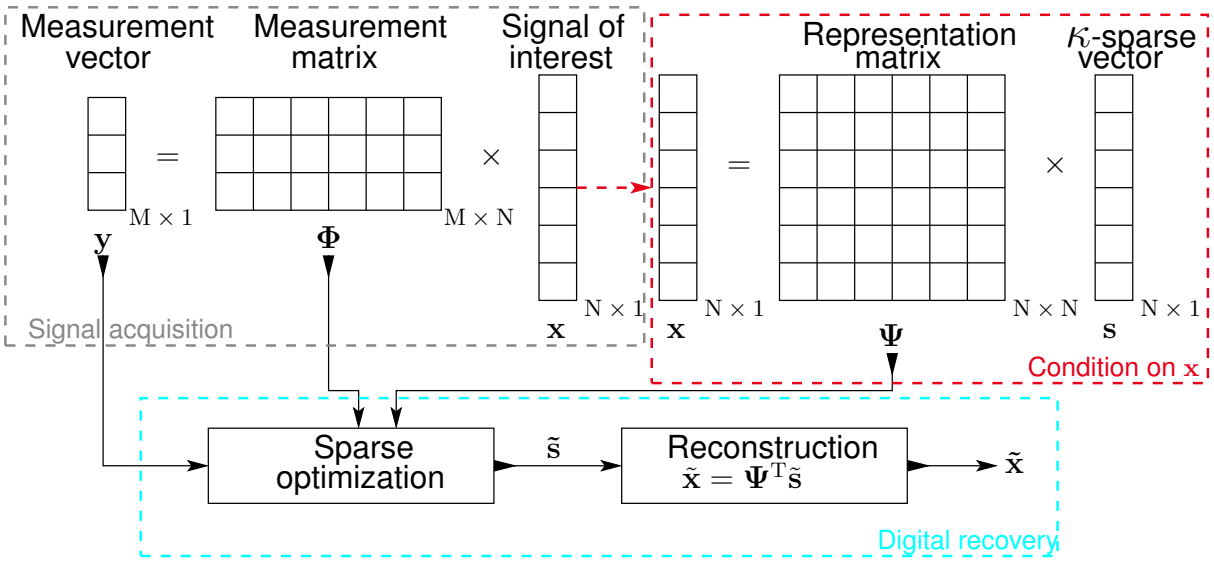

Figure 2.1: Conceptual illustration of the CS theorem. It contains three different phases: condition on $\mathbf{x}$ phase, signal acquisition phase, and the digital recovery phase. Note that (T) is the transpose operation.

2.2.1 Sparsity

The sparsity of the signal is at the forefront of the CS theory. A vector is sparse if it can have a few non-zero coefficients compared to its length. Thus, exploiting the fact that natural signals such as sound, Gaussian, or Electrocardiograms have a sparse representation in time-domain; accordingly, it can be stored only a small number of coefficients rather than all the signal samples. For instance, suppose that a finite-dimensional $\mathrm{N} \times 1$ column vector of discrete-time signal $\mathbf{x}$ in $\in \mathbb{R}^{\mathrm{N}}$, is stated as sparse if its pseudo norm ℓ_0[1] is equal to $\mathcal{K}$ where $\mathcal{K} \ll \mathrm{N}$. In other words, $||\mathbf{x}||_0 = \mathcal{K}$. However, any signal $\mathbf{x}$ in $\in \mathbb{R}^{\mathrm{N}}$ that is not sparse in its time domain basis can be sparse in another specific basis, which is called dictionary. Thus, $\mathbf{x}$ is represented as follow:

$$\mathbf{x} = \mathbf{\Psi}\mathbf{s}, \tag{2.1}$$

[1]The pseudo norm ℓ_0 of a vector is defined as: $||\mathbf{x}||_0 = \#\{\mathrm{i} : \mathbf{x}_\mathrm{i} \neq 0\}$, which calculates the total number of non-zero elements in a vector.

where $\mathbf{\Psi}$ is the $\mathrm{N} \times \mathrm{N}$ dictionary matrix and s, the $\mathrm{N} \times 1$ vector, is the sparse coefficient of x in matrix $\mathbf{\Psi}$. Hence, the $\mathcal{K}$-sparse signal means that only $\mathcal{K}$ coefficients in s are non-zero, and the rest $(\mathrm{N} - \mathcal{K})$ are zero or small enough to be ignored. Clearly, x and s are equivalent representations of the same signal, with x in the time domain and s in the $\mathbf{\Psi}$ domain. Moreover, the degree of sparseness ρ given by:

$$\rho = \frac{\mathcal{K}}{\mathrm{N}}, \tag{2.2}$$

It defines the minimum number of samples required to reconstruct the signal correctly. This implies, the more ρ is small, or equivalently, the more the signal has a sparse representation, the fewer samples are needed; thereby, the sampling frequency is decreased.

Depending on the type of the signal to represent, several compression dictionaries can be used. It exists some standard compressive-type dictionary that has been published in the literature. Images (JPEG and JPEG2000) tend to be compressible in the wavelet bases and Discrete Cosine Transform (DCT) [61, 62]. In many radar applications, the testing signals and the target response are often sparse in time domain since often only a few targets will be present at any given time. Thus, the sparse dictionary Ψ is its canonical basis, $\mathbf{\Psi} = \mathrm{I}_{\mathrm{N}}$, and $\mathrm{x} = \mathrm{s}$ [50, 63]. Furthermore, wide-band signals are not sparse in the time domain. In the case of audio signals and many communication signals when a low spectrum is utilized, then the best compatible sparse representation matrix is in the frequency domain. Thus, the sparsity basis is its Fourier matrix. However, with the increment of the spectrum utilization of the wide-band signal, the frequency domain may no longer be its sparse representation dictionary. Thus, Chapter 3 is devoted to the choices of dictionaries to overcome this challenge.

2.2.2 Acquisition phase

CS replaces the conventional data acquisition approach into a linear and compressed measurement. Throughout the acquisition or measurement phase, the signal is directly sampled without sampling the N data. Before considering the CS case, it is essential to clarify the data acquisition process with respect to the Nyquist rate, which determines the sampling frequency f_s of ADC. Taking into account the requirement of N samples, the linear measurement process is represented by an inner product between x and a collection of vectors $\{\mathbf{\Phi}_n\}_{n=1}^{\mathrm{N}}$. Which gives, as a result, a measurement $\mathbf{y}_n = \langle \mathbf{\Phi}_n, \mathrm{x} \rangle$.

Hence, we can deduce:

$$\mathbf{y} = \mathbf{\Phi x}, \tag{2.3}$$

where $\mathbf{y}$ is an $\mathrm{N} \times 1$ observation vector and $\mathbf{\Phi}$ is the $\mathrm{N} \times \mathrm{N}$ measurement matrix. While in CS, since f_s is much smaller than the Nyquist rate, therefore only M values are sampled and $\mathrm{M} < \mathrm{N}$. In this case, the observation $\mathbf{y}$ is an $\mathrm{M} \times 1$ vector and $\mathbf{\Phi}$ an $\mathrm{M} \times \mathrm{N}$ matrix. Together with the sparse dictionary matrix $\mathbf{\Psi}$, the equation (2.3) develop into:

$$\mathbf{y} = \mathbf{\Theta s}, \qquad \text{where} \qquad \mathbf{\Theta} = \mathbf{\Phi \Psi}, \tag{2.4}$$

where $\mathbf{\Theta}$ is the $\mathrm{M} \times \mathrm{N}$ reconstruction matrix, s is the transform of $\mathbf{x}$ in the domain $\mathbf{\Psi}$, with $||\mathrm{s}||_0 = \mathcal{K}$ and $\mathcal{K} < \mathrm{M} < N$. However, to recover exactly the vector $\mathbf{x}$ of length N from the undersampled measurements $\mathbf{y}$, some criteria should be taken into consideration.

2.2.2.1 Properties

The following paragraphs will present the criteria commonly used in the literature for the measurement matrix. Said differently, the sensing matrix must obey certain conditions to guarantee that the acquisition phase of the CS will not modify the data in the compressed signal.

●Incoherency

The incoherency/coherency is applied between two matrices. Based on the mathematical explanation, the coherence measures the maximum correlation between any two elements of two different matrices. In CS, the coherence (μ) is calculated between the $\mathrm{N} \times \mathrm{N}$ sparseness matrix $\mathbf{\Psi}$ with $\psi_1, \cdots, \psi_\mathrm{N}$ as columns and the $\mathrm{M} \times \mathrm{N}$ measurement matrix $\mathbf{\Phi}$ with $\phi_1, \cdots, \phi_\mathrm{N}$ as rows. It is defined as:

$$\mu(\mathbf{\Phi}, \mathbf{\Psi}) = \sqrt{\mathrm{N}} \max_{\substack{1 \leq m \leq \mathrm{M} \\ 1 \leq n \leq \mathrm{N}}} |\phi_m, \psi_n|. \tag{2.5}$$

The CS framework is interested in low coherence (incoherence) between them. Moreover, the lower the coherence is, the less data is required for the reconstruction of the signal; thereby, the sampling frequency is decreased. Note that, the maximum incoherency is equal to 1, because as a deduction from linear algebra $\mu(\mathbf{\Phi}, \mathbf{\Psi}) \in [1, \sqrt{\mathrm{N}}]$ [64].

●Restricted Isometry Property (RIP)

Concerning the incoherency, an alternative approach for the robustness and the stability of the CS is to check the RIP of the reconstruction matrix $\mathbf{\Theta}$. It will permit to evaluate the CS recovery algorithms. The idea of RIP is applied to ensure that the measurement matrix preserves the important information for the testing signal [65]. For any $\mathcal{K}$-sparse vector $\mathbf{x}$, the RIP states that:

$$1 - \epsilon \leq \frac{||\mathbf{\Theta x}||_2}{||\mathbf{x}||_2} \leq 1 + \epsilon, \tag{2.6}$$

where $\epsilon \in]0, 1[$ is the restricted isometry constant. This means that if the measurement matrix $\mathbf{\Theta}$ satisfies the RIP, then it implies for two measurement vectors $\mathbf{y}_1 = \mathbf{\Theta s}_1$ and $\mathbf{y}_2 = \mathbf{\Theta s}_2$, that $\mathcal{K}$-sparse vectors $\mathbf{s}_1$ and $\mathbf{s}_2$ in $\mathbb{R}^{\mathrm{N}}$ will not map to the same vector in $\mathbb{R}^{\mathrm{n}}$ and their distance is approximately preserved. The RIP is a valuable property that guarantees the reconstruction of the signal. However, it is difficult to verify whether a matrix satisfies the RIP, in practice, it is replaced by coherence. Moreover, the equation (2.7) shows a relation between the RIP and coherency. It implies that when a matrix has a low coherence, it satisfies the RIP [66].

$$\epsilon \leq (\mathcal{K} - 1)\mu(\mathbf{\Phi}, \mathbf{\Psi}). \tag{2.7}$$

Indeed, after determining the sparsity matrix $\mathbf{\Psi}$ and in order to succeed a proper reconstruction (verifying the RIP), according to the state-of-the-art, $\mathbf{\Phi}$ must be a random matrix. Mainly, when the elements of the measurement matrix $\mathbf{\Phi}$ are generated from an identical and independently distributed Gaussian law. Admitting the fact that random matrices have excellent statistical properties [67], much consideration has focused on designing CS systems using random entries measurement matrices.

2.2.3 Recovery phase

The final phase of the CS is the recovery phase. The original signal is constructed from the sub-sampled vector $\mathbf{y}$, the measurement matrix $\mathbf{\Phi}$, and the sparse representation domain $\mathbf{\Psi}$. Successively, to recover from the compressed measurement the original signal or equivalently its sparse coefficient vector $\mathbf{s}$ some reconstruction algorithms are proposed [54]. Those algorithms solve the equation (2.4) based on minimization techniques. They use either ℓ_0, ℓ_1, or ℓ_2 norms by taking advantage of the fact that the

solution is sparse. The prior sparse condition about the signal directly drives to use the ℓ_0-norm. Unfortunately, solving ℓ_0-norm in the constraint is a nonconvex and NP-hard problem. The ℓ_2-norm, least-squares minimization, will almost never find the κ-sparse solution; instead, it will result in a non-sparse solution [68, 69]. In the CS literature, ℓ_1-norm minimization is frequently used.

Minimum ℓ_1-norm reconstruction, is a convex optimization problem. Considering the noise-free measurement, equation (2.4), the optimization problem is

$$\tilde{\mathbf{s}} = \underset{\mathbf{s}'}{\operatorname{argmin}} ||\mathbf{s}'||_1, \qquad \text{such that} \qquad \mathbf{\Theta s}' = \mathbf{y}. \tag{2.8}$$

Once the algorithm successfully converges to an estimate s', the signal of interest can be easily obtained as $\mathbf{x}' = \mathbf{\Psi s}'$. To find the sparsest solution in CS, the reconstruction algorithms are divided into several groups. The most popular ones are *Convex Relaxation* and *Greedy* algorithms [54, 68, 69]. Even though *Convex Relaxation* algorithms, like *Basis Pursuit*, provide a successful recovery, it suffers from high implementation complexity because it solves a convex optimization problem through linear programming.

For this reason, *Greedy* algorithms were developed, and rely on iterative approximation. In general, they compute one iteration at a time by adding to the sparse solution a new atom and provide the least approximation error. *Matching Pursuit* is the simplest version of *Greedy* algorithms, but the disadvantage of this method is that a column of the measurement matrix can be selected several times during the selection phase. To circumvent this issue and to improve convergence, among all the Greedy algorithms, the *Orthogonal Matching Pursuit* (OMP) has shown an absolute success, especially in efficiency versus computational load [70]. A more detailed survey about the variety of algorithms can be found in [54, 69]. Throughout this thesis, we are interested in OMP, the description of this optimization method is illustrated in Algorithm 1 where $\mathbf{\Theta}^\dagger$ is the Moore-Penrose pseudoinverse of $\mathbf{\Theta}$. Furthermore, it was demonstrated in [71] that $\tilde{\mathrm{s}}$ is reconstructed entirely with a very high probability if the number of measurements M verifies the condition $\mathrm{M} \geq C\mu^2(\mathbf{\Phi}, \mathbf{\Psi})\kappa \log \mathrm{N}$ and C is an arbitrary positive constant. In the literature, there exist other types of reconstruction algorithms.

Algorithm 1 *Orthogonal Matching Pursuit* (OMP) Algorithm

Input: Signal $\mathbf{y} \in \mathbb{R}^{\mathrm{M}}$ and matrix $\mathbf{\Theta} \in \mathbb{R}^{\mathrm{M}\times\mathrm{N}}$
Output: estimated sparse vector $\tilde{\mathbf{s}} \in \mathbb{R}^{\mathrm{M}}$
1: Set the initial solution $\tilde{\mathbf{s}}_0 = 0$
2: Set the initial residual $\mathbf{r}_0 = \mathbf{y} - \mathbf{\Theta}\tilde{\mathbf{s}}_0 = \mathbf{y}$
3: Set the initial support $\mathbf{S}_0 = \emptyset$
4: **Repeat** for $j = 1$; $j := j + 1$ till stopping criterion is met
5: Select index i_{max} so that $\underset{i}{\operatorname{argmax}} |\Theta_i^{\mathrm{T}} r_{j-1}|$ for all $i \notin \mathbf{S}_{j-1}$
6: Update $\mathbf{S}_j = \mathbf{S}_{j-1} \cup i_{max}$
7: Update $\tilde{\mathbf{s}}_{\mathbf{S}_j} = \mathbf{\Theta}_{\mathbf{S}_j}^{\dagger}\mathbf{y}$ where $\mathbf{\Theta}_{\mathbf{S}_j}^{\dagger} = \left(\mathbf{\Theta}_{\mathbf{S}_j}^{\mathrm{T}}\mathbf{\Theta}_{\mathbf{S}_j}\right)^{-1}\mathbf{\Theta}_{\mathbf{S}_j}^{\mathrm{T}}$
8: Update $\mathbf{r}_j = \mathbf{y} - \mathbf{\Theta}_{\mathbf{S}_j}\tilde{\mathbf{s}}_{\mathbf{S}_j}$
9: **Return** $\tilde{\mathbf{s}}$

2.2.4 Performance metrics

To evaluate the quality of the reconstructed signal, we employ the performance metrics: Percentage Root-mean-square Difference (PRD) and Signal to Noise Ratio (SNR). The PRD and SNR evaluate the error between the original signal $\mathbf{x}$ and the reconstructed signal $\tilde{\mathbf{x}}$. In [72], a study on electrocardiogram signals classifies the quality of the reconstructed signal based on the value of the PRD. For example, if some signal has a PRD between $0 \sim 2\ \%$, it belongs to the "very good" quality group, and for a PRD above $9\ \%$ it is hard to determine its quality group. Table 2.2 summarizes the different quality groups of the reconstructed signal as a function of the PRD.

$$\text{PRD}_{[\%]} = \frac{||\mathbf{x} - \tilde{\mathbf{x}}||_2}{||\mathbf{x}||_2} \times 100, \tag{2.9}$$

$$\text{SNR}_{[\text{dB}]} = 20\log_{10}\frac{||\mathbf{x}||_2}{||\mathbf{x} - \tilde{\mathbf{x}}||_2} = -20\log_{10}(0.01 \times \text{PRD}). \tag{2.10}$$

Moreover, the Compression Ratio (CR) and the Compression Factor (CF) are other metrics mostly used in the evaluation for the performances of the CS. The CF is the ratio between the numbers of rows and columns of the measurement matrix $\Phi \in \mathbb{R}^{\mathrm{M}\times\mathrm{N}}$. The CR, as expressed in the equation (2.11), is characterized as the percentage of the length required to represent the signal after compression (M) relative to the length of the original signal (N).

$$\text{CR}_{[\%]} = \frac{\mathrm{N} - \mathrm{M}}{\mathrm{N}} \times 100, \tag{2.11}$$

Table 2.2: Different quality classes of reconstruction according to the PRD [72].

$\text{PRD}_{[\%]}$ (prediction range)	Reconstructed signal quality
$0 \sim 2$	"Very good"
$2 \sim 9$	"Good"
$9 \sim 19$	"Not good"
$19 \sim 60$	"Bad"

$$\text{CF} = \frac{\text{N}}{\text{M}}. \tag{2.12}$$

2.3 Analog measurement matrix

In the context of CS, sensing and processing information linearly of an analog signal at a rate dramatically lower than Nyquist provides several signal acquisition systems. In the data acquisition chain, an analog encoder is placed before the ADC. Indeed, the encoder performs a pre-processing of the analog signal so the ADC can digitize the signal below the Nyquist rate. This combination between the analog encoder and the low rate ADC is defined as Analog-to-Information Converter (AIC). Nevertheless, as represented in Figure 2.2, to sample by means of CS, the data acquisition chain is composed of hardware and software parts. Respectively the first part is the analog front-end, which is followed by the digital back-end. In the first part, the physical data converter is placed. It recalls the CS context (e.g., random property) and defines the measurement matrix Φ. In the second part, sparse reconstruction algorithms are used to reconstruct the signal.

Obviously, the AIC directly retrieves the useful information of the signal. Moreover, as aforementioned, the number of data that the AIC must sample depends on the amount of information contained in the signal. The sparser or more compressible the signal is, the fewer samples AIC needs.

So far, in the literature, there have been proposed at least eight AIC architectures, such as the Non-Uniform Sampling (NUS) [73], Random Demodulator (RD) [74–76], the Modulated-Wideband Converter (MWC) [77], and others [78–82].

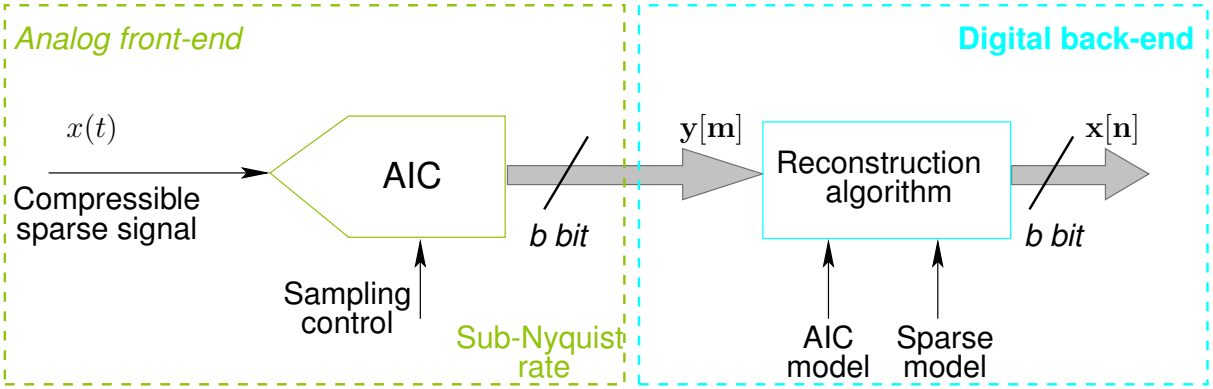

Figure 2.2: A generic overview of sampling by means of CS.

2.3.1 Non-Uniform Sampling (NUS)

The NUS AIC-based architecture uses a sample-and-hold which is followed by a sub-Nyquist rate ADC. For instance, assume the traditional acquisition chain where the analog signal is sampled uniformly with a Nyquist rate ADC at a frequency f_s. In another word, it digitized an analog signal in a time window $\mathrm{T} = \mathrm{N}\Delta\mathrm{t}$ where the time interval between two consecutive samples n and $\mathrm{n}+1$ is $\Delta t = \frac{1}{f_s}$ and N is the Nyquist samples. Theoretically, the measurement matrix $\mathbf{\Phi}$ of this operation is the identity matrix $\mathrm{I_N} \in \mathbb{R}^{\mathrm{N}\times\mathrm{N}}$ and, therefore, the digitized signal $\mathbf{x}[\mathbf{n}] \in \mathbb{R}^{\mathrm{N}}$.

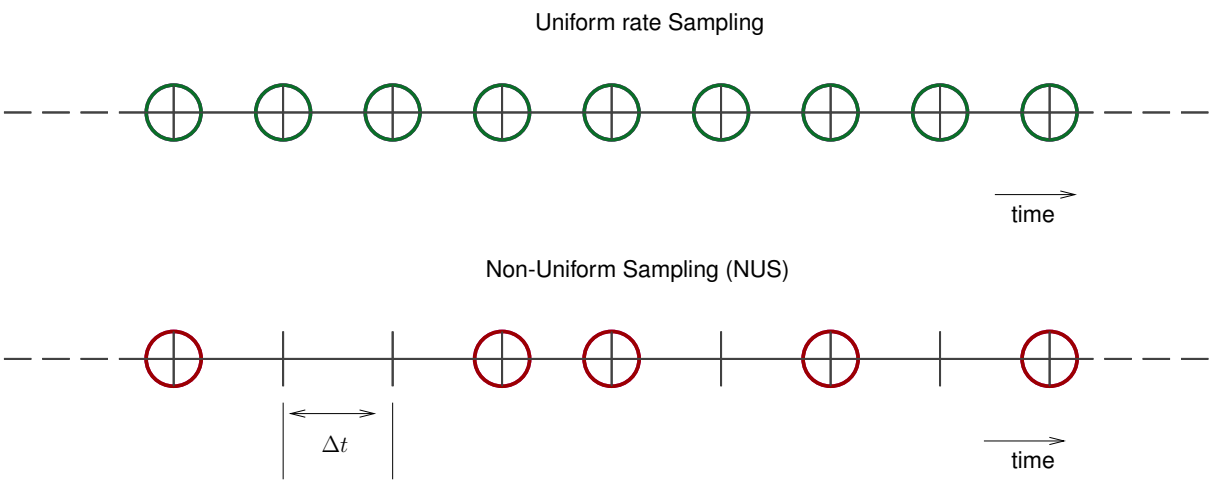

Figure 2.3: NUS protocol. The large circles represent time-domain samples. The NUS samples at irregularly spaced intervals, though always in multiples of Δt.

Alternatively, the NUS avoids using high-rate Nyquist ADC by non-uniformly collecting the data and ignoring the rest. The protocol NUS compared to a Nyquist-rate

sampling is presented in Figure 2.3. The non-uniform sampling digitized the analog signal at irregular intervals of time. Before the low rate ADC, a Pseudo-Random Binary Sequence (PRBS) controls the sample-and-hold circuit. Conceptually, it collects randomly only M samples among the N, with $\mathrm{M} < \mathrm{N}$. In this case the measurement matrix $\Phi \in \mathbb{R}^{\mathrm{M}\times\mathrm{N}}$ is formed by randomly choosing M lines of the identity matrix I. The complication of this method relies on hardware implementation that imposes restrictions on the fact that the measurement matrix should be completely random so that the coherency is surely small. Moreover, frequently the NUS might sample two consecutive data spaced by only Δt apart, so it still requires to sample at f_s. Therefore, the only difference between the Nyquist rate ADC is the number of samples ($\mathrm{M} < \mathrm{N}$).

2.3.2 Random Demodulator (RD)

The RD system is originally designed to capture signals with sparse representation in the frequency domain; see Figure 2.4 for a block diagram. The RD is a linear architecture proposed in [83] in 2006, and it works as follows. The analog signal is multiplied with a PRBS, taking values ± 1 having a bit rate higher than Nyquist, $f_{\mathsf{p}} \geqslant 2f_{\mathsf{max}}$. Since PRBS occupies a large bandwidth, it spreads randomly the spectrum of each active frequency component of the testing analog signal, such that those components are moved throughout the Nyquist zones (especially high frequencies are moved to the low-frequency band). The objective of the demodulation phase is to not damaged the signal by the next stages of the chain. A low pass filter with an impulse response $h(t)$ and a low rate ADC samples the resulting baseband signal where all the necessary information is assembled.

Concisely, the RD is typically decomposed into three steps: demodulation, filtering, and uniform sampling. Those three factors specify the measurement matrix $\mathbf{\Phi}$. The mathematical model of the $\mathbf{\Phi}$ can be modeled as follows:

$$\mathbf{\Phi} = \mathbf{HP}, \tag{2.13}$$

where $\mathbf{H}$, a Toeplitz matrix, represents the impulse response of the low-pass filter as well as the low sampling and $\mathbf{P}$ the PRBS.

The PRBS $p_c(t)$ modulates the signal using a binary sequence with values ± 1:

$$p_c(t) = \mathbf{p}_n, \quad t \in \left[\frac{n}{\mathrm{N}}; \frac{n+1}{\mathrm{N}}\right[\quad \forall\, n \in \{0 \ldots \mathrm{N}-1\}. \tag{2.14}$$

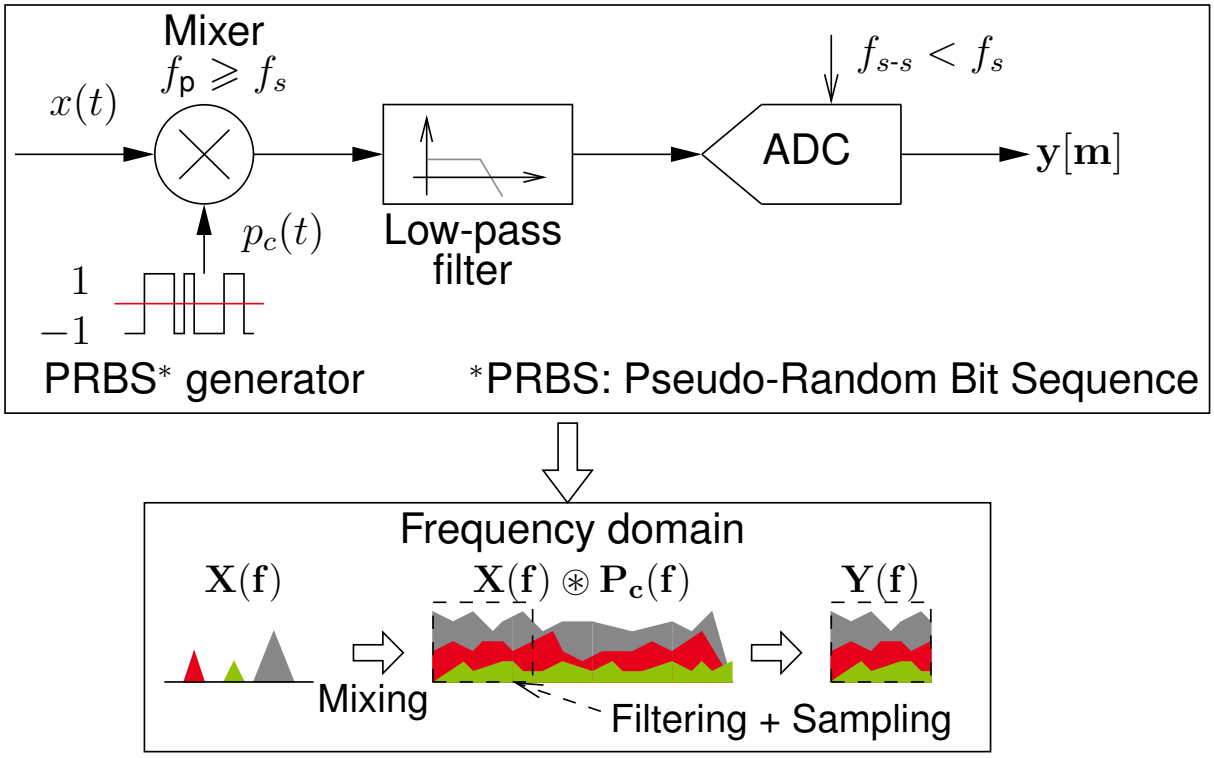

Figure 2.4: The block diagram of the Random Demodulator (RD) on the top, including the three main steps: modulation with $p_c(t)$ with a frequency $f_p \geqslant 2f_{max}$, filtering and low-rate uniform low-rate sampling with an ADC converter at a frequency $f_{s\text{-}s} < f_s$. On the bottom the frequency representation of each steps. Not that $\mathrm{m} \in \{1 \ldots \mathrm{M}\}$.

Therefore, in the discrete-time domain, the modulation yields $\mathbf{d} = \mathbf{P}\mathbf{x}$ such that $\mathbf{P} \in \mathbb{R}^{\mathrm{N}\times\mathrm{N}}$ is a diagonal matrix and $p_n = \pm 1$:

$$\mathbf{P} = \begin{pmatrix} \mathbf{p}_0 & & \\ & \ddots & \\ & & \mathbf{p}_{\mathrm{N}-1} \end{pmatrix}. \tag{2.15}$$

The anti-aliasing low-pass filter structure depends on the discretized impulse response of the filter and the sampling process. Therefore, each row of the matrix $\mathbf{H} \in \mathbb{R}^{\mathrm{M}\times\mathrm{N}}$ outlines the filtering and sampling.

$$\mathbf{H} = \begin{pmatrix} [\mathbf{h}_0 \cdots \mathbf{h}_{\frac{\mathrm{N}}{\mathrm{M}}}]_1 & & \\ & \ddots & \\ & & [\mathbf{h}_0 \cdots \mathbf{h}_{\frac{\mathrm{N}}{\mathrm{M}}}]_{\mathrm{M}} \end{pmatrix}, \tag{2.16}$$

where $\mathbf{h} = [\mathbf{h}_0 \cdots \mathbf{h}_{\frac{\mathrm{N}}{\mathrm{M}}}]$ is a fixed size vector corresponding to the filter coefficients. Ac-

cordingly, the corresponding measurement matrix for RD, $\mathbf{\Phi} \in \mathbb{R}^{\mathrm{M}\times\mathrm{N}}$ has a diagonal block structure, where each block is a fixed size vector equal to $\frac{\mathrm{N}}{\mathrm{M}}$. If the impulse response of the $h(t)$ is equal to 1, the $\mathbf{\Phi}$ elements are formed from the pseudo-random sequence:

$$\mathbf{\Phi} = \begin{pmatrix} [+1\cdots-1]_1 & & & \\ & [-1\cdots+1]_2 & & \\ & & \ddots & \\ & & & [-1\cdots-1]_{\mathrm{M}} \end{pmatrix}. \tag{2.17}$$

2.3.3 Modulated Wideband Converter (MWC)

The architecture of MWC is illustrated in Figure 2.5. A K frequency wide-band signal $x(t)$ enters m channels simultaneously. Every i_{th} channel is similar to RD architecture; the only difference relies on the periodicity of PRBS. Therefore, the signal $x(t)$ is multiplied by a unique periodic PRBS $p_i(t)$ with a period $T_p = \frac{1}{f_p}$ that alternates between ± 1 for each of M equal time intervals. Then it is filtered by the low-pass filter $h(t)$ with cutoff frequency $\frac{1}{2T_{s\text{-}s}}$. Finally, the output signal is sampled at a rate of $f_{s\text{-}s} = \frac{1}{T_{s\text{-}s}}$.

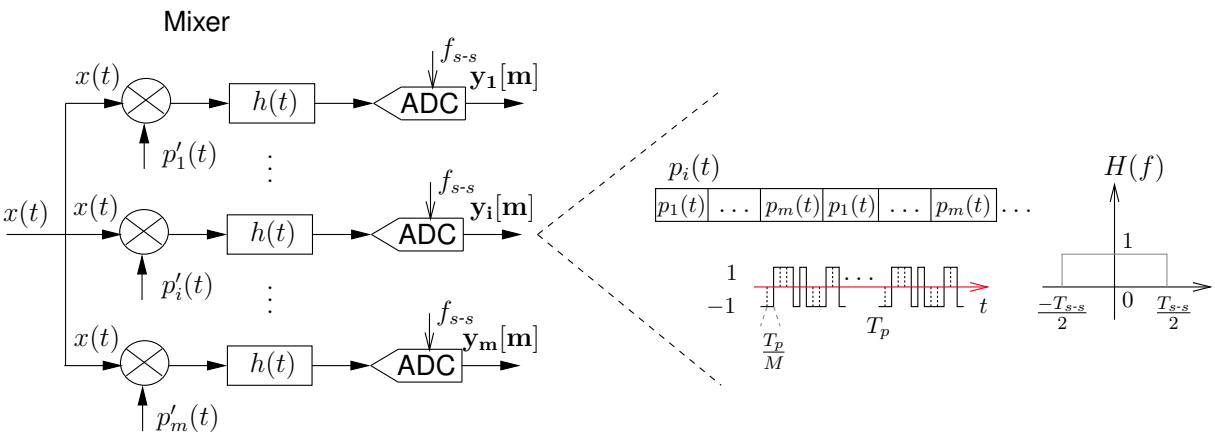

Figure 2.5: The diagram of MWC.

Actually, since the $p_i(t)$ is periodic, it has a Fourier expression

$$p_i(t) = \sum_{l=-\infty}^{\infty} c_{il} \exp\left(j\frac{2\pi}{T_p}lt\right), \tag{2.18}$$

where c_{il} is the Fourier coefficient. This guarantee with a traditional low rate ADC, the signal aliases to the same fold points. Moreover, the randomness of the $p_i(t)$ within

one period of each sequence ensures that there is diversity in the amplitude of each aliased spectrum.

2.3.4 Summary on analog encoder AIC

Table 2.3 summarizes the three different AIC explained previously. It recaps the measurement matrix Φ that the encoder implements, the advantages, the disadvantages, and the field of application of each encoder. Even though MWC and RD almost have similar block diagrams, their reconstruction algorithms and signal models are strongly different. The RD is a single channel uniform sub-sampling design for acquiring multitone signals, whereas the MWC is a multi-channel uniform sub-sampling design for acquiring multiband signals. Actually, they both have a linear architecture, including a (PRBS); thus, the measurement-based matrix Φ has the random property which is adapted for RIP. Furthermore, the RD is robust against noise and quantization errors and is suitable for signals having a finite set of a pure sinus [84]. Considering these advantages and since the reflectometry signals is a multitone sinus type signals; therefore, in this thesis, we are interested in RD architecture. Its extension to other analog encoder, such as MWC, can easily be realized.

Table 2.3: Summary of the various AIC encoders proposed based-CS architectures [84, 85].

	NUS	RD	MWC
Measurement matrix: Φ	Matrix constructed by randomly selecting M rows of an $\mathrm{N} \times \mathrm{N}$ identity matrix I, with $\mathrm{M} < \mathrm{N}$.	Diagonal matrix by block equal to $\frac{\mathrm{N}}{\mathrm{M}}$. Each block forming the diagonal is a vector randomly taking values ± 1 and the impulse response of the filter.	Every channel will determine a diagonal matrix taking values ± 1 and the impulse response of the filter.
Advantages	- Less measurements. - Smaller sampling complexity.	- No need for a high-rate ADC. - Signal sparsity is reconstructed using partial measurements. - Robust against noise and quantization errors.	- Suitable for analog multiband signals. - Flexible control of sampling rate at each channel. - Fast reconstruction process and low sampling delay. - Robust against the noise and model mismatches.
Disadvantages	- Hardware limitations due to restriction of capacity sampling completely randomly. - Must determine the nonuniform probabilities. - Difficult to visualize the output, it depends on the spacing of the samples.	- Slow reconstruction process and high sampling delay. - Affected by design imperfection. - Only suitable for signals having a finite set of pure sinus.	- Requires ideal low pass filters for reconstruction. - Requires many sampling channels and therefore large number of low pass filters. - Imperfections of non-ideal low pass filters. - Limited number of bands and bandwidth.
Application	Image.	Amplitude modulated signals (multitone signal).	Radio frequency transmission (multiband signal).

2.4 Conclusion

This chapter recalls a new theorem, called CS, that changes the central tenets of digital signal processing, which relies on Shannon-Nyquist sampling. It confirms that a signal having a sparse representation in a specific domain can be sampled linearly at a rate proportional to their sparsity, which is completely smaller than their Nyquist rate. For this reason, we first explain the importance of sparse signal and some other hypothesis that the acquisition phase of the signal should satisfy, such as coherency and the RIP. We then detail the importance of the recovery phase that relies on using some sparse optimization algorithms. We finally presented the different implementations of existing analog encoders, AICs, that aim at implementing sub-Nyquist signal acquisition systems. The AICs are proposed for analog signals that recall the CS context and define the measurement matrix Φ. In general, the idea of AIC is to spread the high-frequency components and fold back to low frequencies that can be acquired by a low rate ADC.

Indeed, CS is an alternative solution and has already shown a notable success on several applications (e.g., Radars, Magnetic resonance imaging, $\cdots$), but it has multiple difficult conditions to take in consideration:

- Is any analog encoder simple to implement, which defines the measurement matrix and will be used during the measurement phase? First, random sampling was introduced that had a limitation on hardware implementation. To facilitate this condition, RD was implemented for multitone signals. Since the reflectometry signals are multitone sinus type, thus this architecture is the most adapted for our study.

- How to adequately reconstruct the original signal with a few samples? Many algorithms were proposed in the literature. Due to the disadvantages of NP-hard problem and unsatisfactory results with non-sparse signals of ℓ_0 and ℓ_2 respectively, those algorithms use ℓ_1 norm optimization. Therefore we detail the OMP, an iterative algorithm, that shows an absolute success as low complexity and efficient reconstruction algorithm.

- Which condition must the signal satisfy? The sparsity degree of the signal or the search for a domain or a base allowing a very low degree of sparseness is the most important. Indeed, the more the signal is sparse, the fewer samples are needed to rebuild the signal correctly. Generally, Wavelet, Discrete Cosine, or the Fourier transform domains are the most used. By keeping this in mind and the

fact that reflectometry signals are complex and MC signal, the determination of the sparse representation basis is essential. The definition of those matrices will be the subject of our next chapter.

CHAPTER 3

SPARSE DICTIONARY FOR REFLECTOMETRY SIGNALS

3.1 Introduction

In section 2.2.1,we mentioned the importance of the sparsity. It leads to a decisive compression factor as it should also be noted its relation to the recovery process. As stated in [54], the recovery by sparse optimization algorithms directly depends on the sparsity of the signal that we aim to estimate.

Sparseness dictionaries appear in a variety of settings [64]. Although, many natural signals are sparse in their time domain; therefore, the most common dictionary may be their unique canonical basis. The fact that among all the reflectometry signals, the Pulse TDR is the only one considered sparse in his canonical basis; thus, the objective of this chapter is to introduce the dictionaries where each signal x has a unique set of expansion coefficient $\mathrm{s} = \mathbf{\Psi}^{-1}\mathbf{x}$. For this reason, finding a new dictionary is necessary so that a few non-zero coefficients can represent a signal. Beyond the simplistic sparse model, we will consider two different kinds of reflectometry signals that yield two different bases. We have shown in chapter 1 that signals with limited bandwidth or adjustable bandwidth are desirable in reflectometry applications. In that scope, we have chosen the chirp and the MC signals. Indeed, OMTDR can hardly be regarded as sparse due to is randomness. First, we study the chirp signal as FDR's complex signal. Indeed we will show that the Fractional Fourier Transform (FrFT) leads to a sparse representation. Second, we examine the TDR's real MC signal. In that case, the Discrete Cosine Chirp Transform (DCCT) allows to have a sparse representation of the MC. The theoretical approach, as well as some performance metrics for both proposed sparse basis FrFT and DCCT, are detailed. Since the reflected signal is actually relevant, not only we study the sparseness of the injected signal, but by devoting it, we also study the sparsity of the reflected signal.

3.2 Complex chirp signal

As stationary signals are easily interpreted in their Fourier domain, the frequency domain provides a natural alternative representation to the time domain. Owing to the acquisition and processing implementation, we consider for reflectometry, Discrete Fourier Transform or Fast Fourier Transform (FT). $X(f)$ is the spectrum of $x(t)$; it informs the frequency power of the signal.

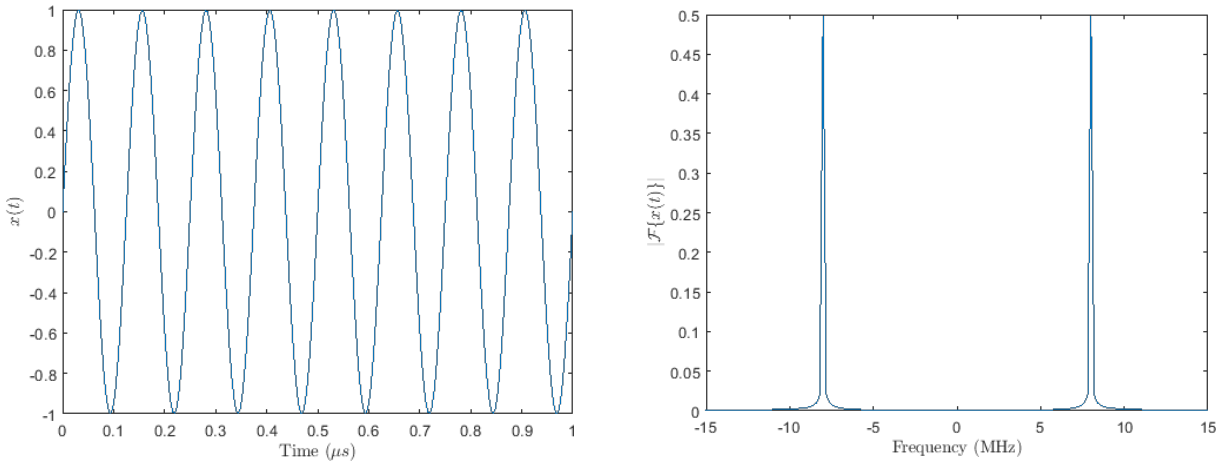

(a) Time domain. (b) Frequency domain.

Figure 3.1: Time and Frequency domain representation of a cosine signal operation at a frequency $f = 8$ MHz ($x(t) = \cos(2\pi f t)$). We can notice that the FT of the $x(t)$ has a sparse representation with only 2 components at $|f| = 8$ MHz different from zero.

As described in equation (3.1), the FT of sinusoidal cosine or sine signal is easily determined. Besides, it shows that the FT of the cosine function with operating frequency at f_1 is constituted of 2 Dirac at $|f| = f_1$.

$$\begin{aligned} x(t) =& \cos(2\pi f_1 t), \quad \text{since} \quad \cos(2\pi f_1 t) = \frac{\exp\left(j2\pi f_1 t\right) + \exp\left(-j2\pi f_1 t\right)}{2}, \\ X(f) =& \frac{1}{2}\left[\int_{-\infty}^{\infty} \exp\left(j2\pi f_1 t\right) \exp\left(-j2\pi f t\right) dt + \int_{-\infty}^{\infty} \exp\left(-j2\pi f_1 t\right) \exp\left(-j2\pi f t\right) dt\right] \\ =& \frac{1}{2}\left[\delta(f - f_1) + \delta(f + f_1)\right]. \end{aligned} \tag{3.1}$$

This is exemplified in Figure 3.1. Of course, the finite time window of acquisition introduces an artifact with respect to the theoretical result. Yet, even for actual implementation, the frequency domain of the cosine signal has a sparse representation; hence,

it is suitable for CS to define it as the sparseness dictionary. However, it will not be valid in the case of a signal occupying a wide frequency range, such as chirp signal and MC signal. Figure 3.2 presents that a broadband linear chirp signal with bandwidth $B = 50$ MHz does not have a sparse representation either in the time nor in the spectral domain. The time domain expression of a chirp (equation (1.11)) clearly shows that only two parameters fully characterize such a signal. From the literature, the FrFT appears to give a sparse representation of the chirp. Therefore, we propose to use the FrFT that will be detailed in the next section.

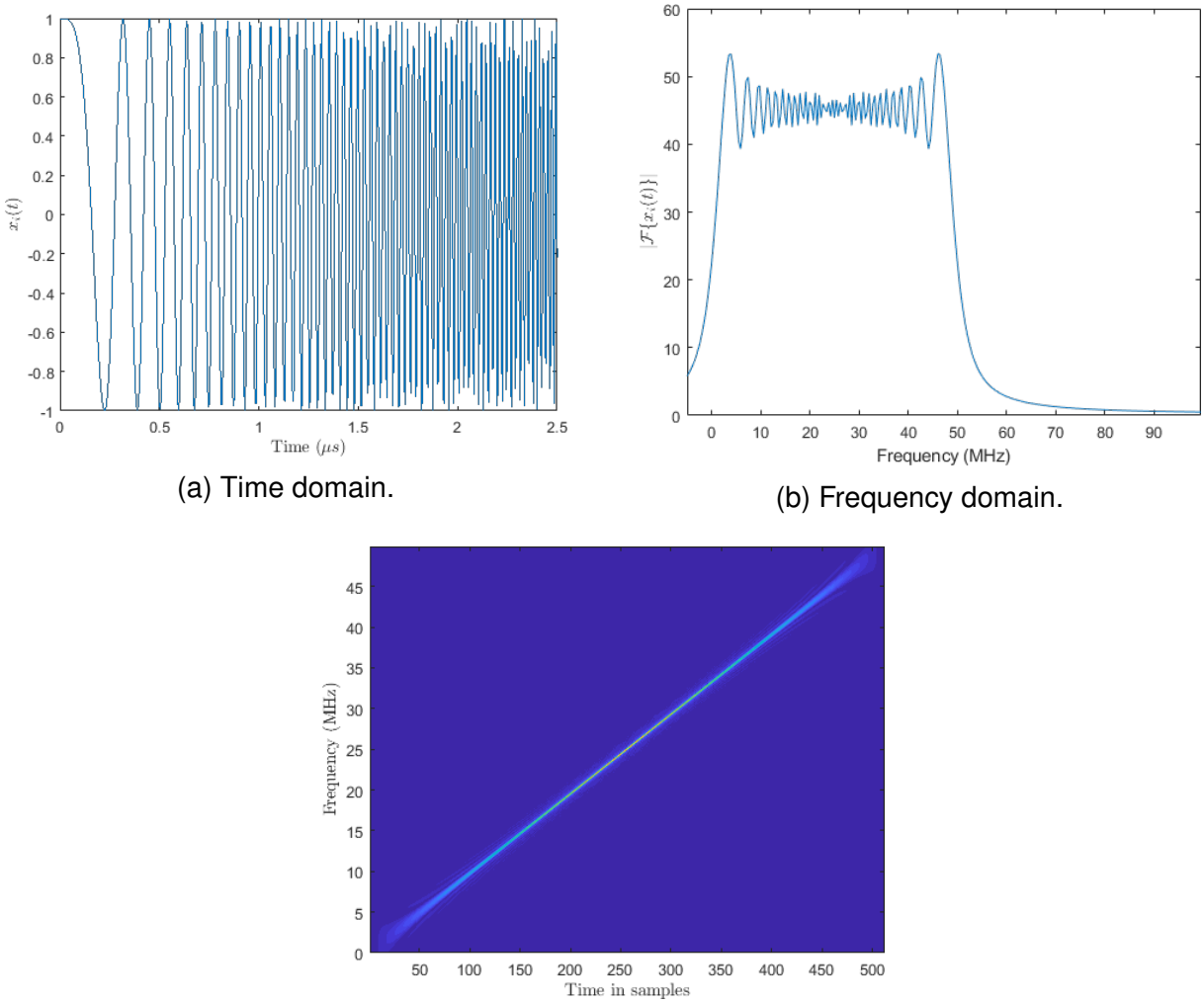

(a) Time domain.

(b) Frequency domain.

(c) Wigner-Ville distribution.

Figure 3.2: Representation of the linear chirp signal with a frequency range 0-50 MHz.

3.2.1 Principles of Fractional Fourier Transform (FrFT)

FrFT [86–88] is a linear transformation generalizing the classical continuous Fourier transform, which essentially projects the time-frequency representation of a signal into a domain where an arbitrary angle rotates the axes.

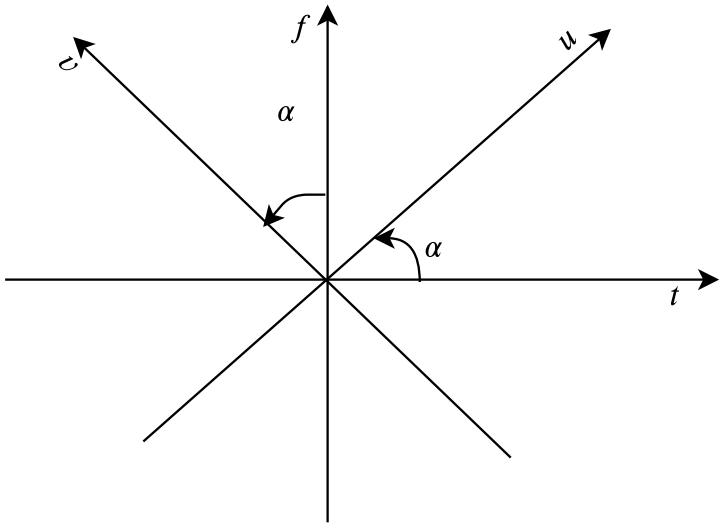

Figure 3.3: The (u, v) plane of FrFT rotated by an angle α relative to the original time-frequency plane (t, f).

The time-frequency representation uses a plane with two orthogonal axes corresponding to the time and frequency (t, f). Whereas, as represented in Figure 3.3, FrFT rotates the axes $(t, f) \rightarrow (u, v)$ with an angle α. Accordingly, the FrFT is defined as:

$$\mathcal{F}^a\{x(t)\} = X_a(u) = \int_{-\infty}^{\infty} x(t) K_a(t, u) dt, \tag{3.2}$$

where $\alpha = a\frac{\pi}{2} \in (-2, 2]$ is the fractional order and $K_a(t, u)$ is the kernel of the transformation which is defined as:

$$K_a(t, u) = \begin{cases} \sqrt{1 - j\cot\alpha}\exp\left(j\pi(u^2\cot\alpha + t^2\cot\alpha - 2ut\csc\alpha)\right) & \text{if } \alpha \text{ is not a multiple of } \pi, \\ \delta(t - u) & \text{if } \alpha \text{ is a multiple of } \pi, \\ \delta(t + u) & \text{if } \alpha + \pi \text{ is a multiple of } 2\pi. \end{cases} \tag{3.3}$$

Indeed, there exist some particular cases while varying α:

- $a = 0 \Leftrightarrow \alpha = 0$; leads to the time domain representation of the signal. This case

represents the identity operator, $\mathcal{F}^0 = \mathrm{I}$.

- $a = 1 \Leftrightarrow \alpha = \frac{\pi}{2}$; leads to the Fourier transform of the signal; therefore $\mathcal{F}^1 = \mathcal{F}$.

- Successive application of α is equivalent to a signal transform with an order equal to the sum of every single order; thus, we can generalize it as fallows: $\mathcal{F}^{a_1}\mathcal{F}^{a_2} = \mathcal{F}^{a_1+a_2}$. Since $\mathcal{F}^a\mathcal{F}^{-a} = \mathcal{F}^{a-a} = \mathcal{F}^0 = \mathrm{I}$, it is clear that FrFT can be inversed exactly as the FT.

In the ordinary Fourier Transform, the rotation from time to frequency axis is applied with a constant angle $\alpha = \frac{\pi}{2}$. However, the FrFT considers a variable rotation of the time-frequency axis by an angle of $0 < |\alpha| < \pi$. Therefore, the FrFT is interpreted as a generalization of the Fourier Transform. The inverse property of the FrFT allows to obtain the signal $x(t)$. It consists of applying an angle $-\alpha$ to the $X_a(u)$. So that $\mathcal{F}^{-a}$ can be expressed as:

$$x(t) = \mathcal{F}^{-a}\{X_a(u)\} = \int_{-\infty}^{\infty} X_\alpha(u) K_{-a}(t,u)dt. \tag{3.4}$$

3.2.1.1 The optimal fractional angle of FrFT for complex linear chirp signal

Let's consider a complex linear chirp with a chirp rate λ and an instantaneous frequency $\theta(t) = 2\pi(f_0 + \lambda t)$:

$$x(t) = A\exp\left(j\left(2\pi f_0 t + \pi\lambda t^2 + q\right)\right), \tag{3.5}$$

where A and q represent the amplitude and the initial phase, respectively. In our case, A is equal to 1, and q to zero. As mentioned earlier, such a signal has a compact expression which relies on only two constants. The aim of the FrFT of an arbitrary angle α of chirp signal $x(t)$ can be written as:

$$\begin{aligned} X_a(u) &= \int_{-\infty}^{\infty} x(t)K_a(t,u)dt \\ &= \sqrt{1 - j\cot\alpha}\exp(j\pi u^2\cot\alpha)\int_{-\infty}^{\infty}\exp\left[j2\pi(f_0 - u\csc\alpha)t\right]\exp\left[j\pi(\lambda + \cot\alpha)t^2\right]dt. \end{aligned} \tag{3.6}$$

In order to find a relation between the chirp rate λ of the linear chirp signal and the fractional rotation angle α, let's consider $\alpha = -\operatorname{arccot}\lambda$ and therefore the equation (3.6)

yields to [86]:

$$X_a(u) = \sqrt{1 - j\cot\alpha}\exp(j\pi u^2\cot\alpha)\delta\left(u - \frac{f_0}{\csc\alpha}\right). \tag{3.7}$$

As we notice, when $\alpha = -\operatorname{arccot}\lambda$, the FrFT of chirp signal corresponds to an impulse representation. Referring to the position of the central frequency f_0 on Fourier f-axis, the new location of the peak on the fractional u-axis is at

$$u = \frac{f_0}{\csc\alpha}, \qquad \text{where} \qquad \csc = \frac{1}{\sin\alpha}. \tag{3.8}$$

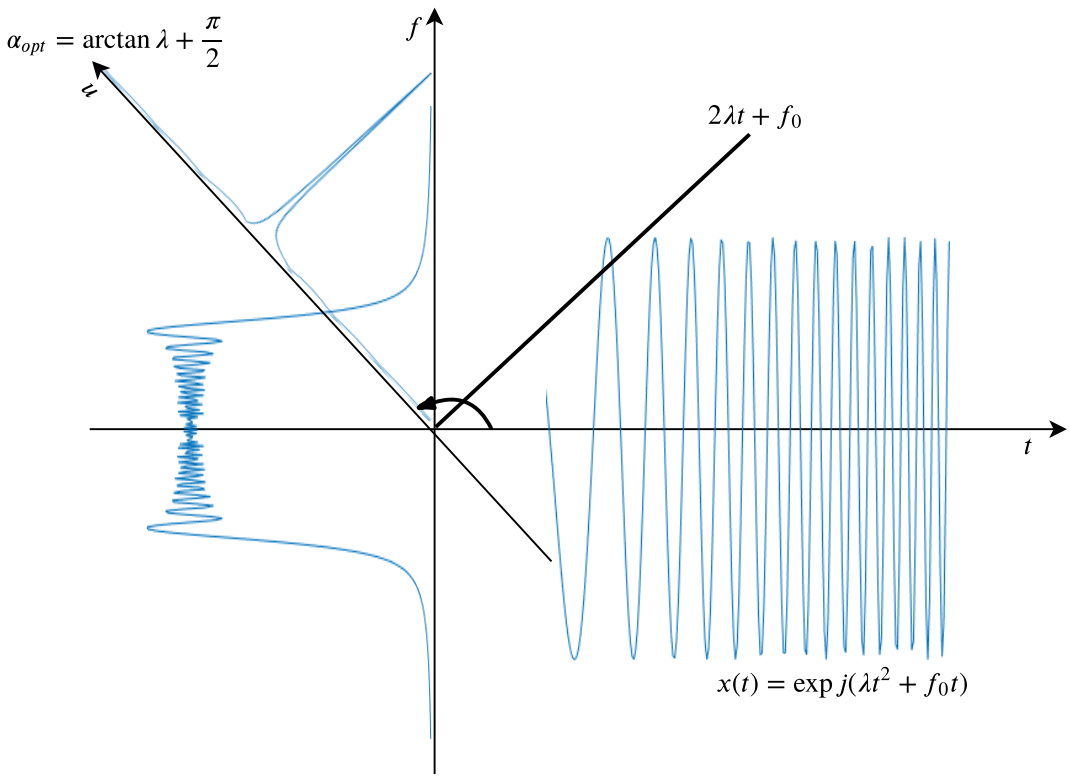

Figure 3.4: This figure provides a different representation of a linear chirp signal. As the projection angle rotates to the optimal, the FrFT of the chirp signal converges to an impulse function.

Wigner-Ville Distribution [1] (WD) of the chirp signal is an impulse function $\delta(f - \lambda t - f_0)$, which distributes the instantaneous frequency $(\theta(t) = 2\lambda t + f_0)$ represented by the straight forming an angle $\arctan \lambda$ with axis t. Figure 3.2c presents the Wigner-Ville distribution of the chirp signal with a frequency range 0-50 MHz. Hence, the optimal rotation angle α_{opt} is defined in equation (3.9). The rotation with an angle α_{opt} of the u-axis will manage to a have vertical representation of the straight line of chirp in WD; thus the integral projection of $\delta(f - \lambda t - f_0)$ onto the u-axis generates an impulse whose value is equivalent to the squared magnitude of $\mathcal{F}^{a_{opt}}\{x(t)\}$. Figure 3.4 provides a different representation of a linear chirp signal. As the projection angle rotates to its optimal value, the FrFT of the chirp signal converges into an impulse function.

$$\alpha_{opt} = \arctan \lambda + \frac{\pi}{2}. \tag{3.9}$$

Finally, when the fractional order of the FrFT matches the optimal value, the transformed signal at the optimal fractional order will be sparser than any other fractional order.

As a result, the time-frequency distribution of a linear chirp signal is a straight line making an angle associated with its chirp-rate in the time-frequency domain, as seen in Figure 3.4. By applying a variable rotation angle, we notice that for an appropriate value of α_{opt}, the straight line representation in the time-frequency plane of the linear chirp is transformed into the most compact form of the signal. Thus, applying this α_{opt} transforms any linear chirp signal into an impulse, where the signal's energy is concentrated into the smallest possible interval, and thereby has the sparsest representation.

3.2.2 Application of α_{opt} to injected signal

Considering the linear chirp signal, mostly used for FDR, and choosing to project it in the FrFT allow access to a domain between temporal and spectral called fractional. Therefore, we illustrate how the FrFT can be used for complex chirp signal and gives the sparser signal. The experiments are conducted based on different types of networks. In the considered examples, and without loss of generality, the proposed injected signal $x_i(t)$ is a complex linear chirp occupying a bandwidth of $B = 50$ MHz,

[1] Wigner-Ville Distribution (WD) of a temporal signal $x(t)$ is denoted as : $WD_x(t,f) = \int_{-\infty}^{\infty} x\left(t + \frac{\tau}{2}\right) x^*\left(t + \frac{\tau}{2}\right) \exp(-j2\pi f\tau) d\tau$. Moreover, the integral projection of WD_x onto the u-axis is equal to the squared magnitude of the $\mathcal{F}^a\{x(t)\}$.

as denoted in equation (3.5) where A is equal to 1, f_0 and q are zero. Since we control all the major characteristics of the injected signal, therefore we first calculate the value of α_{opt_i} theoretically. The projection of $x_i(t)$ in the FrFT with the calculated angle $\alpha_{opt_i} = 1.814$ rad/s is represented in Figure 3.5. Note that, $\alpha_{opt_i} = a_{opt_i}\frac{\pi}{2} \Leftrightarrow a_{opt_i} = 1.155$. The particular $\mathcal{F}^{a_{opt_i}}\{x(t)\}$ transforms the non-sparse complex signal to a completely sparse one, where $\mathbf{s_i}$ has a single active component. Thus, the measurement matrix for the injected signal is the inverse of $\mathcal{F}^{-a_{opt_i}}$, because of $\mathbf{x_i} = \mathcal{F}^{a_{opt_i}}\mathbf{s_i}$.

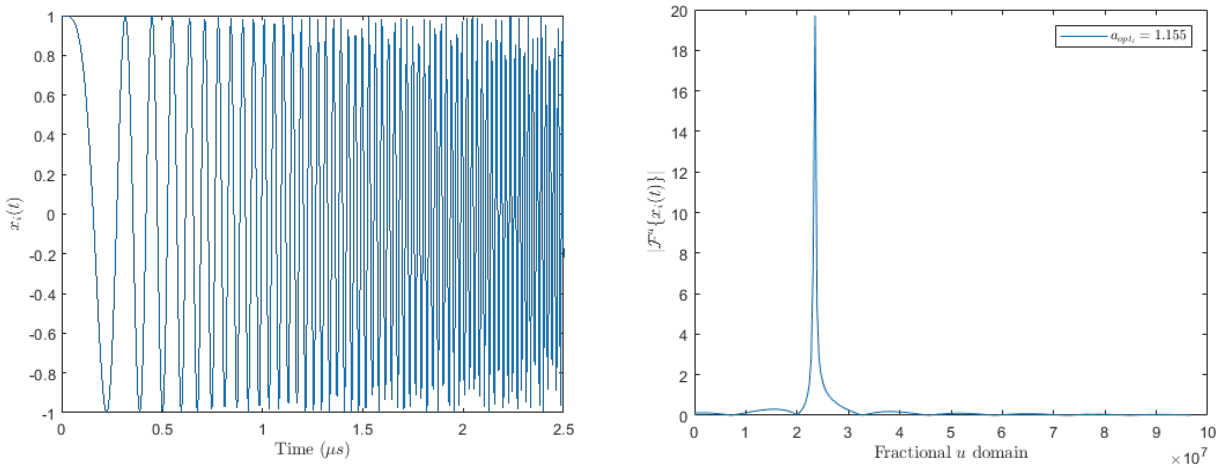

(a) Time domain.

(b) FrFT domain.

Figure 3.5: Time domain representation of the injected signal with a bandwidth 0-50 MHz and the sparse representation of $x_i(t)$ using FrFT with the theoretically calculated angle of rotation $\alpha_{opt_i} = 1.815$ rad/s. Note that $\alpha_{opt_i} = a_{opt_i}\frac{\pi}{2}$.

Besides, the choice of optimal angle is essential for the sparseness degree. Therefore, on a multiple choice of rotational angle, we simulate and calculate the sparsity degree based on those α by $\frac{||\mathbf{s_i}||_1}{||\mathbf{s_i}||_2}$, where $\mathbf{s_i}$ is the sparse coefficients representing the injected signal. Figure 3.6 shows the convergence between the calculated α_{opt_i} from equation (3.9) and the simulated one.

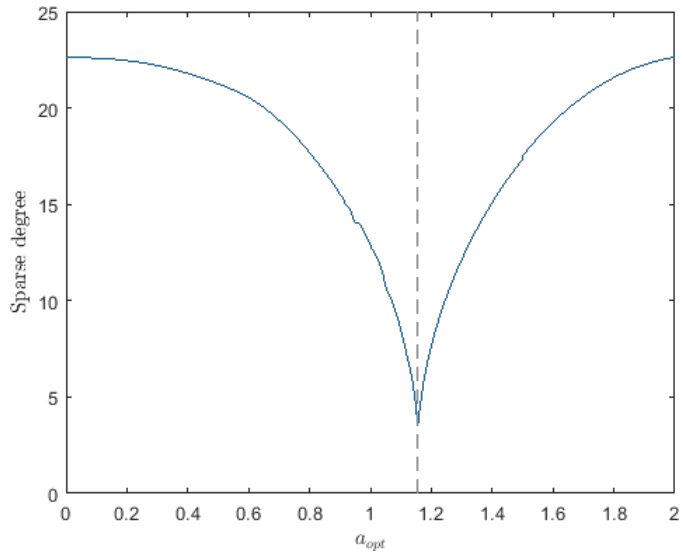

Figure 3.6: In blue the choice of the $\alpha_{opt_i}$for the injected signal. The dashed line in gray represent the value of the calculated a_{opt_i}. Note that $\alpha_{opt_i} = a_{opt_i}\frac{\pi}{2}$.

3.2.3 Application of α_{opt} to reflected signal

In fact, any wire diagnosis system relies on the study of the reflected signal because it contains all the information about network health. Therefore a study on that signal is necessary. Whereas, not only the act of sub-sampling the reflected signal will lead to lose those hidden information but also it is entirely unknown. Consequently, the sparse signal representation is firstly applied to the injected signal and later approved for the reflected one. For instance, in our study, we try to characterize and identify the location of defects causing a total reflection. Hence, open or short defects are responsible for a total reflection of the injected signal. Whatever the bandwidth frequency of the signal is, the rate of variation of the $x_r(t)$ is identical to that of $x_i(t)$. For once, we suppose that the reflected signal is sampled periodically according to Shannon-Nyquist frequency; therefore we calculate the FrFT coefficients $\mathbf{s_r}$ for different values of α. The sparsity degree based on those α is assessed by $\frac{||\mathbf{s_r}||_1}{||\mathbf{s_r}||_2}$, $\mathbf{s_r}$ is the sparse coefficients responsible for the reflected signal. Hence, based on simulation, we verify this hypothesis for a point-to-point and complex network.

●Point-to-point wire

Considering that the chirp signal is injected into a point-to-point $100\,$m cable with $Z_c = 73\,\Omega$ and a hard defect (open circuit) at the extremity. Initially, we focus on the choice of

the optimal angle. Accordingly, we compare the sparsity degree of the reflected signal with the injected one, as illustrated in Figure 3.7b. The trends marked by the two lines have roughly the same minimum; hence, the same optimal angle. Equally important, we notice that the sparsity of the reflected signal is maximized in the FrFT domain when the fractional order α_{opt_r} is equal to 1.82 rad/s ($a_{opt_r} = 1.159$) this value is close to the calculated α_{opt_i}. Thus the calculated optimal rotation angle for sparse representation of the input signal can be applied for the reflected one. As illustrated in Figure 3.7, for the $\alpha_{opt_i} = \alpha_{opt_r}$ both signals have a few non-zero coefficients.

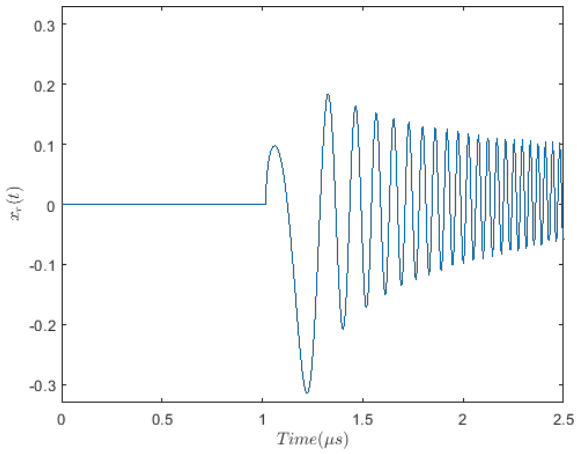

(a) Time domain.

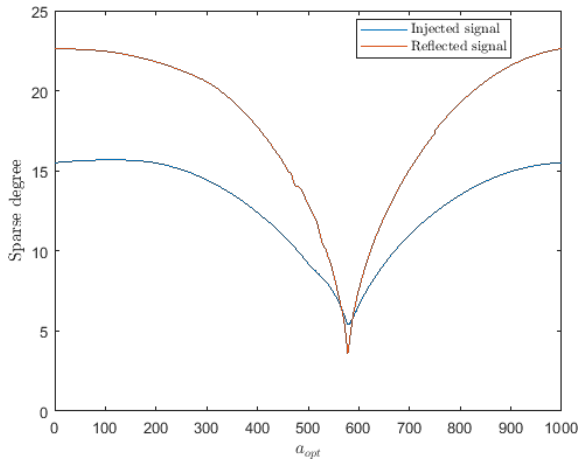

(b) The sparse degree of the reflected signal (in blue) compared with the injected one (in red).

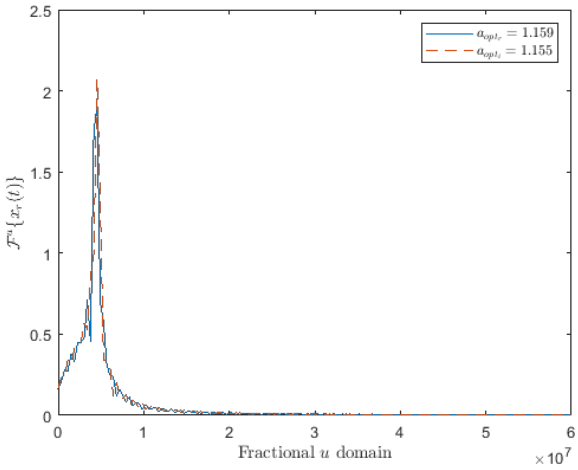

(c) FrFT domain.

Figure 3.7: Time domain representation of the reflected signal in point-to-point wire and the sparse representation of $x_r(t)$ using FrFT while the theoretically calculated angle of rotation $\alpha_{opt_r} = 1.82$ rad/s.

●Complex Y-Network

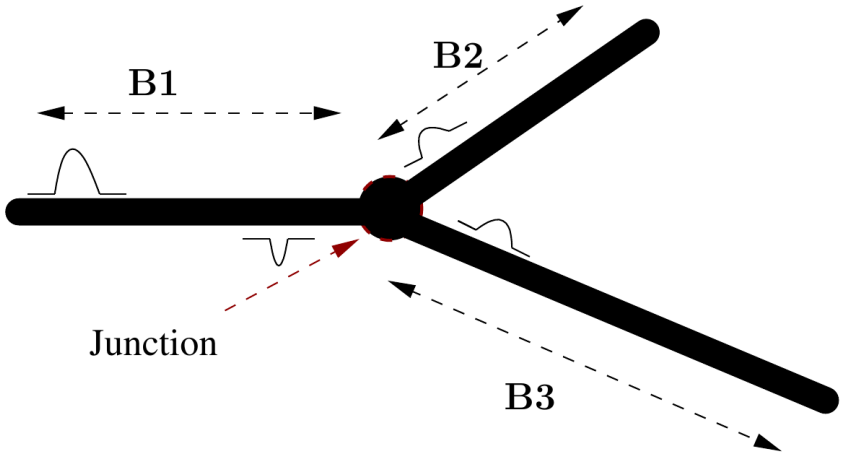

Figure 3.8: The layout of the NUT considered, with a characteristic impedance $Z_c = 50\,\Omega$. The three lines $[\mathbf{B1}, \mathbf{B2}, \mathbf{B3}]$ are of respective length $[24,18,32]$ meters, where the extremities of $\mathbf{B2}$ and $\mathbf{B3}$ are charged by $Z_l \gg Z_c$.

The chirp signal is applied to a coaxial Y-branches network with a characteristic impedance $Z_c = 50\,\Omega$. The presence of a junction and such a network cause multiple reflections. This complex network has a junction connecting both lines $\mathbf{B2}$ and $\mathbf{B3}$ to the first one $\mathbf{B1}$, as illustrated in Figure 3.8. The three lines $[\mathbf{B1}, \mathbf{B2}, \mathbf{B3}]$ are of length $[24,18,32]$ meters, respectively. Each line $\mathbf{B2}$ and $\mathbf{B3}$ is loaded by an impedance $Z_l \gg Z_c$ (hard defect) at its extremity.

The representation of the signal in the so-called fractional Fourier domains and when applying the optimal rotation angle, the magnitude spectrum of the FrFT is the most compact. Since the frequency range of the injected signal remains the same $B = 50$ MHz, the calculated rotation angle for sparse representation of the input signal $x_i(t)$ will not vary, $\alpha_{opt_i} = 1.815$ rad/s. Even though, a complex network causes multiple reflections, the fact that a hard defect causes a total reflection whatever the frequency of the signal is, the rate of variation of the $x_r(t)$ will be stable. As illustrated in Figure 3.9, for both α_{opt} angle, the reflected signal remains sparse.

Once the sparse coefficient $\mathbf{s_r}$ is recovered with the OMP algorithm, the reflected signal $\mathbf{x_r} = \mathcal{F}^{-a_{opt_i}}\mathbf{s_r}$ is reconstructed where $\mathbf{\Psi} = \mathcal{F}^{-a_{opt_i}}$ represents the FrFT matrix relative to the optimal angle calculated for the injected signal. Indeed, other methods, like augmenting the dictionary length, can be adopted for the selection of the optimal

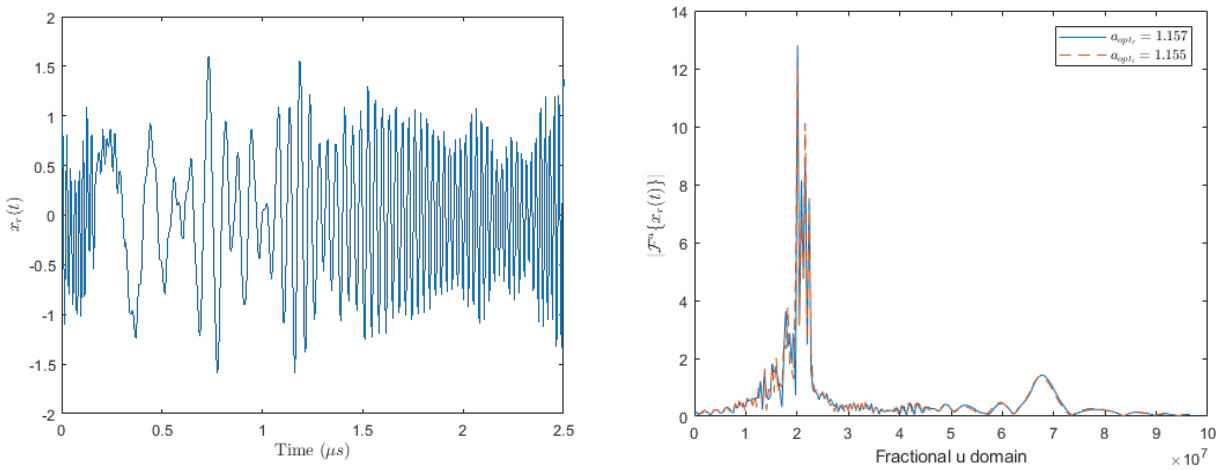

(a) Time domain.

(b) FrFT domain.

Figure 3.9: Time domain representation of the reflected signal in a Y-Network and the sparse representation of $x_r(t)$ using FrFT while the theoretically calculated angle of rotation $\alpha_{opt_r} = 1.818$ rad/s.

value of α; however, the proposed approach based on the prior knowledge of the injected signal is preferred due to its simplicity.

On the other hand, generally, the use of high-frequency or high data rate signals provides better performance for reflectometry. However, other factors than the requirement of powerful data processing or high-speed sampling, which limits the performances of high-frequency reflectometry are the attenuation and the dispersion. Indeed, those factors are related to the electrical characteristics of the cable.

● Attenuation impact

According to equation (1.6), the attenuation is related to the linear resistance of the cable [34]. Besides, the attenuation in any network is more significant when either the frequency of the incident signal or the propagation distance increases [36]. As for the dispersion introduces a loss in fault localization accuracy because of the fact that the high frequency components of the signal propagate at a higher speed than those at low frequency.

Consequently, some frequency bands can be completely attenuated. In fact, this results that the reflected signal will lose its sparseness degree. We apply different studies to prove our hypothesis. Our first study is applied on a point-to-point network with two different real cases of electrical characteristics ($RLCG$) wire. Figure 3.10 represents

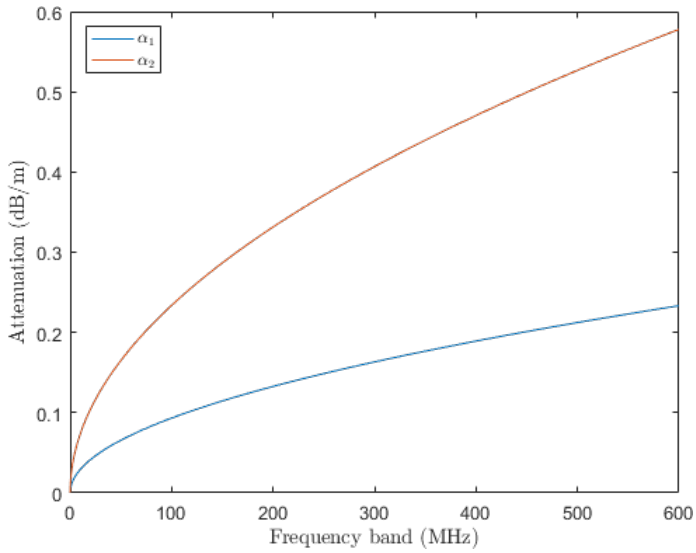

Figure 3.10: Attenuations versus the frequency, where α_1 and α_2 are the attenuations of a different type for real case wires.

the attenuations α_1 and α_2 of real case wires versus the frequency. As we notice, the attenuation of high frequencies in the second wire is more critical than in the first one. We test on multiple bandwidths of x_i, and we estimate the sparse degree κ for the reflected signal with the transformation applied by the calculated optimal angle α_{opt_i} corresponding to the injected signal. Our second study is applied to the previously proposed complex Y-Network (Figure 3.8) with an attenuation α_1. Figure 3.11 and Figure 3.12 illustrate the sparse degree variation of the simple and complex network, respectively. This latter validates our hypothesis. For both point-to-point wire or Y-Network, increasing the band of the testing signal increases the sparsity degree of the reflected one. Moreover, the more the attenuation is significant ($\alpha_2 > \alpha_1$), the sparse is the signal; thus, the attenuation is critical since it alters the sparsity of the reflected signal. As seen previously, the good approximation of the sparsity degree is essential for the performances of the reconstruction of the signal.

Consequently, as demonstrated, the choice of the FrFT dictionary is adaptable for both point-to-point and complex-Y network. However, the choice of the cable is essential because the attenuation modifies the characteristic of the initially determined dictionary by the injected signal — furthermore, the attenuation and the compression factor results to the increment of the sparsity.

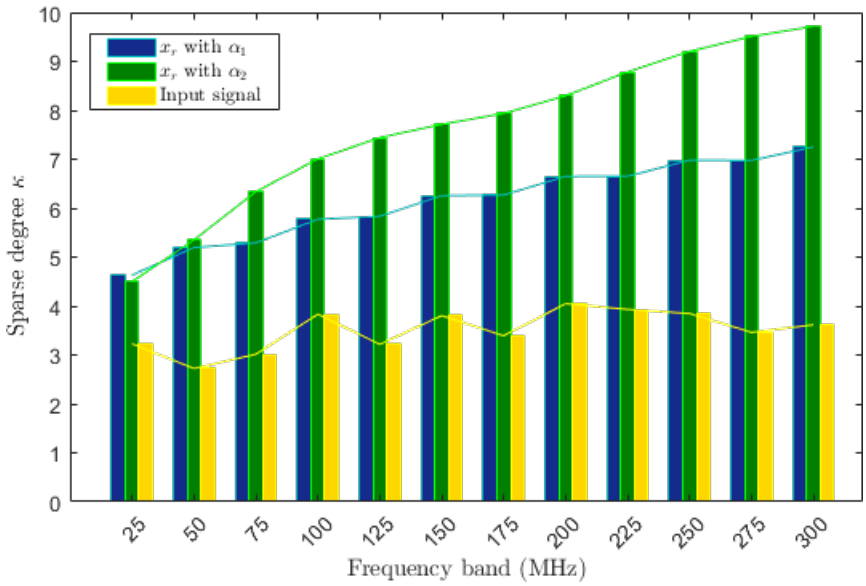

Figure 3.11: The sparse degree estimation of the reflected signal versus different frequency bands in a point-to-point wire.

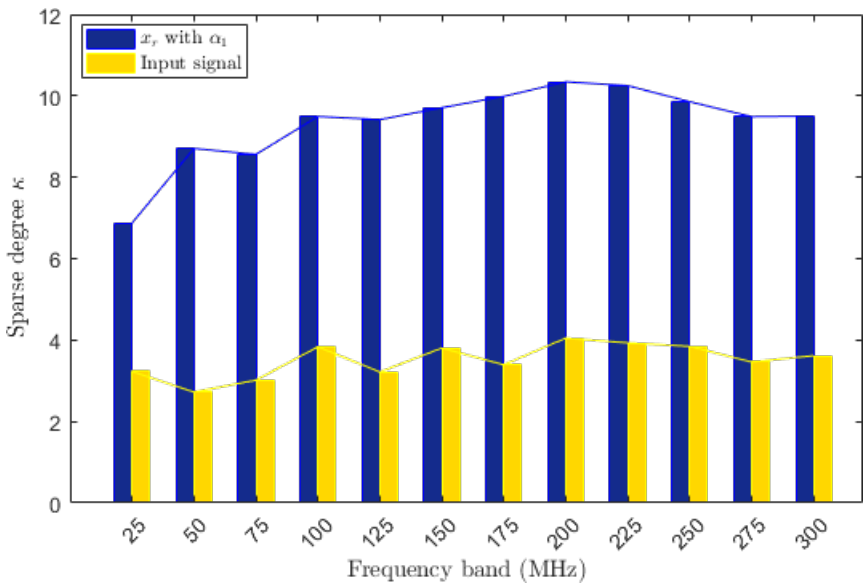

Figure 3.12: The sparse degree estimation of the reflected signal versus different frequency bands in complex Y-Network represented in Figure 3.8.

3.3 Real Multi-Carrier (MC) signal

Since the FrFT provides great sparse representation for complex linear chirp signal, we introduce in this section a new transformation for real MC signals in which a real

transformation is applied. This latter property is required in some applications to provide better performance. Considering the MCTDR, which uses a real MC signal, we introduce the Discrete Cosine Chirp Transform (DCCT) and its inverse [89]. This conversion process is based on orthogonal real linear chirp transformation. Therefore, the DCCT, just like the FrFT, is used to convert a non-sparse representation of a signal in time or frequency domains into a sparse signal. As a matter of fact, the DCCT is a generalization of the Discrete Cosine Transform (DCT). Also, this transformation uses real bases (real linear chirps), and it is not a time-frequency transformation, but rather a frequency chirp-rate transformation.

Here in this section, first, we present the definition and the implementation of the DCCT. Second, we show the results of the transformation obtained for MCTDR signal.

3.3.1 Principles of Discrete Cosine Chirp Transform (DCCT)

3.3.1.1 Theory

This section is devoted to the development of an orthogonal representation by applying the DCCT to a discrete real-valued signal, $\mathbf{x}[\mathbf{n}]$. Unlike the FT and DCT, the DCCT has two variables β and f. The kernel in cosine terms of the DCCT

$$\phi_{\beta,\mathbf{k}}[\mathbf{n}] = \cos\left(\frac{\beta\pi\mathbf{n}^2 + \mathbf{k}\pi(\mathbf{2n}+1)}{2\mathrm{N}}\right) \quad \text{where} \quad \begin{cases} 0 \leqslant \mathbf{k} \leqslant \mathrm{N}-1, \\ \Lambda \leqslant \beta < \Lambda, \\ 0 \leqslant \mathbf{n} \leqslant \mathrm{N}-1. \end{cases} \tag{3.10}$$

is characterized by its finite chirp rate β and the discrete frequency $\frac{2\pi\mathbf{k}}{\mathrm{N}}$. Also, the instantaneous frequency of the cosine is

$$\mathsf{IF}(\mathbf{n},\mathbf{k}) = \frac{\pi}{\mathrm{N}}(\beta\mathbf{n}+\mathbf{k}). \tag{3.11}$$

Therefore the coefficients $\mathbf{X}[\mathbf{k},\beta]$ of the transformation is obtained by

$$\mathbf{X}[\mathbf{k},\beta] = \sum_{\mathbf{n}=0}^{\mathrm{N}-1} \mathbf{x}[\mathbf{n}] \cos\left(\frac{\beta\pi\mathbf{n}^2 + \mathbf{k}\pi(\mathbf{2n}+1)}{2\mathrm{N}}\right). \tag{3.12}$$

It is obvious to realize that DCCT for $\beta = 0$ is the generalization of DCT up to a scalar factor:

$$\mathbf{X}[\mathbf{k}, 0] = \sum_{\mathbf{n}=0}^{\mathrm{N}-1} \mathbf{x}[\mathbf{n}] \cos\left(\frac{\mathbf{k}\pi(\mathbf{2n}+1)}{2\mathrm{N}}\right). \tag{3.13}$$

The notable difference between the DCT and DCCT is that while compressing with DCCT, we need to master the used chirp rates to obtain a sparse representation of the original signal. The original signal $\mathbf{x}[\mathbf{n}]$ where $0 \leqslant \mathbf{n} \leqslant \mathrm{N}-1$ is obtained by Inverse DCCT operation:

$$\text{IDCCT}\{\mathbf{X}[\mathbf{k}, \beta]\} = \mathbf{x}[\mathbf{n}] = \sum_{\beta=-\mathbf{\Lambda}}^{\mathbf{\Lambda}-\mathbf{1}} \sum_{\mathbf{k}=\mathbf{0}}^{\mathrm{N}-1} \frac{2\mathbf{X}[\mathbf{k}, \beta]}{2\Lambda\mathrm{N}} \cos\left(\frac{\beta\pi\mathbf{n}^2 + \mathbf{k}\pi(\mathbf{2n}+1)}{2\mathrm{N}}\right). \tag{3.14}$$

3.3.1.2 Implementation

Since DCCT is the generalization of the DCT, its software or hardware implementation is similar to DCT and the Fast Fourier transform algorithm (FT).

- **DCCT**

  Referring to equation (3.12), we can write the following equation:

$$\mathbf{X}[\mathbf{k}, \beta] = \mathrm{Re}\left\{\exp\left(-j\frac{\pi\mathbf{k}}{2\mathrm{N}}\right) \sum_{\mathbf{n}=0}^{2\mathrm{N}-1} \underbrace{\left[\mathbf{x}[\mathbf{n}] \exp\left(-j\frac{\beta\pi\mathbf{n}^2}{2\mathrm{N}}\right)\right]}_{\mathbf{h}[\mathbf{n},\beta]} \exp\left(-j\frac{2\pi\mathbf{kn}}{2\mathrm{N}}\right)\right\}, \tag{3.15}$$

  where Re represents the real part of the exponential. The factor $\mathbf{h}[\mathbf{n}, \beta]$ introduces the decomposition of the signal with the chirp rate β. Also, when β is null the above equation is nothing else than the DCT transformation. Defining $\mathbf{H}[\mathbf{k}, \beta] = \mathcal{F}\{\mathbf{h}[\mathbf{n}, \beta]\}$ and $\mathbf{h}[\mathbf{n}, \beta] = 0$ for all $\mathbf{n} \in [\mathrm{N}, 2\mathrm{N}-1]$, the equation (3.15) is expressed as follow:

$$\mathbf{X}[\mathbf{k}, \beta] = \mathrm{Re}\left\{\exp\left(-j\frac{\pi\mathbf{k}}{2\mathrm{N}}\right) \mathbf{H}[\mathbf{k}, \beta]\right\}. \tag{3.16}$$

- **IDCCT**

  In this transformation, we can use the inverse FT algorithm.

$$\begin{aligned}\mathbf{x}[\mathbf{n}] &= \mathrm{Re}\left\{\frac{1}{\Lambda}\sum_{\beta=-\Lambda/2}^{\Lambda/2-1}\underbrace{\left[\sum_{\mathbf{k}=0}^{2\mathrm{N}-1}\mathbf{F}[\mathbf{k},\beta]\exp\left(j\frac{2\pi\mathbf{kn}}{2\mathrm{N}}\right)\right]}_{\mathbf{f}[\mathbf{n},\beta]}\exp\left(j\frac{\beta\pi\mathbf{n}^2}{2\mathrm{N}}\right)\right\} \\ &= \mathrm{Re}\left\{\frac{1}{\Lambda}\sum_{\beta=-\Lambda/2}^{\Lambda/2-1}\mathbf{f}[\mathbf{n},\beta]\exp\left(j\frac{\beta\pi\mathbf{n}^2}{2\mathrm{N}}\right)\right\},\end{aligned} \tag{3.17}$$

  for $\mathbf{F}[\mathbf{k},\beta] = \frac{2}{\mathrm{N}}\mathbf{X}[\mathbf{k},\beta]\exp\left(j\frac{\pi\mathbf{k}}{2\mathrm{N}}\right)$ where $\mathbf{F}[\mathbf{k},\beta] = 0$ when $\mathbf{k} \geq \mathrm{N}$ and $\mathbf{f}[\mathbf{n},\beta]$ is its inverse FT.

Figure 3.13 shows an example of the DCCT and its inverse representation of the signal $\mathbf{x}[\mathbf{n}]$ given below (equation (3.18)), where in this case the calculated Root Mean Squared Error (RMSE) between the reconstructed signal and the original is close to 0.001%, which is a relatively good approximation based on [89]. Moreover, mainly two peak locations are expected: $\beta_1 = 0.2$ and $\beta_2 = 0.05$. As shown in Figure 3.13b, the concentration at $\beta_2 = 0.05$ is more important because of the factor 2 in the equation. However, the more the signal is complex, the more the identification of the optimal β is difficult.

$$\mathbf{x}[\mathbf{n}] = \cos\left(\frac{\pi}{1024}(0.2n^2 + 50(2n+1))\right) + 2\cos\left(\frac{\pi}{1024}(0.05n^2 + 300(2n+1))\right). \tag{3.18}$$

We apply the DCCT to MCTDR signal occupying a bandwidth of $[0 - 50]$ MHz. As we notice in Figure 3.14, the concentration of β for this signal is mainly for $\beta = 1$ and $\beta = -1$. Moreover, as illustrated in Figure 3.14d the reconstruction error is on the order of 0.01 where the RMSE is equal to 0.03%. Such an error is low enough to ensure that the correlation between the original and the reconstructed signal will converge.

3.3.2 DCCT with CS

In the above section, we detail a study on the DCCT transformation of the MCTDR type signal. This transformation leads to have a small number of a non-zero coefficient. Hence, in the general CS measurement expression $\mathbf{y} = \mathbf{\Phi\Psi s}$ (equation (2.4)), in

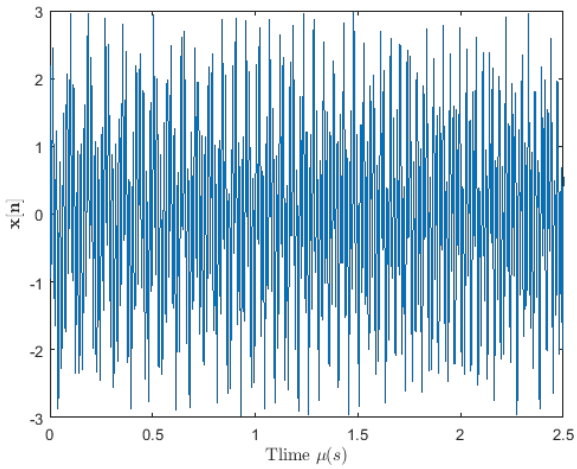

(a) Time domain.

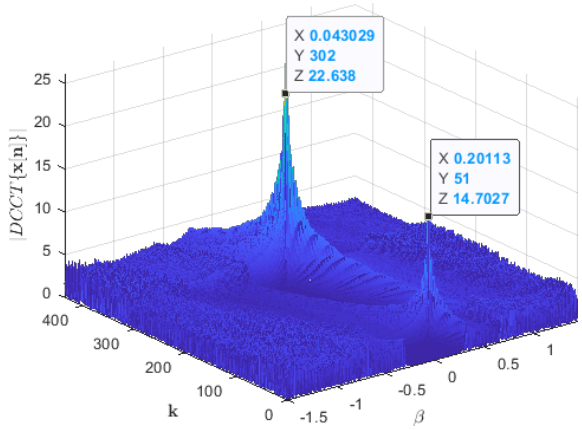

(b) DCCT domain.

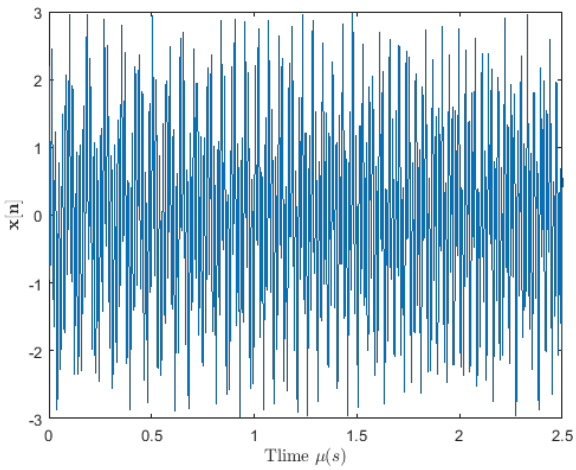

(c) Reconstructed $\mathbf{x}[\mathbf{n}]$ by IDCCT.

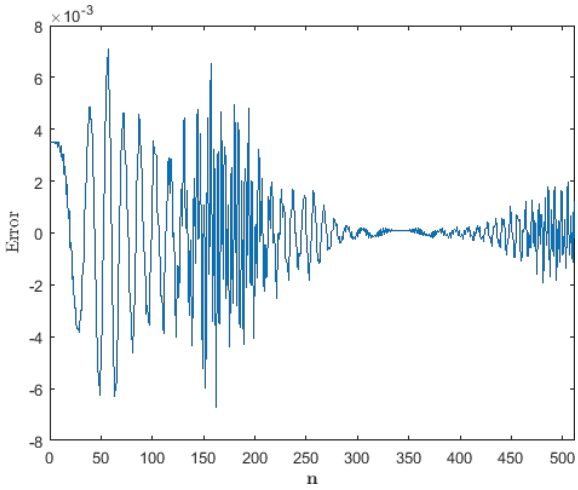

(d) The reconstruction error.

Figure 3.13: Example of the signal $\mathbf{x}[\mathbf{n}]$ in time and DCCT domain and its reconstruction.

which $\mathbf{s} = \mathbf{X}[\mathbf{k}, \beta]$ indicates the amplitude of $[\mathbf{k}, \beta]$ components of $\mathbf{x}$, and $\mathbf{\Psi}$ is given by IDCCT matrix. Moreover, generally, the signal $\mathbf{x}$ is made up only of small projections of chirps where $\mathbf{X}[\mathbf{k}, \beta]$ is sparse. However, based on equation (3.14), the basis $\mathbf{\Psi}$ is over parameterized:

$$\mathbf{\Psi} = [\psi(\mathbf{k}_1, \beta_1) \cdots \psi(\mathbf{k}_1, \beta_V)| \cdots |\psi(\mathbf{k}_U, \beta_1)\, u \cdots \psi(\mathbf{k}_U, \beta_V)] \tag{3.19}$$

where $\mathbf{k} \in [\mathbf{k}_1, \cdots, \mathbf{k}_U]$ represents the frequency and $\beta \in [\beta_1, \cdots, \beta_V]$ represents the chirp rate. Note that U and V are the numbers of samples of the frequency and the

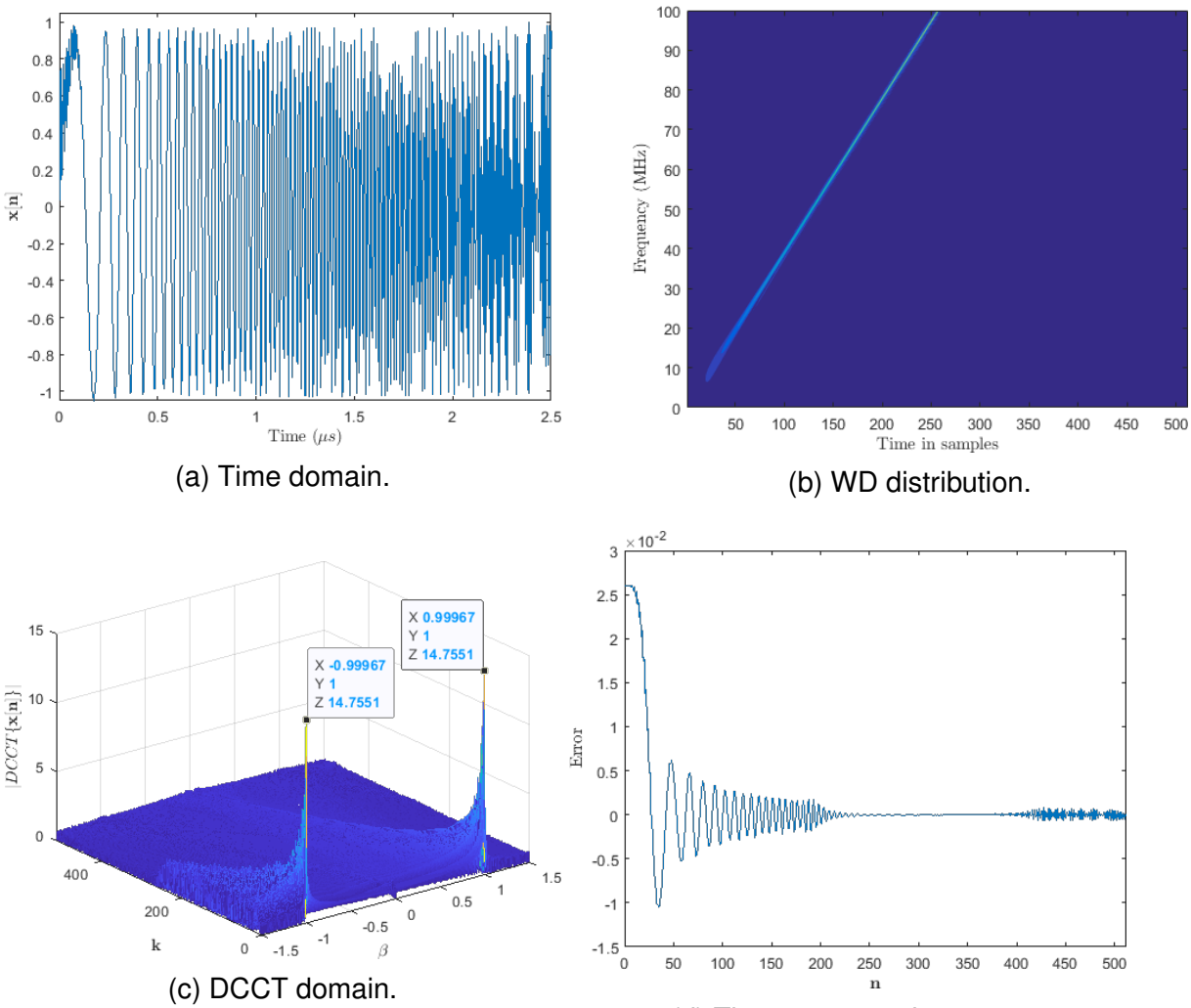

(a) Time domain.

(b) WD distribution.

(c) DCCT domain.

(d) The reconstruction error.

Figure 3.14: MCTDR signal representation in time and DCCT domain as well as the reconstruction error.

chirp rate, respectively. Therefore, we have an overcomplete basis $\mathbf{\Psi}$ with chirp parameters, and in order to obtain better resolution performances, we adapt the sparse reconstruction algorithm OMP to estimate the correct chirp parameters via DCCT basis independently. In this case, the OMP algorithm loops on three different steps:

- The first step consists of finding non-zero locations of the $(\mathbf{k}, \beta)$ pairs using DCCT,
- The second step is to update the linear least square solution,
- The third step finds the magnitude of these non-zero pairs.

These steps will be repeated recursively until a sufficiently small residual is obtained. Such optimization allows detection of several non-zero locations instead of a single one, as well as it focuses on significant $(\mathbf{k}, \beta)$ pairs and suppresses the side lobes. Figure 3.15 shows the original and the recovered DCCT coefficients for the same multi-carrier signal. It is clear that CS filters the DCCT side-lobes and enhances the performance resolution. Furthermore, since the error between the original MCTDR and the reconstructed signal by the recovered DCCT coefficients with CS is decreased (Figure 3.15c), therefore an enhancement of the performance resolution is achieved. This phenomenon is observed in other articles, where using CS recovery with a proper transformation dictionary that gives sparsity established a very proper solution [89, 90].

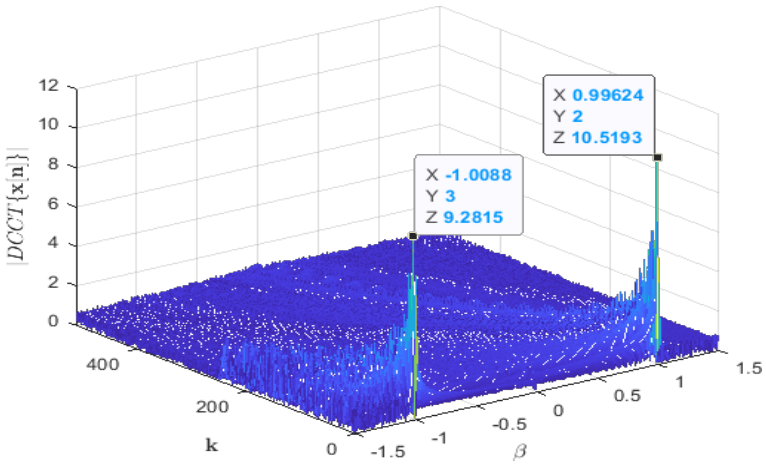

(a) Original DCCT coefficients.

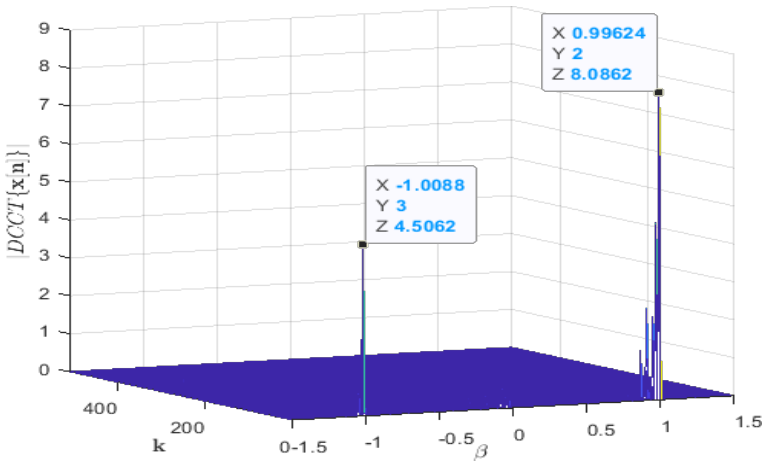

(b) Recovered DCCT coefficients with CS.

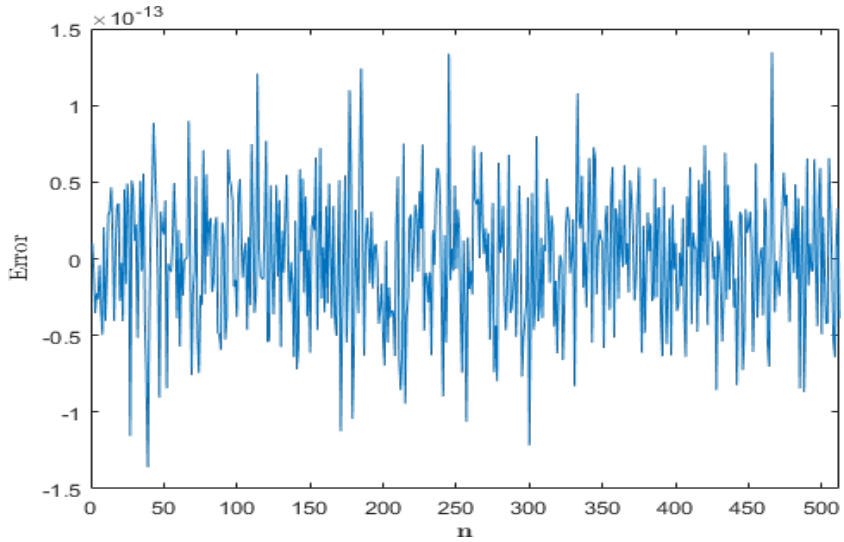

(c) The error between the original MCTDR and the reconstructed signal by the recovered DCCT coefficients with CS.

Figure 3.15: 3-D plot of DCCT coefficients of MCTDR signal occupying a bandwidth of $[0-50]$ MHz.

3.3.3 Simulation results and figure of merit

In this section, we study the DCCT basis on the reflected MCTDR signal for point-to-point wire and complex Y-Network. Since the reflected signal is entirely unknown and depends on the characteristic of the NUT, therefore we had proposed a prior study on the injected signal while using the chirp signal. Such a case requires control on the injected signal and an estimation of its chirp rate. However, in this case, the limitation of the reconstruction's performance is caused by the study on the injected signal and the use of regular DCCT basis. Therefore, to circumvent those conditions, the recursive reconstruction algorithm is used. Thus, without specifying any condition, the CS-DCCT discovers precise peaks at exact locations and correctly reconstructs the reflected signal. Figure 3.16 shows the results for regular DCCT and the CS-DCCT coefficients, respectively for the same point-to-point wire detailed earlier. Obviously, the non-zero $(\mathbf{k}, \beta)$ pairs of the injected signal (Figure 3.15a) are modified in the reflected MCTDR (Figure 3.16a). This phenomenon is solved by CS-DCCT, which does not require any information about the sparsity of the signal.

Moreover, the CS-DCCT correctly estimates the peak locations and sufficiently suppresses side lobes, which provides a successful reconstruction of the signal (an abso-

lute error on the order of 10^{-13}). A related example is given in Figure 3.17 for the complex Y-Network where the proper peaks are easily localized in the $(\mathbf{k}, \beta)$ domain by CS-DCCT method. Figure 3.18 shows the percentage of reconstructed error as a function of a various frequency band of MCTDR signal. It shows that for different electrical characteristics of a wire, the reconstructed error increases, but remains in its minimal cases. Consequently, the updated format of the dictionary is able to have good reconstruction fidelity and efficiency at the same time.

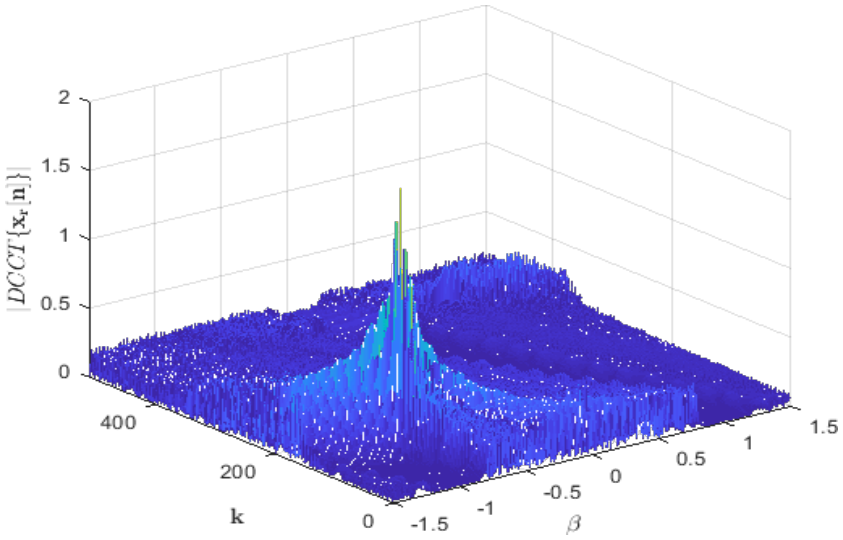

(a) Original DCCT coefficients.

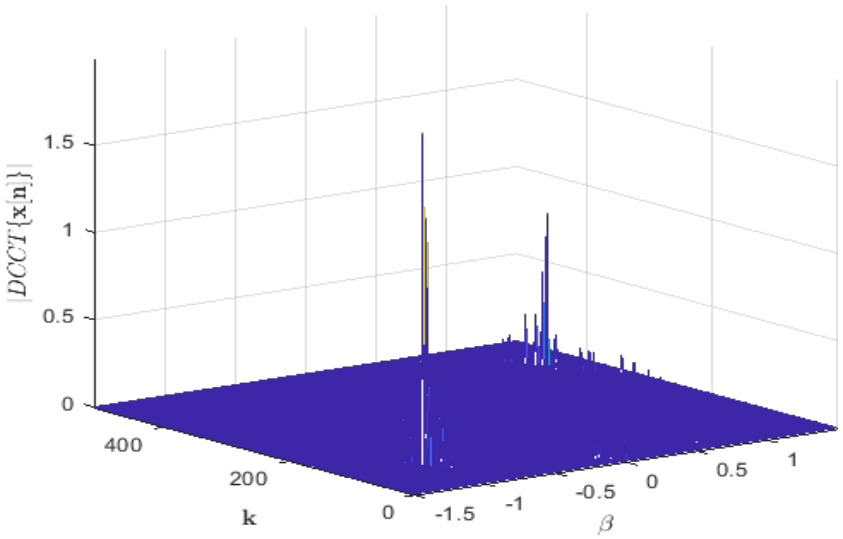

(b) Recovered DCCT coefficients with CS.

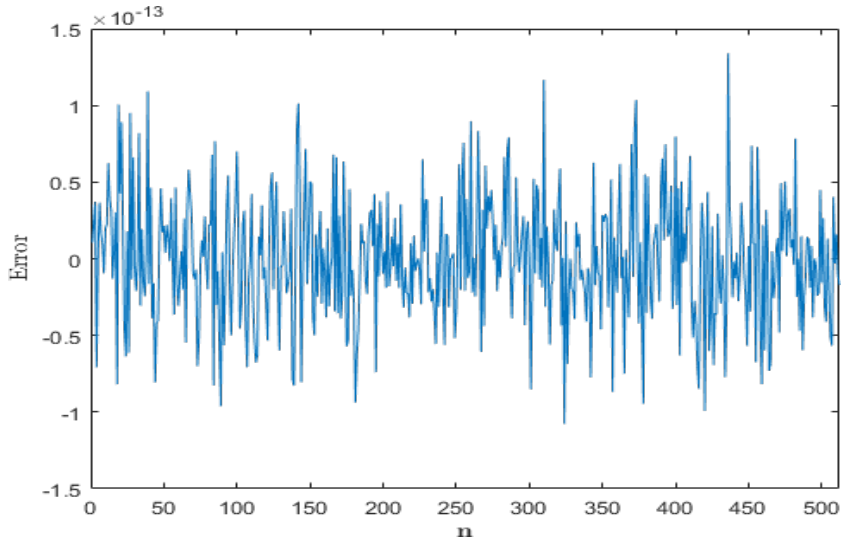

(c) The error between the original MCTDR and the reconstructed signal by the recovered DCCT coefficients with CS.

Figure 3.16: 3-D plot of DCCT coefficients of the reflected MCTDR signal occupying a bandwidth of $[0-50]$ MHz in point-to-point wire.

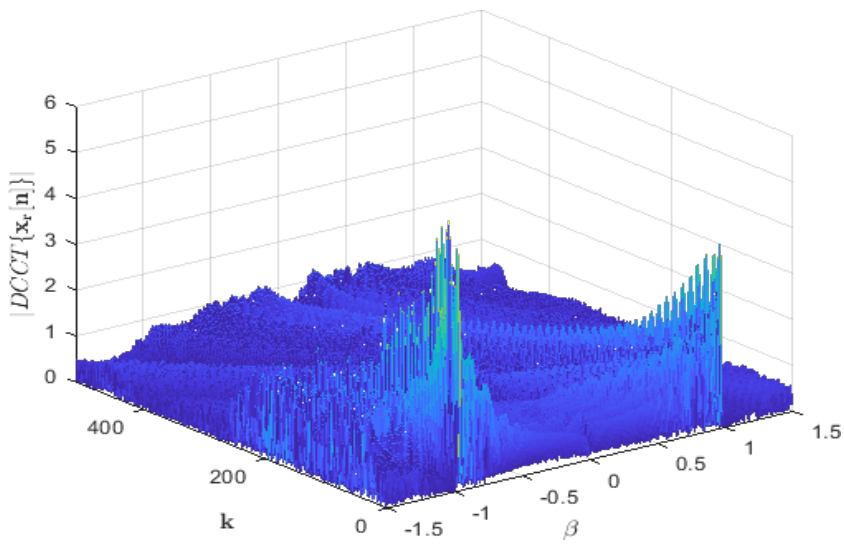

(a) Original DCCT coefficients.

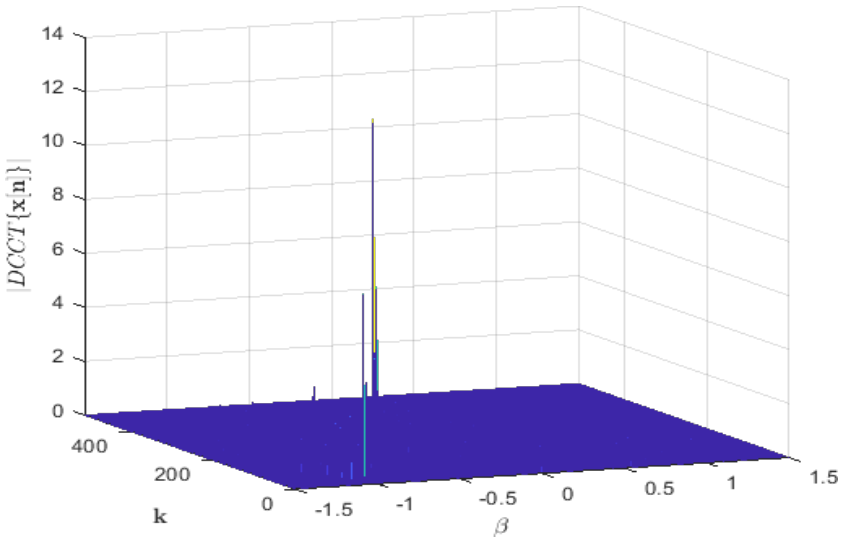

(b) Recovered DCCT coefficients with CS.

Figure 3.17: 3-D plot of DCCT coefficients of the reflected MCTDR signal occupying a bandwidth of $[0-50]$ MHz in complex Y-Network.

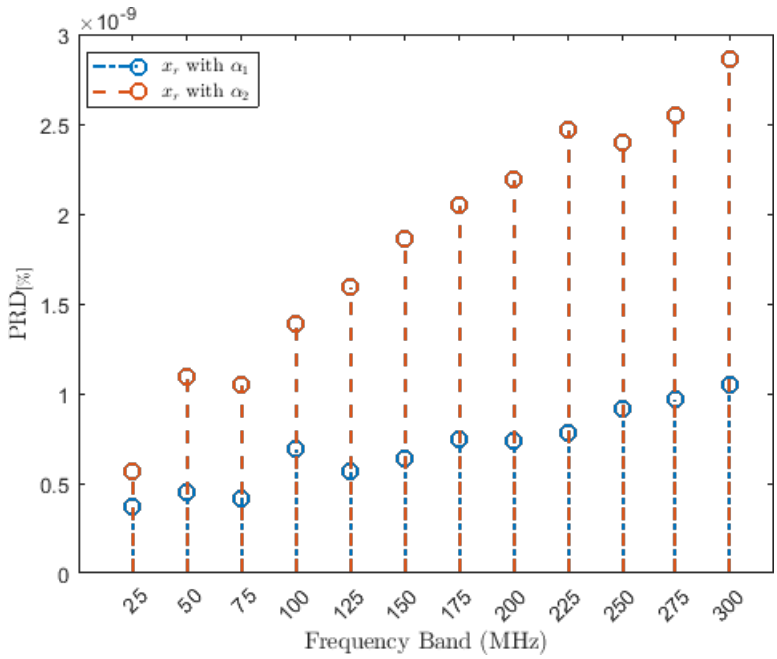

Figure 3.18: Reconstruction error as a function of signal bandwidth for different types of wires in a point-to-point network.

3.4 Conclusion

CS relies on sparseness condition of any signal to make possible the requirements on the sampling rate. Sparsity or compressibility reflects the fact that the information carried by a particular signal is much smaller than their bandwidth. Most signals are not sparse in the time domain, so linear transformations are used to make them sparse in specific equivalent basis. Therefore, in this chapter, we proposed two transformation bases for two different types of signals for reflectometry. First, we study on chirp signal, which is the most used in the FDR-based method. We propose the FrFT transformation that is a generalization of the classical Fourier Transform with an angle parameter α in the time-frequency plane.

Furthermore, we previously demonstrated that from the theoretically calculated optimal angle, the FrFT of chirp signal transforms into an impulse function; thus, a sparse representation of the signal. Moreover, as we consider that the defects of the wires are hard faults which cause a total reflection, hence all the study is applied to the injected signal. The simulation by the FrFT in a point-to-point or complex network with an acceptable attenuation shows good performances in terms of sparsity, computation time, resolution, and peak locations. However, the degree of sparsity increases while changing the electrical characteristics ($RLCG$) of the wire or the type of defects.

Not only FrFT is a complex transformation, but it is also applied to complex type signals. However, some applications require real transformations to provide better performances. Our second study is applied on real MC signal. We also introduce the DCCT and its inverse for which the kernel of the transformation is based on orthogonal real linear chirps. Since the error of the reconstructed signal by the regular DCCT is remarkable, we apply a new algorithm that combines CS and the DCCT. This proposed algorithm combines CS-DCCT and updates the least square solutions at every iteration. The proposed modification provides a precise peak at every exact location and correctly estimates the chirp signal parameters. Such adjustment allows to bypass the initial condition related to the injected signal; it also improves the reconstruction by decreasing both errors and the computational complexity. As a conclusion, not only we use the CS to break the Shannon-Nyquist constraint but at the same time to reduce the reconstruction errors. The next chapter introduces the analog CS idea in the context of reflectometry-based wire diagnosis systems.

CHAPTER 4

COMPRESSIVE SAMPLING FOR REFLECTOMETRY

4.1 Introduction

While dealing with hard faults, which result in significant reflections, reflectometry-based methods show good performances. However, soft faults, e.g., junctions within a network, characterized by a feeble reflection, produce echoes that can pass unnoticed compared to hard faults. On the other hand, the capacity to accurately detect the position of a fault along the NUT is a significant challenge. This property is directly related to the sampling frequency of the components. Unfortunately, nowadays, practically high-frequency DAC and ADC are physically limited. Moreover, from a commercial point marketing aspect, they become very expensive as either the resolution or the sampling frequency increases. The solution to overcome this situation was presented in chapter 2. CS is a technique that can efficiently acquire a signal using relatively few measurements so that a lower sampling frequency is utilized. There are several challenges to overcome while applying the CS-based wire diagnosis system. First, as detailed in chapter 3, according to the type of the injected signal, the reflected probe signal must be compressible or sparse in some basis. Provided that the reflectometry signals can have a sparse representation in a particular domain, their coefficients s can be recovered by solving equation (2.4). Second, there exists a delicate trade-off to optimize between the compression factor, in other word, the reduction in sampling rate, and the dynamic range of the compressive sampling.

However, in the current literature, an architectural combination between the AIC and the wire diagnosis systems does not exist. Thus, in this thesis, a sub-Nyquist approach, the RD of the AIC-based model architecture is used to determine the low-rate sampled measurement matrix Φ. This chapter aims to introduce a new architecture for reflectometry systems, allowing to inject high-frequency signals and bypass the mini-

mum rate required for sampling, which is followed by a determination on the choice of the components. The simulation results of this new approach are investigated for several networks. Notably, we analyze the performances and the impact of detecting the signature of different faults for different sampling frequencies. In parallel, the challenge between the compression factor and the ability of reconstruction with the optimization algorithm, OMP will be discussed. Meanwhile, this procedure will be followed by the introduction of an experimental setup intended to the practical validation of our proposed analytical model for both the AIC and reflectometry techniques.

4.2 Proposed system

CS and AIC have a great interest in reflectometry-based wire diagnosis systems, where high-frequency signals should be injected in order to improve the spatial resolution. Moreover, since the spatial resolution and the frequency are inversely proportional, the higher the frequency of the injected signal, the better the spatial resolution. Besides, the conditions of the sparsity for the reflectometry-based signals were detailed

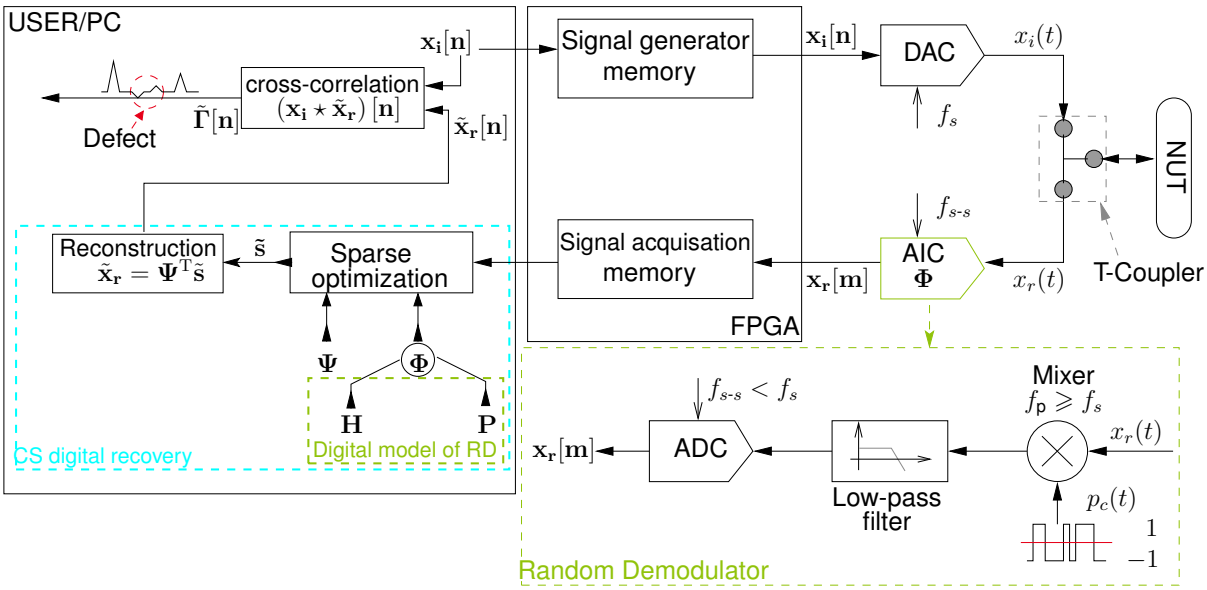

Figure 4.1: The proposed compressive sampling architecture of reflectometry with RD. Where in the digital model of RD, $\mathbf{P}$ represents the ± 1 values of PRBS and $\mathbf{H}$ represents the impulse response of the low-pass filter as well as the sub-sampling. Not that $\mathrm{m} \in \{1 \ldots \mathrm{M}\}$ and $\mathrm{n} \in \{1 \ldots \mathrm{N}\}$.

in Chapter 3. This consideration opens the opportunity to analyze the high-frequency reflectometry signals based on CS and AIC, where the actual limitations in the analysis can be overcome. To this aim, the first uniformly sampling RD AIC-based architecture is used to interpret the reflectometry-based systems signals. The new proposed low rate reflectometry based wire diagnosis architecture is presented in Figure 4.1. In this architecture, the high rate ADC is replaced by an AIC, where the sampling frequency of the ADC is $f_{s\text{-}s}$, with $f_{s\text{-}s} < f_s$. After all, in other words, at a given sampling frequency, the maximum frequency of the probe injected signal can be increased; hence, the spatial resolution. It offers the possibility to choose an ADC with a better resolution (i.e. number of bits), or it could be possible to keep the same sampling rate of a traditional ADC and exploit the compressive sampling to observe on high-frequency signals.

Furthermore, compared to the existing method in the literature working on the improvement of the spatial resolution, the proposed architecture is much easily implemented. For example, the time reversal method requires a Vector Network Analyzer which necessitates some calibration time, and it is hard to implement regarding its physical size. Moreover, the fake over-sampling, mostly used in the actual literature, request complex resynchronization mechanisms. Also, once a signature of a fault is detected, it requires a stable system for a given amount of time in order to finalize the recomposition procedure.

In our study, the analog front-end of the AIC is realized by the RD. This subsampling methodology is typically decomposed into three steps: modulation, filtering, and uniform sampling.

- **The mixer:**

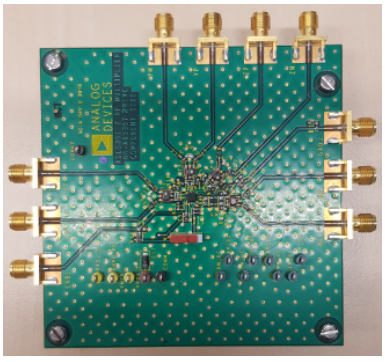

Figure 4.2: The Mixer ADL5391 [91].

The mixing process of the proposed AIC prototype is carried out by means of Analog Device ADL5391 evaluating board, where the bandwidth is about 2 GHz.

●The filtering:

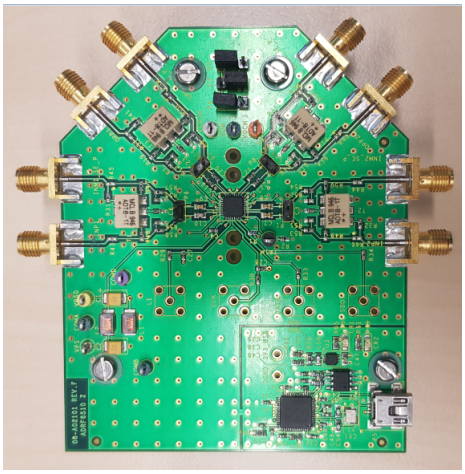

Figure 4.3: The low-pass filter ADRF6510 [92].

Then, the mixed signal is low-pass filtered by an Analog Device ADRF6510 evaluation board. The ADRF6510 is a dual-channel programmable six order Butterworth [1] low-pass filter, with selectable cut-off frequencies between $[1-30]$ MHz.

●The uniform sub-sampling:

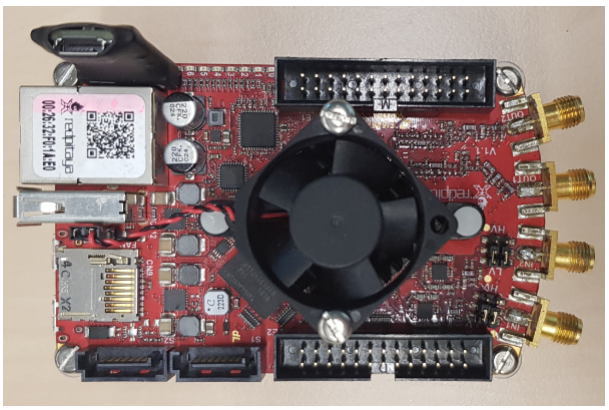

Figure 4.4: The FPGA board: Red Pitaya.

[1] A Butterworth filter is a linear filter, characterized to have a gain as constant as possible in its bandwidth. The generalized frequency response equation representing a nth order of Butterworth filter is given as: $|\mathrm{H}(j\omega)| = \frac{1}{\sqrt{1+(\omega/\omega_c)^{2n}}}$, where $\omega_c = 2\pi f_c$ is the cut-off frequency at -3 dB.

The sampling factor CF, which alternatively defines the sampling frequency of ADC, will be set to 1, 2, or 4. To check the feasibility of the proposed technique for practical implementation, the ideal goal is to generate the input signal with the FPGA board: Red Pitaya (mostly used in the laboratory) driving a 10-bit DAC with a maximum sampling rate of 125 MS/s and a 10-bit ADC where the frequency will vary. However, in order to be more accurate, the results of our experiments are based on a more reliable architecture, where the input signal and the Pseudo-Random Bit Sequence is generated by MATLAB and downloaded to a Tektronix AWG7122C Arbitrary Waveform Generator. In this case, the sub-sampling of the signal is accomplished by the software before the reconstruction phase.

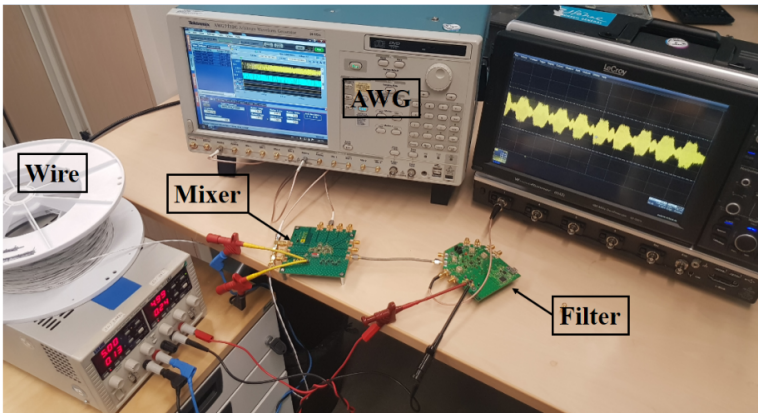

(a) With AWG7122C.

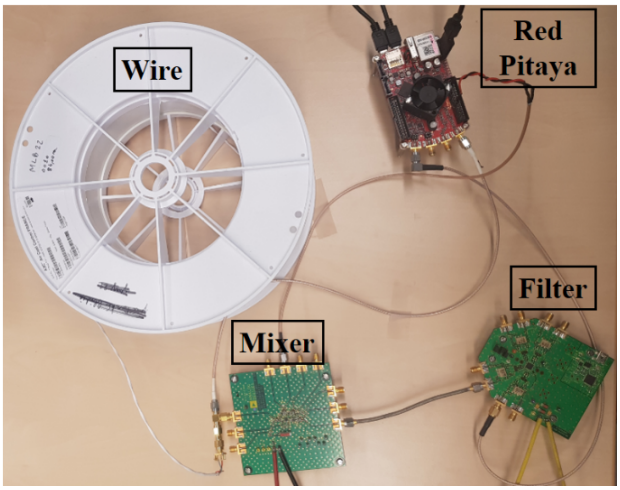

(b) With Red Pitaya.

Figure 4.5: Schema-bloc of the implemented reflectometry architecture.

Additionally, besides the identification of the sparseness matrix, the reconstruction algorithm is heavily dependent on the determination of the measurement matrix $\mathbf{\Psi}$ from the actual components used to realize the RD. Through equation (2.13), we can notice that $\mathbf{\Psi}$ is related to the PRBS and the impulse response of the anti-aliasing low-pass filter. Since the random sequence is already controlled, only the estimation of the impulse response of the anti-aliasing filter is necessary. The concept of validation by simulation is based on using the Butterworth model low-pass filter proposed by MATLAB.

4.3 Standard reflectometry-based system for wire diagnosis

We have investigated two representative sets of networks: a single cable and a single junction structure. The analysis shows that due to multiple reflections, the interpretation of a complex network reflectogram is complicated compared to that of a simple cable. Moreover, the difficulties of analysis of complex wired networks will be studied in the elementary case of the Y network. As for the type of injected signal, we mainly work on MC signals, such as chirp and MCTDR as detailed in Chapter 1. The analysis of the networks will be performed by the time domain reflectometry in which the detection of the defect will be driven by the shape of the peaks appeared in reflectogram.

4.3.1 Point-to-point wire diagnosis

To ensure our method on a simple case, we evaluate the detection of hard defects (open and short circuits) at the extremity of the wire. At some point, a point-to-point wire is easily interpreted compared to a complex network in which multiple reflections have occurred. We test a wire of 100 m length assigned a hard fault at its extremity. The characteristic impedance Z_c of the line is equal to $73\,\Omega$. The computed reflectogram is obtained by the correlation between the reflected and the incident waves (chirp), where the signal occupies a bandwidth $B = 50$ MHz, and the number of samples is $\mathrm{N} = 1024$. A positive amplitude indicates an impedance discontinuity with an module greater than Z_c (Figure 4.6a), whereas a negative amplitude indicates a module impedance discontinuity lower than the characteristic impedance (Figure 4.6b). In this case of Network,

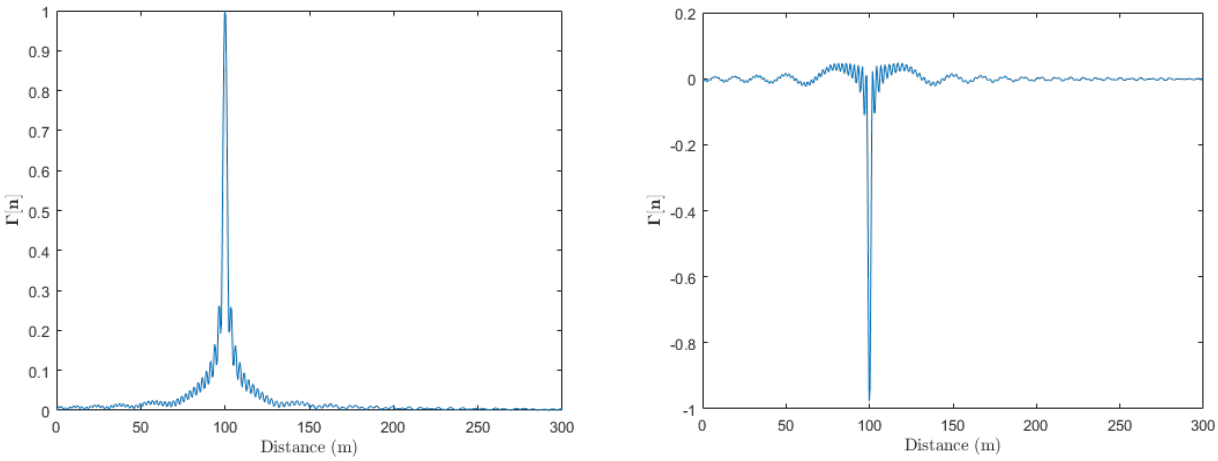

(a) Open circuit. (b) Short circuit.

Figure 4.6: The normalized reflectogram corresponding to high sampling frequency $f_s = f_{Nyq} = 2B$ for a point-to-point system, while the injected signal chirp occupies a bandwidth $B = 50$ MHz.

despite the presence of secondary lobes around the peak, it is easy to detect and locate the open circuit. Moreover, as represented in Figure 4.7, we show the importance of improvement of spatial resolution by increasing the maximum frequency of the injected signal. Accordingly, an improvement in the precision of the fault localization and a high spatial resolution is obtained.

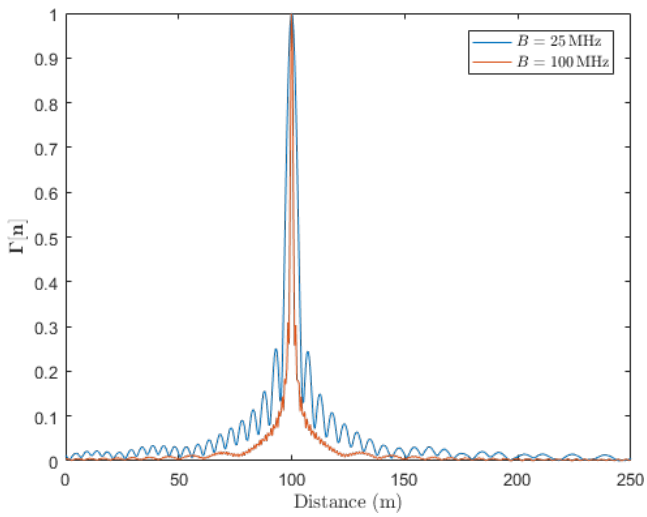

Figure 4.7: Influence of the maximum signal frequency on the accuracy of the fault localization.

4.3.2 Diagnosis of the state of a Y complex network

The detection of the defects becomes more challenging with the complexity of the wired network because of multiple reflections' presence. Thereby, we take an example of a complex network with one junction. The existing Y-branch network with a characteristic impedance $Z_c = 50\,\Omega$ consists of three branches. This complex network has a junction connecting the two lines, $\mathbf{B2}$ and $\mathbf{B3}$ to the first one $\mathbf{B1}$. Each of the branches $\mathbf{B1}$, $\mathbf{B2}$, and $\mathbf{B3}$ have a respective length of $l_1 = 24\,$m, $l_2 = 18\,$m and $l_3 = 32\,$m. The lines $\mathbf{B2}$ and $\mathbf{B3}$ end with an open circuit. Figure 4.8 shows the Bounce diagram representing the different reflections in the network.

The injected chirp signal will propagate along the line $\mathbf{B1}$ until it encounters the impedance discontinuity at the junction. One-third of the signal energy is reflected back to the injection point. On the other hand, due to the existence of the junction, the transmitted part of the signal is equally divided to propagate in the lines $\mathbf{B2}$ and $\mathbf{B3}$. While the signal propagates on the line, any impedance mismatches will cause a reflection. In our case, once the signal reaches the open-circuit at the end of the lines $\mathbf{B2}$ and $\mathbf{B3}$, it will be reflected. Then, reflected signals propagate back to the junction. Finally, they get divided respectively at the junction to propagate again into the three lines $\mathbf{B1}$, $\mathbf{B2}$, and $\mathbf{B3}$ and so on until the total attenuation of the signal.

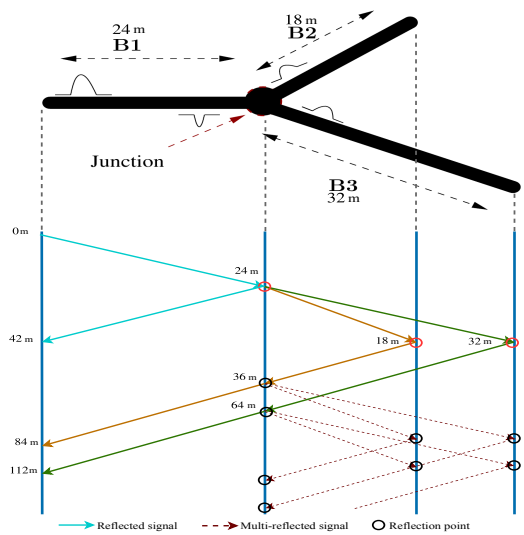

Figure 4.8: Bounce layout of the NUT considered, with a characteristic impedance $Z_c = 50\,\Omega$. The three lines $[\mathbf{B1}, \mathbf{B2}, \mathbf{B3}]$ are of respective length $[24,18,32]$ meters, where the extremity of $\mathbf{B2}$ and $\mathbf{B3}$ is charged by $Z_l \gg Z_c$.

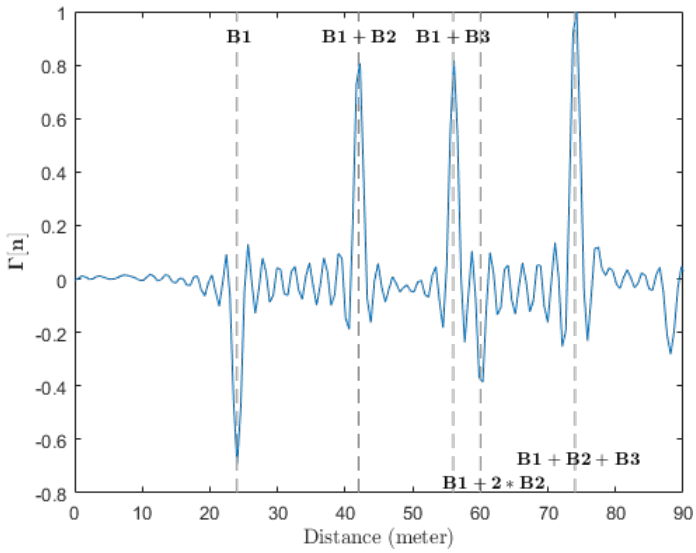

Figure 4.9: The normalized reflectogram corresponding to high sampling frequency $f_s = f_{Nyq} = 2B$ for a Y-network system, while the injected signal chirp occupies a bandwidth $B = 50$ MHz.

Therefore, the expected reflections are at $[24, 18, 32]$ meters which represent the impedance mismatching on the junction, $\mathbf{B1}$, at the end of $\mathbf{B2}$ and $\mathbf{B3}$, respectively. Besides, multiple reflections are also detectable. Hence, the reflected signals traveling path $[\mathbf{B1} + 2 \times \mathbf{B2}, \mathbf{B1} + \mathbf{B2} + \mathbf{B3}, \cdots]$ accounts for the reflection peaks at $[60, 74, \cdots]$ meters respectively. We note that for the detection of defects, we are mainly interested in primary echoes which directly give information about the distance and the nature of the singularity. As for secondary echoes, they are difficult to control and in some cases constitute a disturbance.

Figure 4.9 represents the corresponding normalized reflectogram, where each peak is associated to each discontinuity along the cables of the network. The first peak at 24 m corresponds to the junction, the second peak at 42 m ($\mathbf{B1} + \mathbf{B2}$) corresponds to the open circuit at the end of the branch $\mathbf{B2}$, and the third peak at 56 m ($\mathbf{B1} + \mathbf{B3}$) corresponds to the open circuit at the end of the branch $\mathbf{B3}$.

Although it is possible to distinguish the defects (open circuit), the presence of side lobes around each peak remains troublesome. Another key point is to achieve a sufficient accuracy to efficiently distinguish two close defects. For instance, we consider again the Y-network with three lines $[\mathbf{B1}, \mathbf{B2}, \mathbf{B3}]$ of respective length $[24, 18, 21]$ meters, respectively. The expected peaks corresponding to the junction and the two open circuits present at the ends of $\mathbf{B2}$ and $\mathbf{B3}$ are at the distances 24 m, 18 m, and 21 m re-

spectively. However, for a testing chirp signal of $f_{max} = 25$ MHz, the defects of the lines $\mathbf{B2}$ and $\mathbf{B3}$ overlap. Augmentation of the f_{max} to 50 MHz allows to localize the three corresponding faults peaks; hence an improvement of the spatial resolution. Thereby, to deal with this problem on complexity of hardware implementation without affecting the actual reflectometry architecture, we are going to introduce in the section below a detailed study on the possibility of the compression (sub-sampling) and the improvement of the spatial resolution simultaneously.

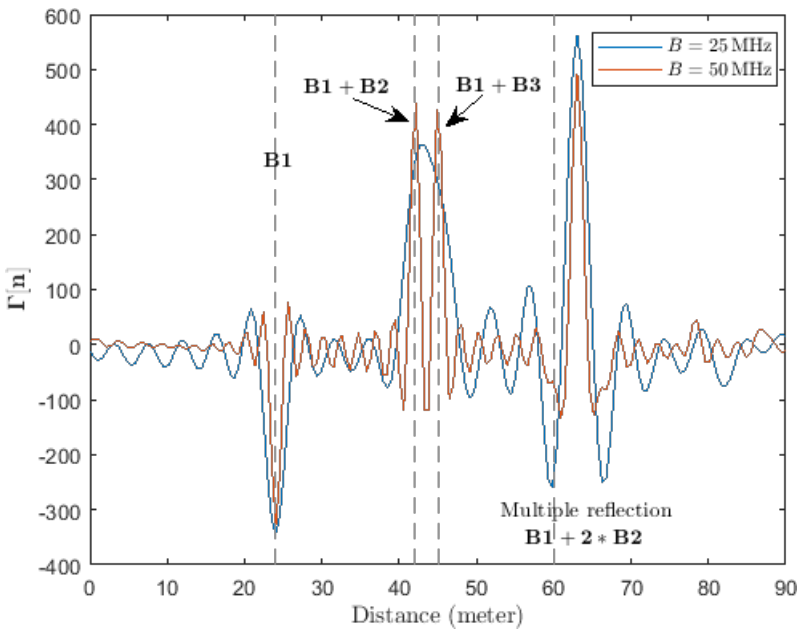

Figure 4.10: The reflectogram for the chirp signal occupying a bandwidth of $B = [25, 50]$ MHz, where the influence of the maximum frequency of the injected signal on the detection and localization two nearby faults is represented.

4.4 Implementation of CS methods for reflectometry-based system for wire diagnosis

In the following section, the performance of different aspects of the application of CS mathematic methods on acquisition hardware for monitoring the wire diagnosis is presented. The first part of this section will be devoted to provide the numerical support that will prove the efficiency of CS in locating multiple faults in point-to-point and complex wiring configurations. In fact, these numerical results will handle high-frequency

chirp and MCTDR signals while using standard traditional ADC. Notably, in this case, the influence of data reduction, under-sampling, and the impact of noise are presented. After that, an experimental study will be conducted in order to validate the method and highlight its feasibility for real-life practical implementation.

4.4.1 Impact of detection and localization for point-to-point wire

Dealing with the proposed point-to-point network structure in section 4.3.1, we use the AIC based prototype and evaluate the reconstructed signal and especially the position of the defect compared to the standard reflectometry systems. In simulation tests, to asses the performances and limitations of the CS, the frequency of the injected signal is kept constant while only the compression factor (CF) is changed. Indeed, with the increase of the CF, the number of points used to reconstruct the signal in question decreases and the additional noise on these points prevent the convergence of the reconstruction algorithms.

Accordingly, lets consider as a testing signal a chirp and an MCTDR signals occupying a bandwidth $B = 50$ MHz with a frequency resolution of $\Delta f = 50\,\text{MHz}/1024 = 48.8$ KHz. Considering an ADC, a sampling frequency of at least $f_s = 100$ MSa/s is required for the reflected signal. With this sampling rate, records of 1024 samples can be acquired. The architectural combination of the reflectometry system and the AIC, where the high frequency ADC is replaced by different steps of RD, allows sampling the reflected signal $x_r(t)$ below the required sampling frequency. We studied the system for different sub-sampling frequency, $f_{s\text{-}s} = f_s/\mathbf{K}$ where $\mathbf{K}$ is an integer greater than 1 and can be equal to $\mathbf{K} = [2, \cdots, 16]$. The relation between the compression factor and $\mathbf{K}$ is determined as:

$$\mathbf{K} = \frac{\text{CF}}{R} \quad \text{where} \quad \begin{cases} \text{CF} = \frac{\mathrm{N}}{\mathrm{M}}, \\ \mathrm{N} = \text{number of samples with respect to Nyquist,} \\ \mathrm{M} = \text{number of samples with compression,} \\ R = \text{ratio between the sampling and the simulation frequency.} \end{cases} \tag{4.1}$$

Thus, in the AIC case system, the output of the acquisition record length is shorter due to the compressive sampling. It can be seen that records of M samples are enough to allow the correct spectrum reconstruction of the considered signal. Figure 4.11a and

4.12a show the reconstruction of the sub-sampled reflected signal of length $\mathrm{M} = 64$ instead of $\mathrm{N} = 1024$ for a sampling frequency corresponding to $f_{s\text{-}s} = f_s/\mathbf{K} = 12.5$ MHz ($\mathbf{K} = 8$). With the help of the OMP optimization algorithm, the sub-sampled reflected chirp and MCTDR signals are reconstructed. In order to have a good conversion, first, we define for both signals the measurement matrix by RD and second the sparseness matrix. This latter, for the chirp signal, is related to the injected signal characteristics and defined by the FrFT with a corresponding optimal angle; as highlighted in Chapter 3, the matrix $\mathbf{\Psi}$ should be equal to $\mathcal{F}^{-1.55}$. Whereas, for the MCTDR signal, $\mathbf{\Psi}$ matrix is defined as $\mathbf{\Psi} =$ CS-IDCCT, which is totally independent and does not require any initial condition. The resulting SNR $= 6$ dB for the reconstructed reflected MCTDR signal decreases compared to the SNR $= 7.83$ dB of the reconstructed reflected chirp signal, yet both cases are robust for the detection of the defect on the wire. Moreover, as illustrated in Figure 4.11b and 4.12b and despite the presence of the secondary lobes for $f_{s\text{-}s} = f_{Nyq}/8$, we can reconstruct and measure the distance of the defect located in this simulation at 100 m from the point of injection, which is fundamental for reflectometry. Furthermore, the robustness of the reflectogram and more significantly the robustness to the noise is a primary prerequisite to consider since the diagnosis system can be disturbed either by the useful signals of the target system itself or by parasitic sources. Therefore, we have to assess the quality of the reconstructed signal via some metrics. SNR is appropriate to measure the difference between the original and the reconstructed signal. Yet, Signal to Noise and Distortion (SINAD) is interesting since in reflectometry we are mostly interested by peaks. Besides, calculating deconvolution (e.g. CLEAN algorithm [1]) between the two signals would also give interesting information. Based on IEEE Std. 1241.2010 [93], the SINAD is the ratio of the peak amplitude representing the defect to the mean value of the root sum square of all other components, including the artifacts (harmonics) and the noise. SINAD is a good indication of the overall dynamic performance of the proposed CS-reflectogram system. The SINAD is expressed in decibels (dB) and determined by the following equation:

$$\text{SINAD} = 20\log\left(\frac{|\text{Amplitude of the peak}|}{\sqrt{\frac{1}{\mathrm{N}}}\,(\text{Noise + Harmonics})}\right), \tag{4.2}$$

where N is the number of samples.

Therefore, first, we study the accuracy of the reconstruction for various SNR and different sampling frequencies. Note that the SNR values are sensitive to the sampling

frequency and are calculated as in equation (2.10). Figures 4.11c and 4.12c show the SNR values for different types of reflected signals (noise-free, low-noise: SNR$=20$ dB and very noisy: SNR$=10$ dB) with various sampling frequencies (far from the Nyquist frequency). In this study, we apply a number of 100 data set based on the Monte Carlo method, and these results are consistent with the theory of CS because the performance of the algorithm degrades for noisy signals. When the sampling frequency is much lower than that of Nyquist, the reconstruction algorithm does not have enough information to reconstruct the original signal, which results in a degradation of the SNR.

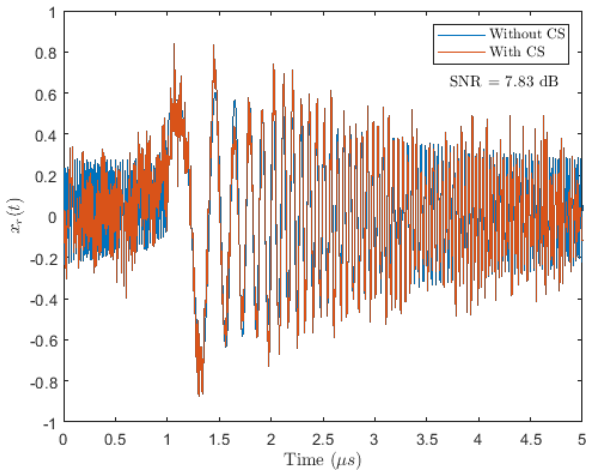

(a) Reflected and reconstructed sub-sampled signal.

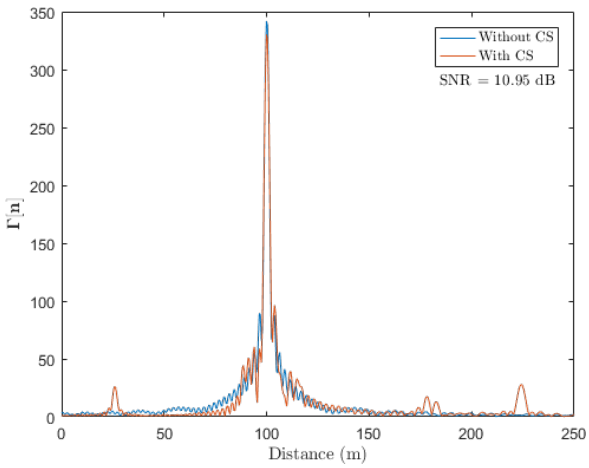

(b) Reflectograms, in red (with CS) corresponding to low sampling frequency $f_{s\text{-}s} = \frac{f_s}{8}$ and in blue (without CS) corresponding to high sampling frequency $f_s = f_{Nyq} = 2B$.

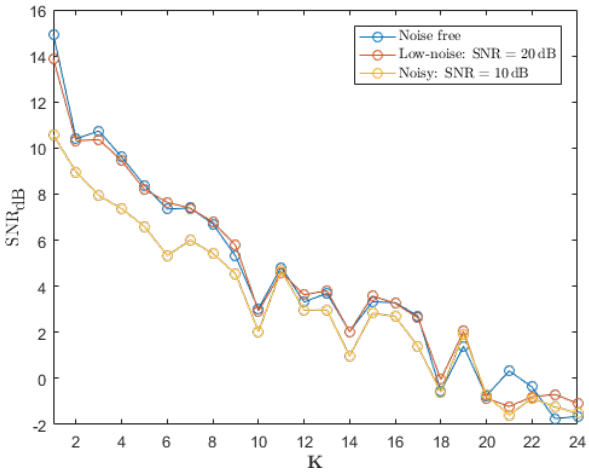

(c) Effect of noise and sampling frequency on the performance of the reflectogram's reconstruction measured by SNR.

Figure 4.11: A study on a chirp signal with a bandwidth $B = 50$ MHz for a sampling frequency $f_{\mathrm{s-s}} = f_s/8 = 12.5$ MHz.

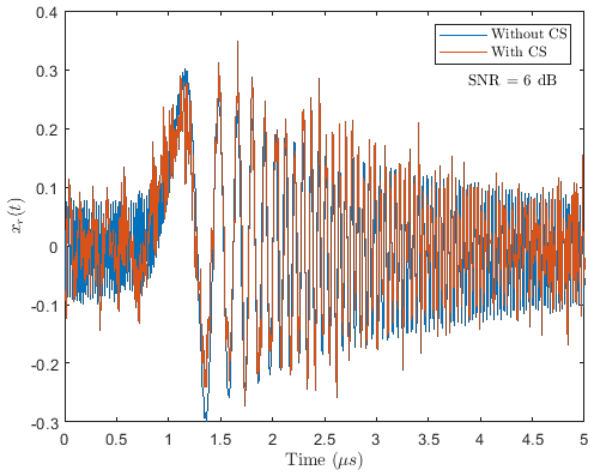

(a) Reflected and reconstructed sub-sampled signal.

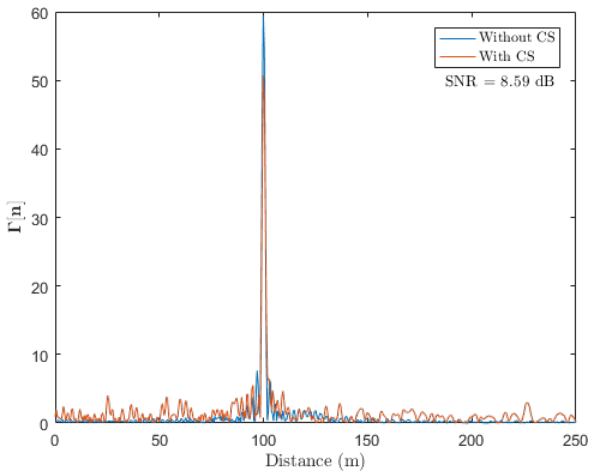

(b) Reflectograms, in red (with CS) corresponding to low sampling frequency $f_{s\text{-}s} = \frac{f_s}{8}$ and in blue (without CS) corresponding to high sampling frequency $f_s = f_{Nyq} = 2B$.

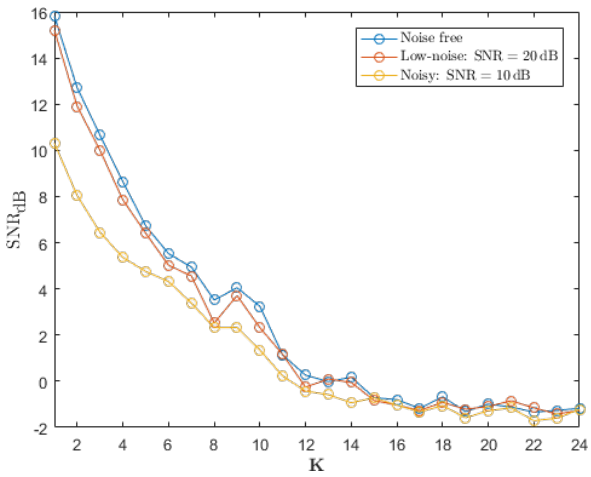

(c) Effect of noise and sampling frequency on the performance of the reflectogram's reconstruction measured by SNR.

Figure 4.12: A study on an MCTDR signal with a bandwidth $B = 50$ MHz for a sampling frequency $f_{\mathrm{s-s}} = f_s/8 = 12.5$ MHz.

Second, as shown by the simulation results, the level of both the noise floor and harmonics increases with the decrease of the sampling frequency; hence, a decrease in the value of SINAD. In fact, this is probably due to the fact that a smaller amount of information passes through the filter and the ADC which can be used for the reconstruction. This can be easily observed in Figure 4.13, where the robustness of the system is studied, by taking in consideration the SINAD versus the sampling frequency of the ADC for chirp and MCTDR signals of bandwidth $B = 50$ MHz. Obviously, the SINAD has better performance for a higher sampling frequency. For example, for chirp signal, when the compression factor is equal to 8 ($f_{\text{s-s}} = f_s/8 = 12.5$ MHz) the SINAD $= 28.29$ dB which is almost constant compared to a standard reflectometry for $f_s = 100$ MHz the SINAD $= 29.49$ dB.

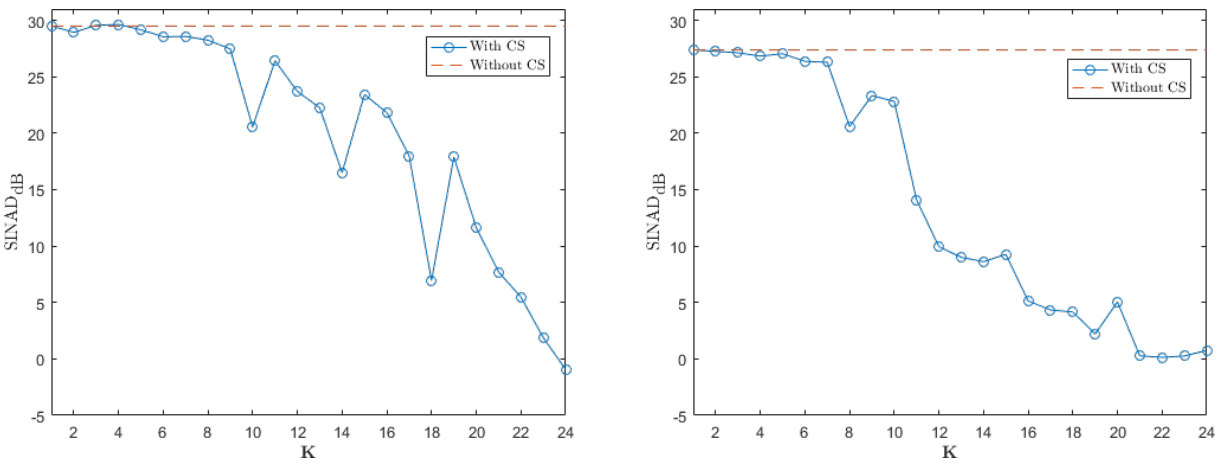

(a) Chirp signal of bandwidth $B = 50$ MHz. (b) MCTDR signal of bandwidth $B = 50$ MHz.

Figure 4.13: The robustness of the fault localization with sampling frequency on the performance of the reflectogram's by evaluating the SINAD.

4.4.2 Impact of detection and localization for complex wire

In this section, the feasibility of CS on more complex networks. As in previous section, we use the single-junction network of Figure 4.8. In simulation tests, we apply two various but complementary axes. The first axis is based on interpretation of the reconstructed reflectogram for different compression factor while keeping the maximum frequency of the injected signal constant; hence, the limitation of CS is treated. The second axis relies on the analysis to carry out the RD architecture functionality as the

wide-band of the acquired signal increases without the need of a wide-band ADC; and therefore an evaluation on the spatial resolution of the system.

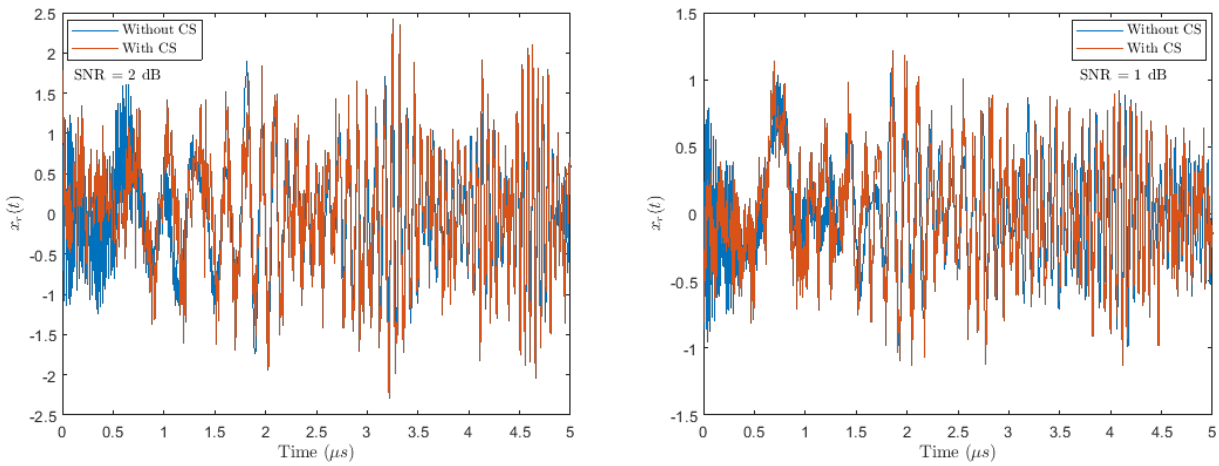

(a) Chirp signal of bandwidth $B = 50$ MHz. (b) MCTDR signal of bandwidth $B = 50$ MHz.

Figure 4.14: Reflected and reconstructed of sub-sampled signal with OMP at $f_{\text{Nyq}}/8$.

During the simulation, both the MC chirp and MCTDR signals have been generated with frequency within the range of $[0\text{-}50]$ MHz and with a record length of $\mathrm{N} = 2048$ samples. Part of the injected signal is reflected towards the injection point when it encounters a discontinuity during its propagation. This latter is then given to a mixer model, with a PN sequence of the same size. The output of the mixer is then given to a low-pass filter, modeling the antialiasing filter, with a cut-off frequency depending on the sampling rate. This system allows to sample the reflected signal $x_r(t)$ below the required sampling frequency. Due to downsampling, the record length is reduced. For compression factors $\mathbf{K} = [2, 4, 8, \cdots, 16]$ the length is reduced to $\mathrm{M} = [1024, 512, 256, \cdots, 128]$ respectively. The output of the ADC model is provided to the reconstruction OMP algorithm [54, 94], capable of regenerating the original reflected signal of size $\mathrm{N} = 2048$. Figure 4.14 shows the reconstruction of the sub-sampled reflected signal for chirp and MCTDR with a factor $\mathbf{K} = 8$ ($\mathrm{M} = 256$ samples) that has an SNR $= 2$ dB and SNR $= 1$ dB, respectively. Compared with the previous simple case wire, the reconstructed signals have a higher SNR, however it will maintain the identification and detection of the peaks.

In order to determine the defect on the Y-NUT of Figure 4.8, the cross-correlation is calculated between the injected and the reconstructed reflected signals. The injected signal into the network propagates at a speed relative to 0.66 times to the speed of

light. The wave propagates until it encounters the first junction at a distance of 24 m from the testing port. Consequently, the discontinuity reflects $|1/3|$ the energy of the wave to the source and the remaining $|2/3|$ of it on each branch. The first reflection reaches the origin after $0.21\,\mu$s, which is the round-trip time to reach the junction. As for the other part of the wave, it will be transmitted through the network, where part of it will propagate into the second branch until it reaches the open load located at 42 m from the reference port and then reflects back until it attenuates utterly due to the attenuation of the network. Similarly, the reflecting-transmitting process will take place into the third branch, for the part propagating the third branch load located at 56 m from the reference port. As we notice in Figure 4.15, the simulation results for a compression factor equal to 8 maintains a precise localization as well as an amplitude for different peaks of the reflections with an SNR between low and high rate sampling frequency reflectograms is equal to 5.48 dB for chirp signal and 2.45 dB for MCTDR signal.

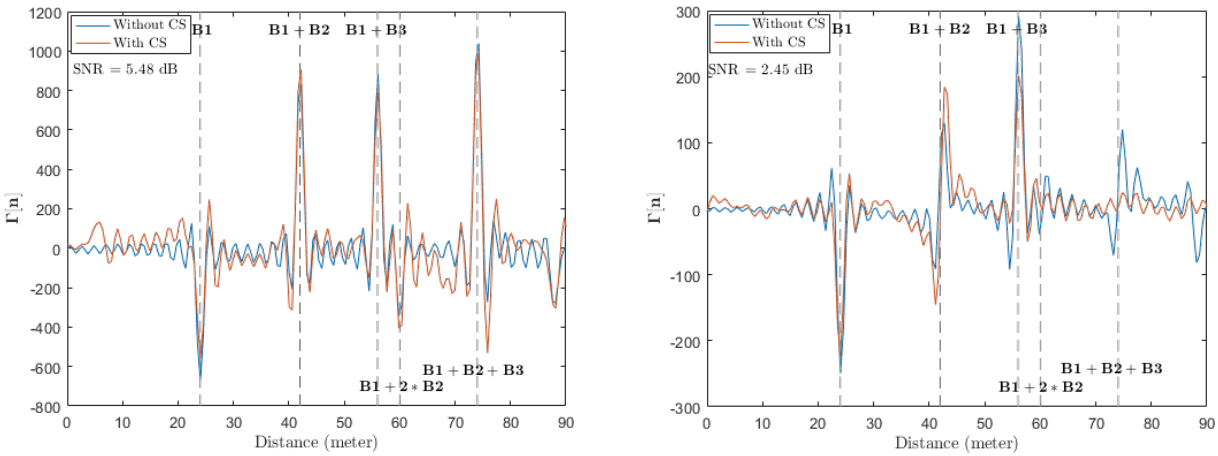

(a) Chirp signal of bandwidth $B = 50$ MHz.

(b) MCTDR signal of bandwidth $B = 50$ MHz.

Figure 4.15: Reflectograms, in red (with CS) corresponding to low sampling frequency $f_{s\text{-}s} = f_{\text{Nyq}}/8$ and high in blue (without CS) corresponding to high sampling frequency $f_{s\text{-}s} = f_{\text{Nyq}} = 2B$.

However, the selection of the compression factor has an impact on the performance, when $\mathbf{K}$ is much higher than the required length of the reconstructed signal, the algorithm will not have enough information to reconstruct the demanded signal. First, to discuss the impact of $\mathbf{K}$ on the performances, we establish a simulation for different

compression factors, and we calculate the relative errors $\delta\alpha_r$.

$$\delta\alpha_r = \frac{d_{\text{CS}} - d_{\text{th}}}{|d_{\text{th}}|}, \tag{4.3}$$

where d_{CS} is the distance of the peak found after compression and d_{th} represents the distance of the peak theoretically. The results are shown in Table 4.1, the $\delta\alpha_r$, as defined in equation (4.3), is the error between the distance of the defect calculated with the proposed architecture and the actual one. In those simulations, the same sequence of PN is applied for different compression factors in order to reconstruct the signal having the length of $\mathrm{N} = 512$; later, a correlation is applied for the localization of the defect. We note that for the compression factor 10 the localization of defects is acceptable, below that the defects are invisible (e.g., for $f_{\text{Nyq}}/12$ the defect at $\mathbf{B2}$ and $\mathbf{B3}$ is missed). This limitation can be solved by increasing the length-N of the signal so that we can increase the compression factor of the ADC.

Table 4.1: The SNR_{dB} for different compression factors and the relative errors $\delta\alpha_r$ of localization of defects at each point.

	$\text{SNR}_{[\text{dB}]}$	$\delta\alpha_r\mathbf{B1}$	$\delta\alpha_r\mathbf{B2}$	$\delta\alpha_r\mathbf{B3}$
f_{Nyq}	30.25	0.021	0.018	0.008
$f_{\text{Nyq}}/2$	7.35	0.021	0.018	0.008
$f_{\text{Nyq}}/4$	8.69	0.021	0.018	0.008
$f_{\text{Nyq}}/8$	6.13	0.021	0.018	0.008
$f_{\text{Nyq}}/10$	4.49	0.021	0.018	0.008
$f_{\text{Nyq}}/12$	1.2	0.021	None	None
$f_{\text{Nyq}}/16$	1.78	0.021	None	None

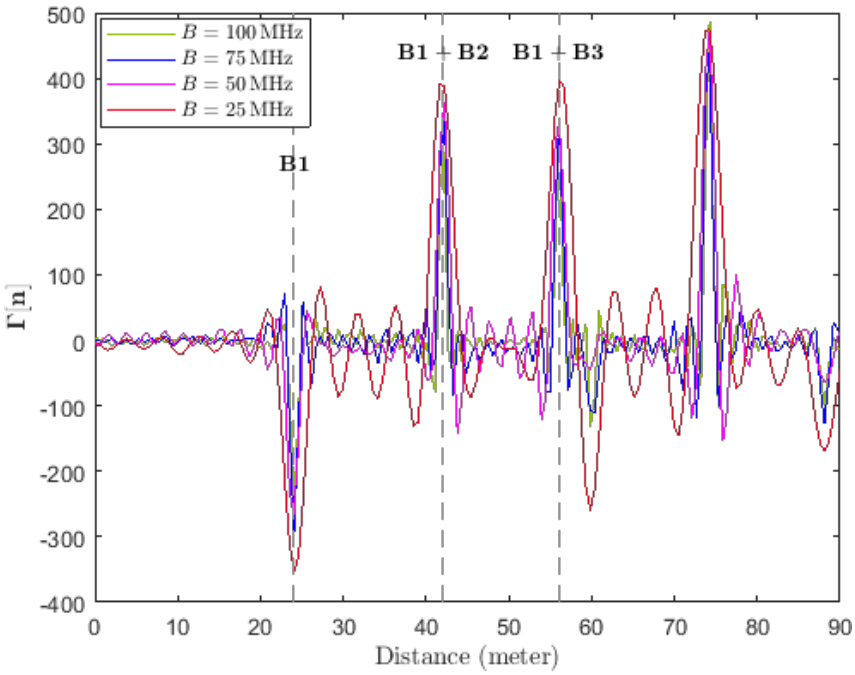

(a) Reflectogram for chirp signal.

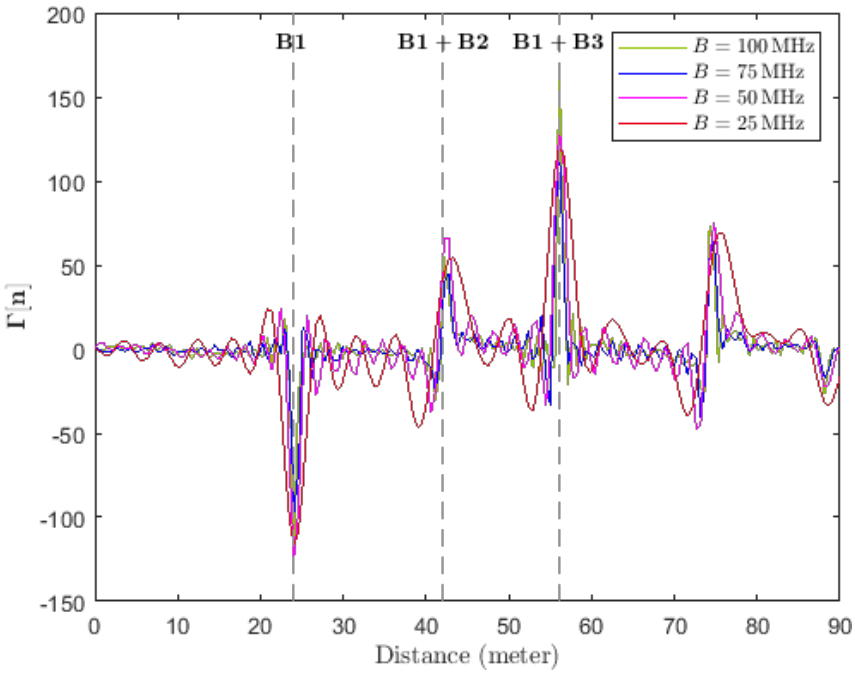

(b) Reflectogram for MCTDR signal.

Figure 4.16: Reconstructed reflectogram for four different bandwidths of injected signal where the sampling frequency is constant $f_{s\text{-}s} = 50$ MHz for the Y-network of branches length $[24, 18, 32]$ m.

Let's now introduce the CS impact by varying the injected signal bandwidth B while keeping the sampling frequency of a traditional ADC constant. Such a study at one point will help to observe the importance of improving the spatial resolution of the reflectogram and in another point will offer to keep the same old reflectometry hardware. This study is based on the average of 50 trials of Monte Carlo analysis and the sampling frequency of ADC embedded in the AIC architecture is maintained constant to $f_s = 50$ MHz. The injected chirp/MCTDR signal occupies a bandwidth $B = [25, 50, 75, 100]$ MHz, therefore the compression factor is $\mathbf{K} = [1, 2, 3, 4]$ respectively. In these cases, the under-sampled modified reflected signals are of size $\mathrm{M} = 256$ and are given to the reconstruction algorithm so that the original reconstructed signals of size $\mathrm{N} = 1024$ are regenerated. As we can notice in Figure 4.16, the peaks corresponding to defects become sharper, hence more accurate when the bandwidth occupied by the injected signal is higher. Thus, it results in an improvement of the spatial resolution of the signal.

Moreover, in order to efficiently detect an accurate localization of the defect, a post-processing algorithm can be applied. Notably, it is obvious to notice that in the proposed network, the branches lengths ($\mathbf{B2}$ and $\mathbf{B3}$) are sufficiently determined such that the high reflections caused on the extremities will not interfere. Therefore, it contributes to clear identification of defects. However, would it be possible to characterize the defects on approximately similar length branches?

To answer this question, we will reconsider the Y-network of three lines $[\mathbf{B1}, \mathbf{B2}, \mathbf{B3}]$ are of respective length $[24, 18, 21]$ m. Unfortunately, the reflections at the end of $\mathbf{B2}$ and $\mathbf{B3}$ are delayed only by 30 ns ($d = 6$ m). However, for the injected signal occupying a bandwidth $B = [25, 50, 75, 100]$ MHz the spatial resolution will vary $\delta_s = [8, 4, 2.6, 2]$ m. We represent in Figure 4.17, the reconstructed reflectograms for four different bandwidth of injected signal where the sampling frequency is maintained constant $f_{s\text{-}s} = 50$ MHz; hence, we remain the same hardware. As we notice, regardless of the fact that we are respecting the Nyquist criteria for $B = 25$ MHz, yet the defect at the extremity of $\mathbf{B3}$ is missed. In fact, this appears to be the same problem as that of any radar system, where the resolution or in another word the maximum frequency of the testing signal should be defined as that the radar system is capable of distinguishing between two nearby adjacent targets. Therefore, as illustrated in Figure 4.17, to deal with this problem, we consider the alternative high frequency injected signals for which the reflected signals are reconstructed by obeying a down-sampling. This analysis shows

that the concept of CS allows to enhance and clarify the signature of the fault and make it detectable.

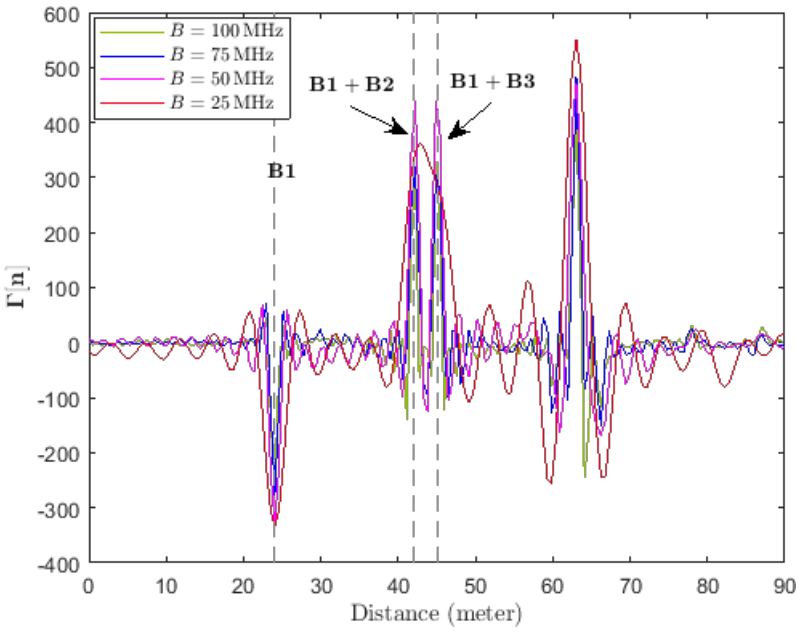

(a) Reflectogram for chirp signal.

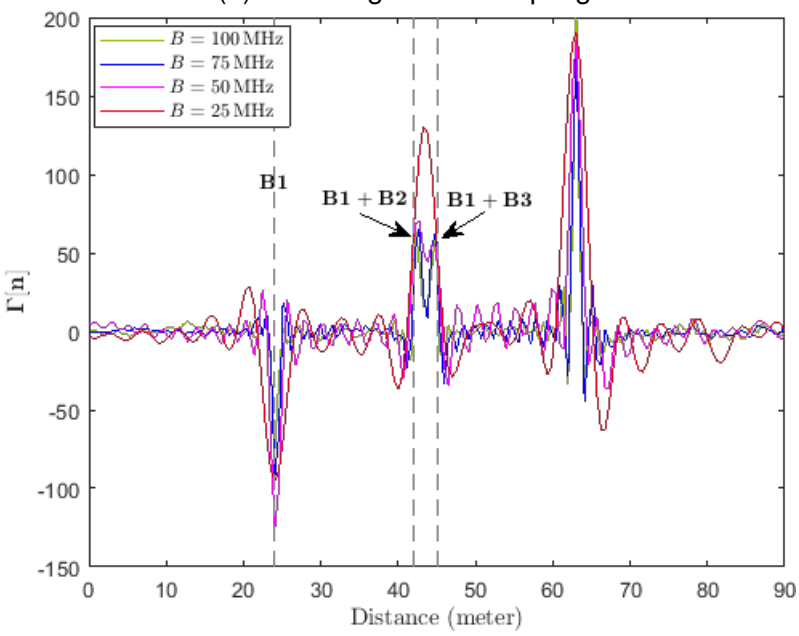

(b) Reflectogram for MCTDR signal.

Figure 4.17: Reconstructed reflectogram for four different bandwidths of injected signal where the sampling frequency is constant $f_{s\text{-}s} = 50$ MHz for the Y-network of branches length $[24, 18, 21]$ m.

4.5 Experimental results

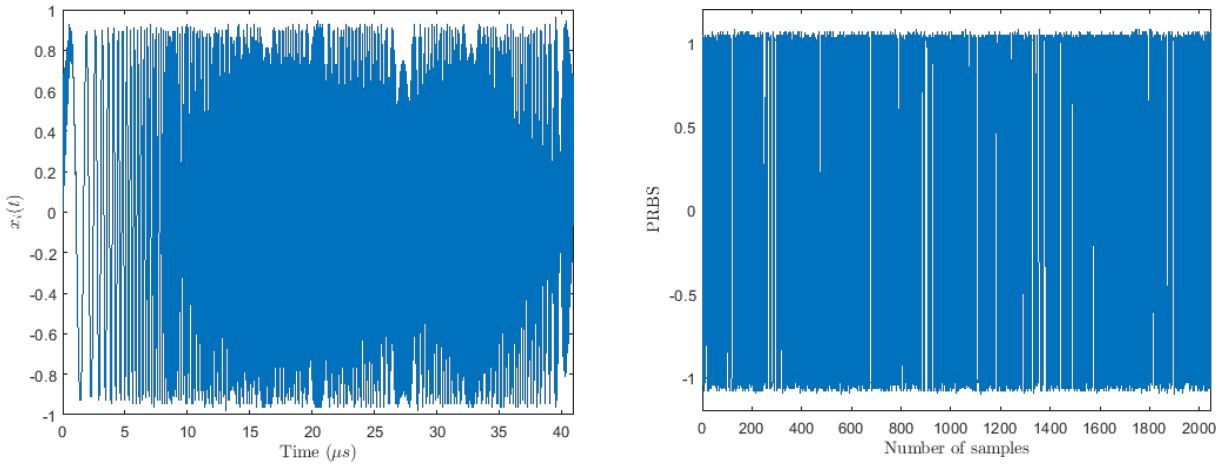

(a) MCTDR signal of bandwidth $B = 25$ MHz.

(b) PRBS signal.

Figure 4.18: The injected MCTDR and PRBS signals by the AWG.

To prove the capacity of the CS experimentally in precisely locating a hard fault, we apply it on a simple point-to-point 87 m long wire having electrical characteristics as follows:

$$\begin{aligned} R &= 4.637 \times 10^{-4}\,(\Omega/\text{m}), \\ L &= 3.8006582698 \times 10^{-7}\,(\text{Henry}/\text{m}), \\ C &= 1.23484257517 \times 10^{-10}\,(\text{Farad}/\text{m}), \\ G &= 4.02189721899 \times 10^{-11}\,(\text{Siemens}/\text{m}). \end{aligned} \tag{4.4}$$

While the AWG7122C functions at 50 MHz, its outputs are configured to generate the signal MCTDR occupying a bandwidth $B = [0 - 25]$ MHz and the PRBS a frequency of $f = 50$ MHz of size $\mathrm{N} = 2048$ samples. Figures 4.18a and 4.18b represent both the injected and PRBS signals. The reflected signal is then associated with three phases (modulation, filtering, sub-sampling) implied by the RD. Therefore, we will demonstrate those phases and try to compare them with the numerical approach.

First, both the reflected and PRBS signals are multiplied using the multiplier ADL5391. Figure 4.19 illustrates the measured and the numerical multiplied signals in blue and red, respectively. Since the SNR between them is equal to 15.3 dB, thus the noise added by the multiplier should not disturb the convergence of the OMP algorithm.

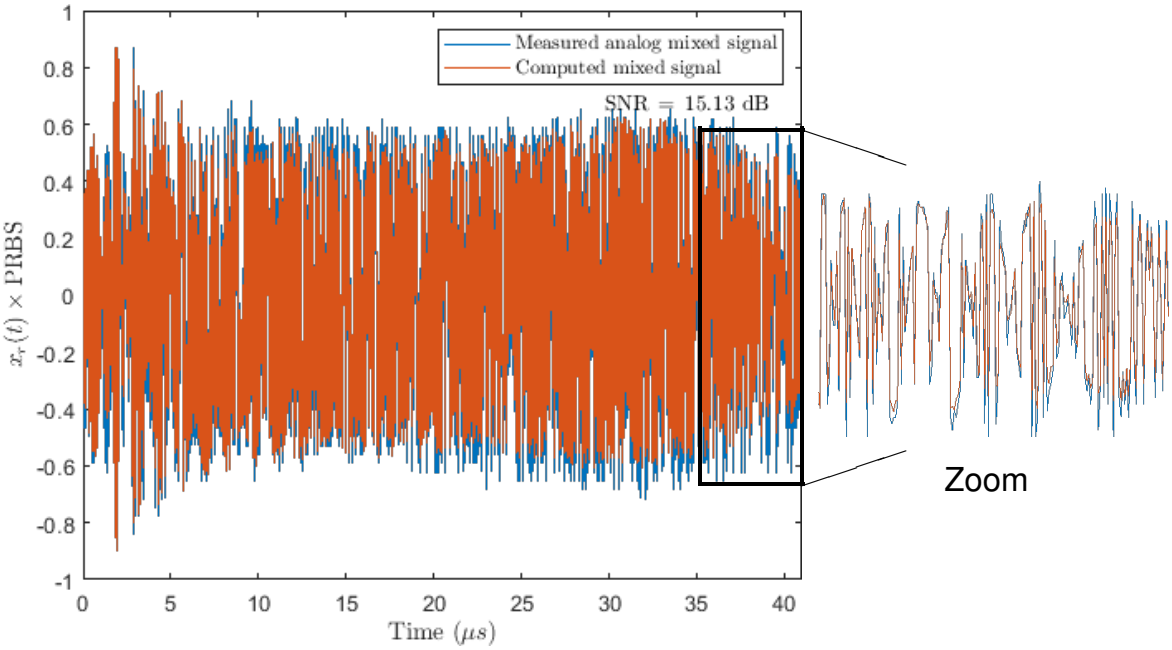

Figure 4.19: Reflected signal multiplied with the PRBS, with blue by ADL5391 and with red numerically in MATLAB.

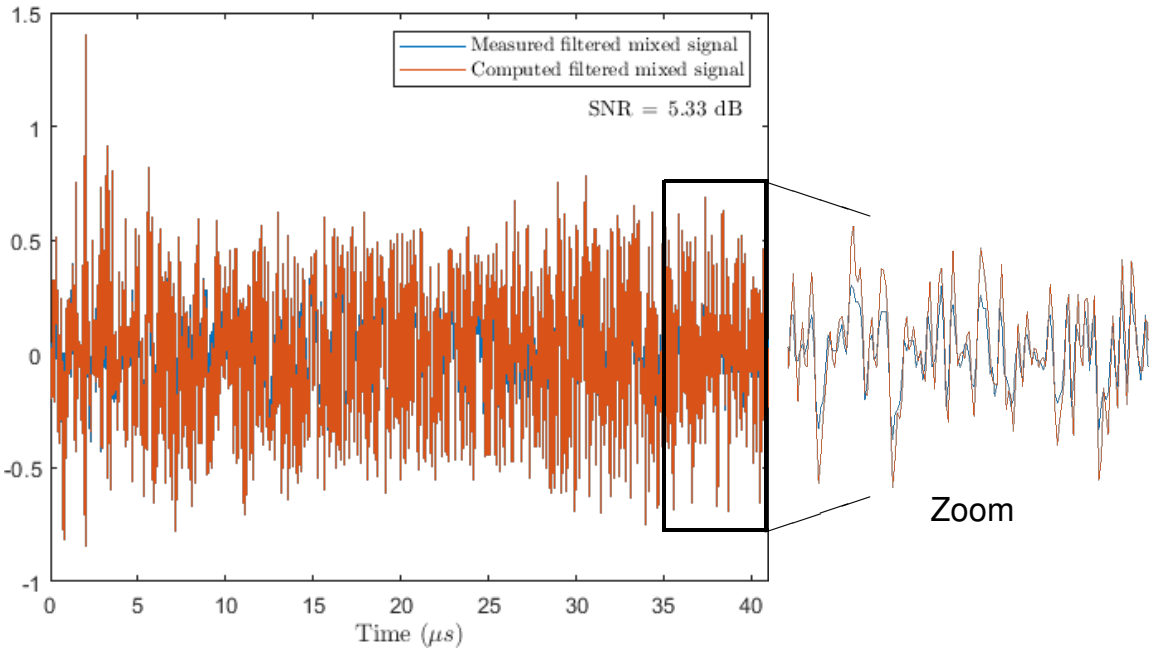

Figure 4.20: Filtered signal after multiplication at a $f_c = 12$ MHz, where the blue is filtered by ADRF6510 and the red is numerically filtered using the Butter function of MATLAB.

Second, the filtering is applied by the ADRF6510 filter with a cut of frequency $f_c = 12$ MHz. In this specific instance, the compression factor corresponds to 4, because theoretically $f_{\text{Nyq}} = 2f_{max} = 50$ MHz. In this case, as explained in section 4.2, an approximation using the Butterworth filter of MATLAB is applied. The current situation is more complex and will involve more noises. Moreover, it is important to obtain the exact impulse response of the analog filter. As a matter of fact, the f_c of the analog filter corresponds to -0.5 dB. Hence, for analog $f_c = 12$ dB the cut off frequency of MATLAB's Butterworth filter should be settle to 14.3010 MHz. Figure 4.20 illustrates the two analog measured and simulated modulated reflected signals with an SNR $= 5.33$ dB. Third, by sub-sampling the signal with a factor 4, we will end up with 512 samples.

Finally, based on the advantages of the OMP algorithm and with the choice of the performance characteristics, the reflected signal of size 2048 is reconstructed and illustrated in Figure 4.21. In order to obtain the reflectogram, the final step for wire diagnosis is to apply the correlation. As noticed in Figure 4.22, the possibility of detecting the defect by only measured signals is missed. However, using the computed approach, the reflection at 87 m (end of the wire) is detected.

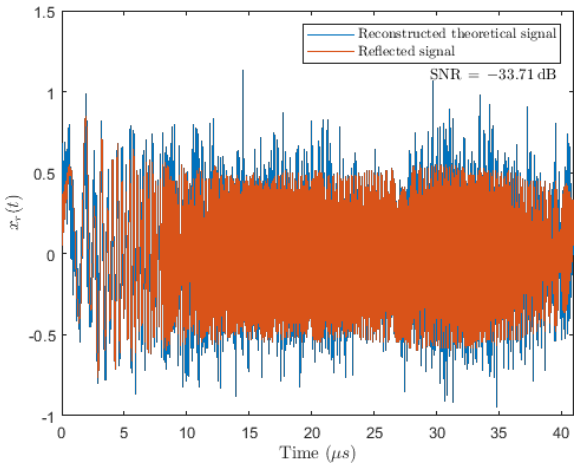

(a) Reconstructed computed reflected signal.

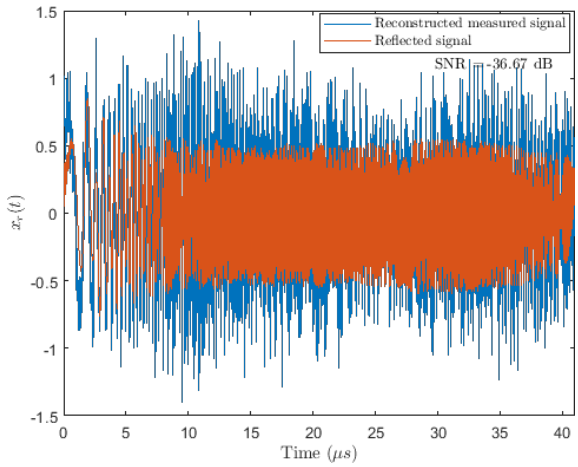

(b) Reconstructed measured reflected signal.

Figure 4.21: Reconstructed signal vs. standard reflected signal.

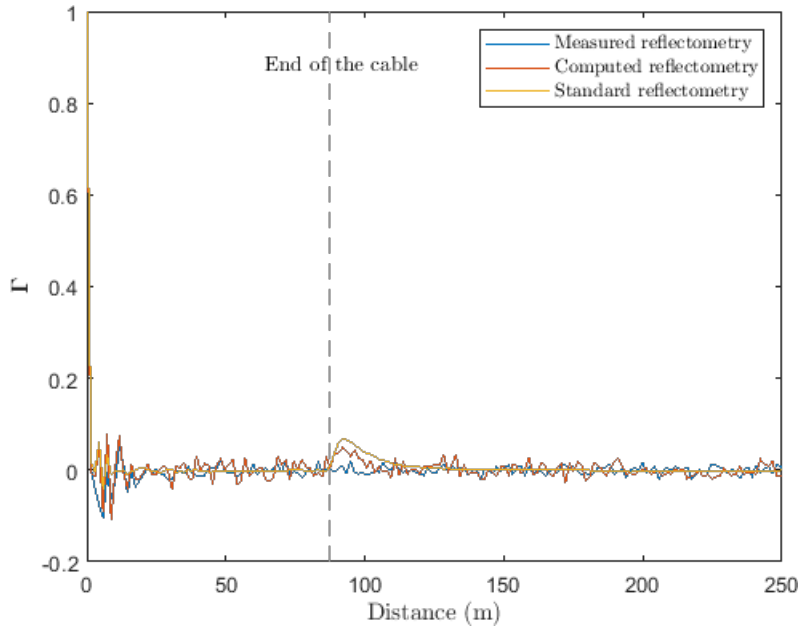

Figure 4.22: Reflectograms comparison approach between the measured, theoretical, and standard.

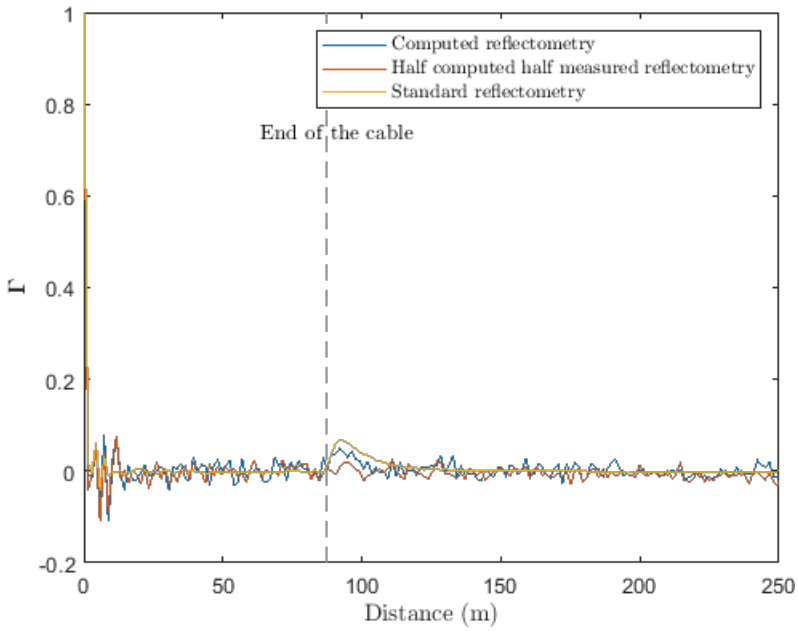

Figure 4.23: Reflectograms comparison approach between the half measured half theoretical, theoretical, and standard.

4.5.1 Impact of the filter

Accordingly, to find the source of the problem and to detect the defect, we apply a concept where half measured and half computed method are exploited. In this particular case, an analog multiplication and numerical low-pass filtering are examined. The proposed method allows nearly a proper detection with an SNR $= 6.9$ dB (Figure 4.23). Hence, we notice the importance of controlling the impulse response of the filter for the reconstruction algorithm to improve the result. Therefore, the choice of the Butterworth low-pass filter is replaced by an ideal integrator with cut off frequency $f_c = 12.5$ MHz. The impulse response and the frequency representation of this filter are represented in Figure 4.24. The reflectograms of Figure 4.25 shows an improvement of the localization of the defect; hence an improvement of the SNR of the reconstructed signals. Therefore, it results an SNR $= [20.54, 13.98,=]$ dB for theoretical operations and half analogical half numerical operations, respectively. Besides, a small attenuation of the signal can cause a loss on the peak, especially while testing wires with high attenuation electrical characteristics. However, the choice of the filter needs more maturity and more time to search the related reasons behind the non convergence of the reconstruction algorithms.

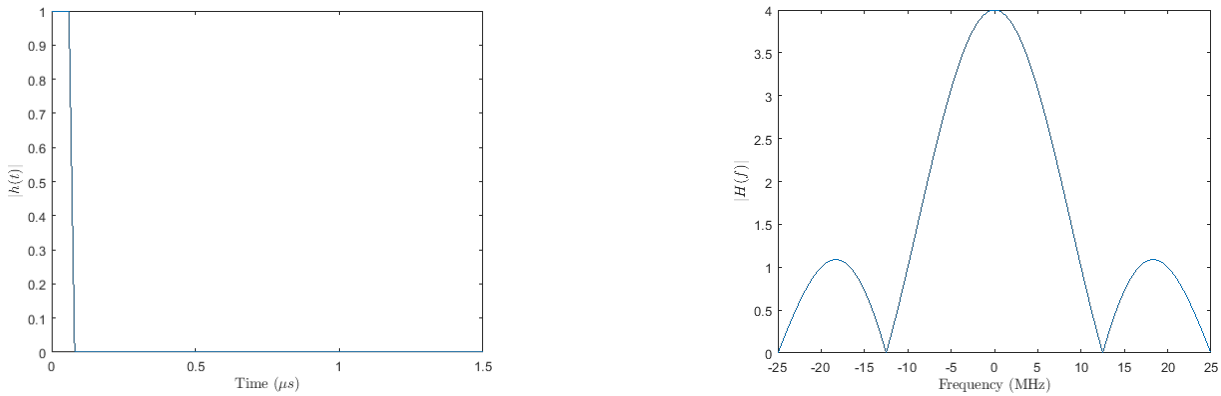

(a) Temporal domain.

(b) Frequency domain

Figure 4.24: The impulse response of perfect integrator in temporal and frequency domain with cut off frequency $f_c = 12.5$ MHz.

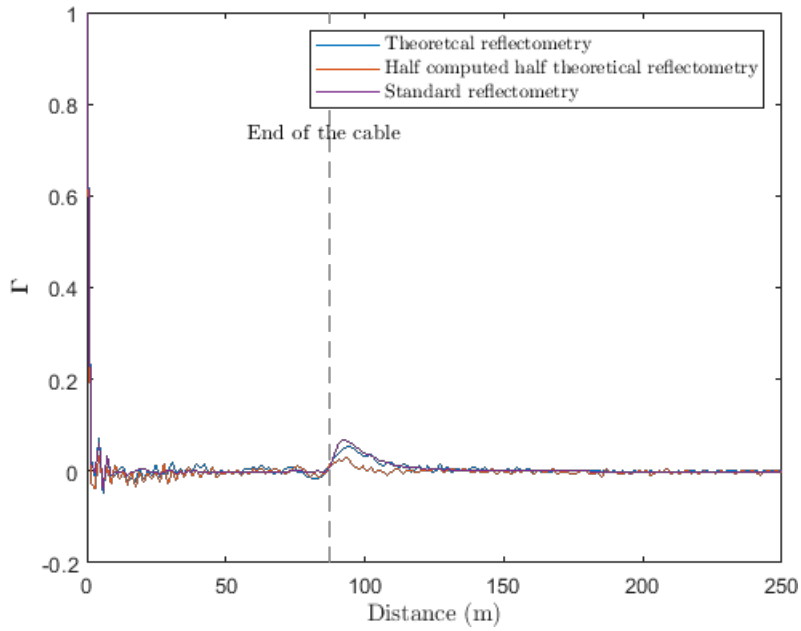

Figure 4.25: Reflectograms comparison approach between the half measured-half theoretical, theoretical, and standard.

4.6 Conclusion

We began this chapter by demonstrating the new architecture for wire diagnosis system based on reflectometry. This architecture will improve the localization of the defect in a wired network and was chosen as it presents interesting features for multi-carrier wideband reflectometry signals. In particular, we detail the experimental approach con-

ducted on a specifically designed AIC prototype. As followed, the original reflectometry architecture limitation is explained, especially the importance of the spatial resolution which refers to the ability to discriminate two close defects. In fact, improving the spatial resolution while preserving highly accurate fault positions in short acquisition and processing periods, necessitate outperforming ADCs and DACs. Accordingly, an increased complexity of hardware implementation and highly expensive elements are required.

The proposed architecture offers the possibility to overcome the limitation of ADC, in terms of limitation of sampling frequency value. To validate the feasibility between these two domains (Reflectometry and CS), we used the linear complex chirp and MCTDR signal models and proposed their dictionaries of sparse representation in FrFT and DCCT, respectively. In the simulation analysis, we suggest two types of networks: point-to-point and one junction Y-network. In a point-to-point network, the additive noise impact on the reflected signal is analyzed. The modified reflectometry results are evaluated by measuring the SNR or the SINAD of the reconstructed reflectogram for different values of the compression ratio. The main result, for both network and signal, is that this new acquisition scheme allows the detection of multiple reflection peaks caused by the defects at a sampling frequency 8 times lower than the classical Nyquist rate with a relative fault location error of 2%. In addition, in order to be more realistic, we proposed a study based on increasing the bandwidth of the injected signal and by keeping the same sampling frequency. Markedly, those results have proven to be efficient in enhancing the spatial resolution and returning accurate estimates of fault's locations.

General Conclusion and Perspectives

Conclusion

The study conducted in this thesis aims to propose, develop, and assess new hardware approach for the diagnosis of complex wired networks to meet the need and the problem of detecting and locating faults appeared on electrical wires. The reflectometry-based technique for detecting and locating faults in wiring networks and the critical importance of the hardware limitations of this technique has been explained. In fact, for online testing wire networks instead of using a Dirac-pulse, multi-carrier wide-band signals are used. Basically, it will permit controlling the channel bandwidth of the testing signal so that will not interfere with the native signals operating on the system. While dealing with such a system, the ability of accurately detecting the position of a fault along the NUT is a major challenge. This property is directly related to the sampling frequency of the components. The conventional paradigm in digital signal processing for reconstructing signals from measured data follows Shannon sampling theorem. This approach guarantees the preservation of the information that is in the signal being sampled, but the cost is reflected in the number of samples that are required to represent the signal. Unfortunately, nowadays, mainly, ADC constitute a limitation for the considered $(f_{sampling}, N_{bits})$ couple. Moreover, from a commercial point marketing aspect, they become very expensive as either the resolution or the sampling frequency increases.

Therefore, the literature study achieved during the three years of the thesis led us to find a new and effective data acquisition methods for practical instrumentation development, which can be used in case of monitoring purpose the wired network with an increasing the signal bandwidth. The state of the art performed in the first year permitted developing a conviction of the importance of Compressive Sampling (CS) methods in fulfilling our aim.

Within this context, using CS ideas need to overcome multiple challenges before

the actual CS-based reflectometry systems become a reality. Those challenges for reflectometry systems are chosen precisely and detailed in this thesis:

- The injected and the reflected signals must be compressible, i.e. sparse, in some basis or dictionaries. Since the MC signals of the reflectometry have a sparse representation in neither time nor frequency domain, thus time-frequency analysis is needed to obtain an intermediate domain where the signal is sparser than in time or in frequency. We validate two sparse domains: the FrFT for the complex chirp signal and the CS-DCCT for MCTDR signal. However, the sparsity is directly related to the electrical characteristics of the NUT. The major difference between these two transformations is that one of them is based on real chirps instead of using a transform that depends on complex chirps such as the FrFT.

- The signal recovery algorithms must be able to handle real-world acquisition scenarios with sufficient computational efficiency and robust performance for noisy data. In this approach, the OMP algorithm has been used. Several advantages exist such as it shows very useful results from the computational complexity point of view and handles multiple signals in the same base-band; hence, it is one of the optimal solutions for MC signals. Beside, its computational complexity is low,hence it is also fast and straightforward to implement.

- The choice of unique AIC-based adapted for reflectometry. This latter is a combination of hardware and software, offering a powerful method for the acquisition of a wide-band signal. Meanwhile, this hardware allows us to operate at a rate much lower than the one required by Shannon-Nyquist. However, there is a tradeoff between the reduced sampling rate and the resolution of the reconstructed signal resulted from CS. In the simulation results, several aspects were treated, such as a point-to-point network, a complex wire network, different electrical characteristics, and a noisy reflected signal.

Both chirp and MCTDR signals show relevant and usable results while using a sampling frequency 8 times lower than what would be needed by traditional Shannon-Nyquist sampling theory ($\text{SNR}_{\text{chirp}} = 7.83\,\text{dB}$ and $\text{SNR}_{\text{MCTDR}} = 6\,\text{dB}$). The new reflectometry hardware was evaluated, by measuring the SNR of the reflected signal as well as the SINAD of the reconstructed reflectogram for different values of the compression ratio. Equally important, it has the advantage of improving the performance

of diagnostic systems by increasing the transmission rate for the same bandwidth — accordingly, a significant improvement of super-resolution that estimates the locations of the defects.

As a conclusion, notably, the idea of CS for the new reflectometry systems could enable shifting the emphasis from expensive hardware of required ADC conversion to smart signal recovery algorithms. The four main objectives: reconstruction, detection, localization, and characterization, are performed using a digital algorithm and can even be performed off-line. Hence the improvement in the performance of the reflectometry architecture and the substantial gain in storage memory are achieved by the sub-sampling system.

Perspectives

In this thesis, we exploited on adapting CS properties to the problem of fault detection and location in transmission line networks. In point of fact, efficient and significant results have been obtained with single as well as multiple faults in different network structures. With this in mind, an extensive study could be conducted to continue or handle other features that we were not able to address in our work. Some of these perspectives are listed in the following:

- While using the CS, in this thesis, we exclusively focused on the reconstruction of the reflected signal. As a matter of fact, in reflectometry applications, we are purely interested in the localization of the defect rather than the reflected signal itself. Consequently, for the future work, without reconstructing the reflected signal, we plan to detect, classify, and localize the defect by applying a more statistical approach on the dictionaries. The main idea is to seek the possibility from a small set of random measurements which extracts the necessary information on the defect. In this case, from one point, a fewer sample can be required for defect detection instead of signal reconstruction, and from another, the computational complexity of detection can be reduced compared to reconstruction.

- It will be interesting to implement the CS and reflectometry architecture based on an FPGA for live testing. However, that idea itself has so many complicated and challengeable notions. One of this notion is the clocking jitter, especially for the binary sequence PRBS since the speed of the PRBS is much important than

the sampling frequency. Thus the noise introduced by jitter may affect the SNR performances of the systems. Also, it demands much precision, especially on the unavoidable nonidealities added by the different components of the AIC architecture, whereas it will destroy the analog waveform. Therefore, there is a need to deal with the robustness of the CS and its sensitivity to the presence of the noise.

BIBLIOGRAPHY

[1] Adrien Lelong, “Méthodes de diagnostic filaire embarqué pour des réseaux complexes (Embedded wire diagnosis methods for complex networks)”, PhD thesis, Université Lille1 - Sciences et Technologies, 2010.

[2] Wafa Ben Hassen, “Étude de stratégies de diagnostic embarqué des réseaux filaires complexes”, PhD thesis, Oct. 2014.

[3] Lola El El Sahmarany Sahmarany, “Improvement methods for cable diagnosis by reflectometry”, Theses, Université Blaise Pascal - Clermont-Ferrand II, Dec. 2013, URL: https://tel.archives-ouvertes.fr/tel-00999462.

[4] C. Furse and R. Haupt, “Down to the Wire [Aircraft Wiring]”, *in*: *IEEE Spectr.* 38.*2* (Feb. 2001), pp. 34–39, ISSN: 0018-9235.

[5] R. C. Taft et al., “A 1.8-V 1.6-GSample/s 8-b self-calibrating folding ADC with 7.26 ENOB at Nyquist frequency”, *in*: *IEEE Journal of Solid-State Circuits* 39.*12* (2004), pp. 2107–2115.

[6] David L Donoho, “Compressed sensing”, *in*: *IEEE Transactions on information theory* 52.*4* (2006), pp. 1289–1306.

[7] Emmanuel J Candès, Justin Romberg, and Terence Tao, “Robust uncertainty principles: Exact signal reconstruction from highly incomplete frequency information”, *in*: *IEEE Transactions on information theory* 52.*2* (2006), pp. 489–509.

[8] Joel A Tropp et al., “Beyond Nyquist: Efficient sampling of sparse bandlimited signals”, *in*: *IEEE Transactions on Information Theory* 56.*1* (2010), pp. 520–544.

[9] Frédéric Cohen Tenoudji, *Analog and digital signal analysis: from basics to applications*, Springer, 2016.

[10] Galen Mark Gaeris and Paul Z Vanderlaan, *High-performance data cable*, US Patent 5,789,711, Aug. 1998.

[11] Fabrice Auzanneau, “Wire troubleshooting and diagnosis: Review and perspectives”, *in*: *Progress In Electromagnetics Research* 49 (2013), pp. 253–279.

[12] J. Densley, “Ageing mechanisms and diagnostics for power cables - an overview”, *in*: *IEEE Electrical Insulation Magazine* 17.*1* (Jan. 2001), pp. 14–22, ISSN: 0883-7554.

[13] Technical Report Edition 2013, *Schéma décennal de développement du réseau de transport d’électricité*, Réseau de Transport d’Electricité (RTE), Février 2014.

[14] Steven R. Skinner and K. Khan, “Wiring Assessment of Commuter Class Aircraft”, *in*: Aging Aircraft conference, Feb. 2005.

[15] D. Lee and P. Arnason, “U.S. Navy Wiring Systems Lessons Learned.”, *in*: *In Joint Conference on Aging Aircraft*, 2000.

[16] Kevin R Wheeler et al., “Aging aircraft wiring fault detection survey”, *in*: (2007).

[17] F. Loete, Q. Zhang, and M. Sorine, “Experimental Validation of the Inverse Scattering Method for Distributed Characteristic Impedance Estimation”, *in*: *IEEE Transactions on Antennas and Propagation* 63.*6* (June 2015), pp. 2532–2538, ISSN: 0018-926X, DOI: 10.1109/TAP.2015.2417215.

[18] C. Smith, *Transport aircraft intrusive inspection project (an analysis of the wire installations of six decommissioned aircraft)*, Final Report, Aging Transport Systems Rulemaking Advisory Committee (ATSRAC), 2000.

[19] Santi Bhushana Reddy Basava, “Signal Processing Solutions to Detection and Location of Cable Faults in Aging Aircraft Wiring Using Reflectometry Methods”, PhD thesis, Utah State University, Department of Electrical and Computer Engineering, 2003.

[20] Australian Transport Safety Bureau, *How Old is Too Old? The impact of ageing aircraft on aviation safety*, Report, Austalian Government, 2007, p. 78.

[21] M Dornheim, “New rules and hardware for wiring soon to emerge”, *in*: *Aviation Week and Space Technology* 154.*14* (2001), p. 92.

[22] *Airworthiness Directives; Boeing Model 737-100, -200, -200C, -300, -400, and -500 Series Airplanes*, Federal Register, May 22, 2007, (visited on 01/07/2019).

[23] K. Blemel and C. Furse, “Applications of microsystems and signal processing for wiring integrity monitoring”, *in*: *2001 IEEE Aerospace Conference Proceedings (Cat. No.01TH8542)*, vol. 7, Mar. 2001, 7–3253 vol.7, DOI: 10.1109/AERO.2001.931401.

[24] H. M. Hashemian, “State-of-the-Art Predictive Maintenance Techniques”, *in*: *IEEE Transactions on Instrumentation and Measurement* 60.*1* (Jan. 2011), pp. 226–236, ISSN: 0018-9456, DOI: 10.1109/TIM.2010.2047662.

[25] Nassif Berrabah, “Problèmes inverses pour le diagnostic de câbles électriques à partir de mesures de réflectométrie”, PhD thesis, Nov. 2017.

[26] Robert E Collin, *Foundations for microwave engineering*, John Wiley & Sons, 2007.

[27] E. J. Lundquist et al., “Advanced Forward Methods for Complex Wire Fault Modeling”, *in*: *IEEE Sensors Journal* 13.*4* (Apr. 2013), pp. 1172–1179, ISSN: 1530-437X, DOI: 10.1109/JSEN.2012.2227996.

[28] Moussa Kafal, “Imaging Techniques for soft fault detection and location in wiring networks”, Theses, Université Paris-Saclay, Sept. 2016, URL: https://tel.archives-ouvertes.fr/tel-01396175.

[29] C. Furse et al., “Frequency-domain reflectometry for on-board testing of aging aircraft wiring”, *in*: *IEEE Transactions on Electromagnetic Compatibility* 45.*2* (May 2003), pp. 306–315, ISSN: 0018-9375, DOI: 10.1109/TEMC.2003.811305.

[30] Fengqing Bao, “Sparse Overcomplete Representation applied to FMCW Reflectometry for Non-uniform Transmission Lines”, PhD thesis, Technische Universität München, 2015.

[31] Cynthia Furse and Nilesh Kamdar, “An inexpensive distance measuring system for navigation of robotic vehicles”, *in*: *Microwave and Optical Technology Letters* 33.*2* (2002), pp. 84–87.

[32] A.J. Hymans and J Lait, “Analysis of a frequency-modulated continuous-wave ranging system”, *in*: *Proceedings of the IEE - Part B: Electronic and Communication Engineering* 107 (Aug. 1960), pp. 365 –372, DOI: 10.1049/pi-b-2.1960.0130.

[33] Cynthia Furse and Raymond Woodward, *Cable testing, cable length, and liquid level determination system utilizing a standing wave reflectometer*, US Patent App. 10/308,864, Dec. 2003.

[34] Nicolas Ravot, “ANALYSE ET DIAGNOSTIC DE RESEAUX FILAIRES COMPLEXES PAR REFLECTOMETRIE”, Theses, Université Paris-Sud, 2007.

[35] You Chung Chung, Cynthia Furse, and Jeremy Pruitt, “Application of phase detection frequency domain reflectometry for locating faults in an F-18 flight control harness”, English, *in*: *IEEE Transactions on Electromagnetic Compatibility* 47.*2* (May 2005), pp. 327–334, ISSN: 0018-9375, DOI: 10.1109/TEMC.2005.847403.

[36] Cynthia Furse et al., “A critical comparison of reflectometry methods for location of wiring faults”, English, *in*: *Smart Structures and Systems* 2.*1* (Jan. 2006), pp. 25–46, ISSN: 1738-1584.

[37] L. A. Griffiths et al., “The invisible fray: a critical analysis of the use of reflectometry for fray location”, *in*: *IEEE Sensors Journal* 6.*3* (June 2006), pp. 697–706, ISSN: 1530-437X, DOI: 10.1109/JSEN.2006.874017.

[38] A. Cozza and L. Pichon, “Echo Response of Faults in Transmission Lines: Models and Limitations to Fault Detection”, *in*: *IEEE Transactions on Microwave Theory and Techniques* 64.*12* (Dec. 2016), pp. 4155–4164, ISSN: 0018-9480, DOI: 10.1109/TMTT.2016.2608774.

[39] C. Furse et al., “Feasibility of spread spectrum sensors for location of arcs on live wires”, *in*: *IEEE Sensors Journal* 5.*6* (Dec. 2005), pp. 1445–1450, ISSN: 1530-437X, DOI: 10.1109/JSEN.2005.858900.

[40] Cynthia Furse et al., “Spread spectrum sensors for critical fault location on live wire networks”, *in*: *Structural Control and Health Monitoring* 12.*3-4* (2005), pp. 257–267, DOI: 10.1002/stc.69, URL: https://onlinelibrary.wiley.com/doi/abs/10.1002/stc.69.

[41] Xudong SHI et al., “Fault Detection of Aircraft Cable via Spread Spectrum Time Domain Reflectometry”, *in*: *Sensors & Transducers* 167 (Mar. 2014), pp. 135–141.

[42] Chet Lo and Cynthia Furse, “Noise-domain reflectometry for locating wiring faults”, English, *in*: *IEEE Transactions on Electromagnetic Compatibility* 47.*1* (Feb. 2005), pp. 97–104, ISSN: 0018-9375, DOI: 10.1109/TEMC.2004.842109.

[43] S. Naik, C. M. Furse, and B. Farhang-Boroujeny, “Multicarrier reflectometry”, *in*: *IEEE Sensors Journal* 6.*3* (June 2006), pp. 812–818, ISSN: 1530-437X, DOI: 10.1109/JSEN.2006.874018.

[44] A. Lelong and M. O. Carrion, “On line wire diagnosis using Multicarrier Time Domain Reflectometry for fault location”, *in*: *SENSORS, 2009 IEEE*, Oct. 2009, pp. 751–754.

[45] Bonhomme Yannick Guilhemsang Julien Auzanneau Fabrice, “Method for improving fault detection and positioning precision using reflectometry in a wired electrical network”, pat. 8620605, Dec. 2013.

[46] E. Cabanillas, C. Layer, and M. Kafal, “On the phase analysis of multi-carrier signals for high-precision fault detection by reflectometry”, *in*: *2017 IEEE SENSORS*, Aug. 2017, pp. 1–3, DOI: 10.1109/ICSENS.2017.8234182.

[47] E. Cabanillas et al., “Enhancing the Spatial Resolution for Wire Fault Detection Systems using Multi-Carrier Signals”, *in*: *IEEE Sensors Journal* (2018), pp. 1–1, ISSN: 1530-437X, DOI: 10.1109/JSEN.2018.2872409.

[48] R. H. Walden, “Analog-to-digital converter survey and analysis”, *in*: *IEEE Journal on Selected Areas in Communications* 17.*4* (Apr. 1999), pp. 539–550, ISSN: 0733-8716, DOI: 10.1109/49.761034.

[49] Boris Murmann, “Trends in Low-Power, Digitally Assisted A/D Conversion”, *in*: *IEICE Transactions* 93-C (2010), pp. 718–729.

[50] Laura Anitori, “Compressive Sensing and Fast Simulations: Applications to Radar Detection”, PhD thesis, TU Delft, Delft University of Technology, 2012.

[51] Hossein Mamaghanian, “Compressed sensing: a universal energy-efficient compression scheme for biosignals on wireless body sensor nodes”, *in*: (Jan. 2014).

[52] Andrianiaina Ravelomanantsoa, “Approche déterministe de l’acquisition comprimée et la reconstruction des signaux issus de capteurs intelligents distribués”, PhD thesis, Nov. 2015.

[53] Nicolas Chauffert, Philippe Ciuciu, and Pierre Weiss, “Variable density compressed sensing in MRI. Theoretical vs heuristic sampling strategies”, *in*: *Biomedical Imaging (ISBI), 2013 IEEE 10th International Symposium on*, IEEE, 2013, pp. 298–301.

[54] Saad Qaisar et al., “Compressive sensing: From theory to applications, a survey”, *in*: *Journal of Communications and networks* 15.*5* (2013), pp. 443–456.

[55] P. Nagesh and Baoxin Li, “Compressive imaging of color images”, *in*: *2009 IEEE International Conference on Acoustics, Speech and Signal Processing*, Apr. 2009, pp. 1261–1264, DOI: 10.1109/ICASSP.2009.4959820.

[56] *A new compressive imaging camera architecture using optical-domain compression*, vol. 6065, 2006, pp. 6065 –6065 –10, DOI: 10.1117/12.659602, URL: https://doi.org/10.1117/12.659602.

[57] Michael Lustig, David Donoho, and John M Pauly, “Sparse MRI: The application of compressed sensing for rapid MR imaging”, *in*: *Magnetic Resonance in Medicine: An Official Journal of the International Society for Magnetic Resonance in Medicine* 58.*6* (2007), pp. 1182–1195.

[58] F. J. Herrmann and G. Hennenfent, “Non-parametric seismic data recovery with curvelet frames”, *in*: *Geophysical Journal International* 173.*1* (Apr. 2008), pp. 233–248, ISSN: 0956-540X, DOI: 10.1111/j.1365-246X.2007.03698.x.

[59] M. A. Herman and T. Strohmer, “High-Resolution Radar via Compressed Sensing”, *in*: *IEEE Transactions on Signal Processing* 57.*6* (June 2009), pp. 2275–2284, ISSN: 1053-587X.

[60] David L Donoho and Emmanuel J Candes, *Digital ridgelet transform via digital polar coordinate transform*, US Patent 6,766,062, July 2004.

[61] J. Romberg, “Imaging via Compressive Sampling”, *in*: *IEEE Signal Processing Magazine* 25.*2* (Mar. 2008), pp. 14–20, ISSN: 1053-5888, DOI: 10.1109/MSP.2007.914729.

[62] Stephane Mallat, *“A wavelet tour of signal processing: the sparse way”*, Academic press, 2008.

[63] R. Baraniuk and P. Steeghs, “Compressive Radar Imaging”, *in*: *2007 IEEE Radar Conference*, Apr. 2007, pp. 128–133, DOI: 10.1109/RADAR.2007.374203.

[64] E. J. Candes and M. B. Wakin, “An Introduction To Compressive Sampling”, *in*: *IEEE Signal Processing Magazine* 25.*2* (Apr. 2008), pp. 21–30, ISSN: 1053-5888, DOI: 10.1109/MSP.2007.914731.

[65] Emmanuel J Candes, “The restricted isometry property and its implications for compressed sensing”, *in*: *Comptes rendus mathematique* 346.*9-10* (2008), pp. 589–592.

[66] T. T. Cai, G. Xu, and J. Zhang, "On Recovery of Sparse Signals Viaℓ_1Minimization", *in*: *IEEE Transactions on Information Theory* 55.*7* (July 2009), pp. 3388–3397, ISSN: 0018-9448, DOI: 10.1109/TIT.2009.2021377.

[67] Emmanuel J Candes and Terence Tao, "Near-optimal signal recovery from random projections: Universal encoding strategies?", *in*: *IEEE transactions on information theory* 52.*12* (2006), pp. 5406–5425.

[68] Yonina C Eldar and Gitta Kutyniok, *Compressed sensing: theory and applications*, Cambridge University Press, 2012.

[69] Simon Foucart and Holger Rauhut, *A mathematical introduction to compressive sensing*, vol. 1, 3, Birkhäuser Basel, 2013.

[70] Joel A Tropp and Anna C Gilbert, "Signal recovery from random measurements via orthogonal matching pursuit", *in*: *IEEE Transactions on information theory* 53.*12* (2007), pp. 4655–4666.

[71] Emmanuel Candes and Justin Romberg, "Sparsity and incoherence in compressive sampling", *in*: *Inverse problems* 23.*3* (2007), p. 969.

[72] Yaniv Zigel, Arnon Cohen, and Amos Katz, "The weighted diagnostic distortion (WDD) measure for ECG signal compression", *in*: *IEEE Transactions on Biomedical Engineering* 47.*11* (2000), pp. 1422–1430.

[73] M. Wakin et al., "A Nonuniform Sampler for Wideband Spectrally-Sparse Environments", *in*: *IEEE Journal on Emerging and Selected Topics in Circuits and Systems* 2.*3* (Sept. 2012), pp. 516–529, ISSN: 2156-3357, DOI: 10.1109/JETCAS.2012.2214635.

[74] Jason N Laska et al., "Theory and implementation of an analog-to-information converter using random demodulation", *in*: *Circuits and Systems, 2007. ISCAS 2007. IEEE International Symposium on*, IEEE, 2007, pp. 1959–1962.

[75] Stephen R. Becker, *Practical Compressed Sensing: modern data acquisition and signal processing*, 2011.

[76] Pawel Jerzy Pankiewicz, Thomas Arildsen, and Torben Larsen, "Model-based calibration of filter imperfections in the random demodulator for compressive sensing", *in*: *arXiv preprint arXiv:1303.6135* (2013).

[77] Moshe Mishali et al., "Xampling: Analog to digital at sub-Nyquist rates", *in*: *IET circuits, devices & systems* 5.*1* (2011), pp. 8–20.

[78] S. Kirolos et al. J. Laska, “Random Sampling for Analog-to-Information Conversion of Wideband Signals”, *in*: *2006 IEEE Dallas/CAS Workshop on Design, Applications, Integration and Software*, Oct. 2006, pp. 119–122, DOI: 10.1109/DCAS.2006.321048.

[79] J. A. Tropp et al., “Random Filters for Compressive Sampling and Reconstruction”, *in*: *2006 IEEE International Conference on Acoustics Speech and Signal Processing Proceedings*, vol. 3, May 2006, pp. III–III, DOI: 10.1109/ICASSP.2006.1660793.

[80] Gil M Raz, *Method and system for nonlinear and affine signal processing*, US Patent 7,173,555, Feb. 2007.

[81] John P Slavinsky et al., “The compressive multiplexer for multi-channel compressive sensing”, *in*: *Acoustics, Speech and Signal Processing (ICASSP), 2011 IEEE International Conference on*, IEEE, 2011, pp. 3980–3983.

[82] R. Maleh et al., “Analog-to-Information and the Nyquist Folding Receiver”, *in*: *IEEE Journal on Emerging and Selected Topics in Circuits and Systems* 2.*3* (Sept. 2012), pp. 564–578, ISSN: 2156-3357, DOI: 10.1109/JETCAS.2012.2223611.

[83] S. Kirolos et al., “Analog-to-Information Conversion via Random Demodulation”, *in*: *2006 IEEE Dallas/CAS Workshop on Design, Applications, Integration and Software*, Oct. 2006, pp. 71–74, DOI: 10.1109/DCAS.2006.321036.

[84] S. K. Sharma et al., “Application of Compressive Sensing in Cognitive Radio Communications: A Survey”, *in*: *IEEE Communications Surveys Tutorials* 18.*3* (2016), pp. 1838–1860, DOI: 10.1109/COMST.2016.2524443.

[85] Mohammed Abo-Zahhad et al., “Wideband Cognitive Radio Networks Based Compressed Spectrum Sensing: A Survey”, *in*: *Journal of Signal and Information Processing* 9.*02* (2018), p. 122.

[86] Haldun M Ozaktas and M Alper Kutay, “The fractional Fourier transform”, *in*: *2001 European Control Conference (ECC)*, IEEE, 2001, pp. 1477–1483.

[87] V Ashok Narayanan and KMM Prabhu, “The fractional Fourier transform: theory, implementation and error analysis”, *in*: *Microprocessors and Microsystems* 27.*10* (2003), pp. 511–521.

[88] Jianmin Mei et al., “A multi-order FRFT self-adaptive filter based on segmental frequency fitting and early fault diagnosis in gears”, *in*: *Measurement* 91 (2016), pp. 532–540.

[89] Osama Alkishriwo, “The Discrete Linear Chirp Transform and its Applications”, June 2013, URL: http://d-scholarship.pitt.edu/17769/.

[90] Arnab Shaw and Luay Alirkhis, “Wideband directions of arrival estimation of chirp sources using compressive sensing”, *in*: May 2018, p. 57, DOI: 10.1117/12.2316654.

[91] *DC to 2.0 GHz Multiplier, Data Sheet - ADL5391*, Analog Device, URL: https://www.analog.com/media/en/technical-documentation/data-sheets/ADL5391.pdf.

[92] *30 MHz Dual Programmable Filters and Variable Gain Amplifiers, Data Sheet - ADRF6510*, Analog Device, URL: https://www.analog.com/media/en/technical-documentation/data-sheets/ADRF6510.pdf.

[93] “IEEE Standard for Terminology and Test Methods for Analog-to-Digital Converters”, *in*: *IEEE Std 1241-2010 (Revision of IEEE std 1241-2000)* (Jan. 2011), pp. 1–139, DOI: 10.1109/IEEESTD.2011.5692956.

[94] Amey Kulkarni and Tinoosh Mohsenin, “Accelerating compressive sensing reconstruction OMP algorithm with CPU, GPU, FPGA and domain specific many-core”, *in*: May 2015, DOI: 10.1109/ISCAS.2015.7168797.

UNIVERSITE BRETAGNE LOIRE / MATHSTIC

CENTRALE NANTES

Titre: Exploration de l'Acquisition Comprimée appliquée à la Réflectométrie

Mot clés : diagnostic filaire, acquisition comprimée, matrices parcimonieuses

Résumé : La réflectométrie, une technique utilisée en diagnostic filaire, permet la détection et la localisation de défauts des câbles. Alors que, les Convertisseurs Analogique-Numérique sont indispensables dans les architectures de la réflectométrie, la nécessité du respect de la condition de Shannon et le besoin d'effectuer des traitements en temps réel limitent les fréquences maximales des signaux injectés, ainsi la précision de localisation. Pour une première fois dans le système de diagnostic filaire, cette étude s'inscrit l'échantillonnage comprimé du signal réfléchi afin d'améliorer ces performances. Pour cela en utilisant les signaux multi-porteuses de la réflectométrie, nous proposons les dictionnaires adaptées induisant la parcimonie. Ainsi, grâce à l'acquisition comprimée et son encodeur analogique nous arrivons à reconstruire le réflectogramme avec une fréquence d'échantillonnage moins élevée et également d'id-entifier les défauts à proximité.

Title: Exploration of Compressive Sampling for Wire Diagnosis Systems Based on Reflectometry

Keywords : wire diagnosis, Compressive Sampling, sparse matrices

Abstract : Reflectometry, a wire diagnosis technique, allows to detect and localize electrical defects in networks efficiently. In order to achieve a very precise online diagnosis without altering the functioning of a network, reflectometry methods should use specific wideband Multi-Carrier signals, whose generation requires dedicated numerical tools. The underlying architecture of any reflectometry system for the injection of the signal requires appropriate Digital-to-Analog Converters. Yet, measuring the reflected signal should be performed using Analog-to-Digital Converters capable of reaching high sampling frequencies together with sufficient resolution. Such converter are either extremely expensive or beyond nowadays state of the art. In that respect, this study addresses a new architectural approach for designing such reflectometry systems based on Compressive Sampling method bypassing the Nyquist rate. Thus, thanks to the compressed acquisition and its analog encoder, we succeed in reconstructing the reflectogram with a lower sampling frequency and also in identifying nearby defects.